NIST Advanced Manufacturing Series 100-45r1

Performance Measurement of a Mobile Manipulator-on-a-Cart and Coordinate Registration Methods for Manufacturing Applications

Omar Aboul-Enein
Roger Bostelman
Ya-Shian Li-Baboud
Mili Shah

This publication is available free of charge from:
https://doi.org/10.6028/NIST.AMS.100-45r1

National Institute of
Standards and Technology
U.S. Department of Commerce

NIST Advanced Manufacturing Series 100-45r1

Performance Measurement of a Mobile Manipulator-on-a-Cart and Coordinate Registration Methods for Manufacturing Applications

Omar Aboul-Enein
Intelligent Systems Division
Engineering Laboratory

Roger Bostelman
Smart HLPR, LLC
Frederick, MD

Ya-Shian Li-Baboud
Software and Systems Division
Information Technology Laboratory

Mili Shah
Department of Mathematics
The Cooper Union for the Advancement of Science and Art
New York, NY

This publication is available free of charge from:
https://doi.org/10.6028/NIST.AMS.100-45r1

April 2022

U.S. Department of Commerce
Gina M. Raimondo, Secretary

National Institute of Standards and Technology
James K. Olthoff, Performing the Non-Exclusive Functions and Duties of the Under Secretary of Commerce for Standards and Technology & Director, National Institute of Standards and Technology

National Institute of Standards and Technology
Advanced Manufacturing Series 100-45r1
Natl. Inst. Stand. Technol. Adv. Man. Ser. 100-45r1, 100 pages (April 2022)

This publication is available free of charge from:
https://doi.org/10.6028/NIST.AMS.100-45r1

Abstract

Mobile manipulators, which consist of a robotic manipulator arm on a vehicular base, enable more flexible and dynamic workflows in manufacturing processes by freeing the manipulator arm from the restriction of working on a single, calibrated workspace. A mobile manipulator-on-cart further enhances job concurrency since the manipulator arm is mounted to a detachable cart rather than directly to the vehicle payload structure. With this increase in flexibility, there is a need to understand new sources of position and orientation uncertainty. This uncertainty can degrade the accuracy and precision of the mobile manipulator position and orientation in addition to the coordination capability between the manipulator and vehicle. To facilitate performance evaluation and uncertainty characterization, the National Institute of Standards and Technology (NIST) has developed an artifact-based measurement methodology for mobile manipulator-on-a-cart systems. The artifact, which is re-configurable, simulates mock-assembly tasks for manufacturing applications, and is compared to a ground truth consisting of an optical tracking system (OTS). This report documents experimental procedures, data analysis methods, and results in measuring the performance of the manipulator-on-a-cart system. The speed and accuracy of two example coordinate registration techniques to be used by the mobile manipulator-on-a-cart to reduce position and orientation uncertainty are also compared.

Key words

Coordinate registration; experiment design; ground truth; mobile manipulators; mobile robot; optical tracking system; Re-configurable Mobile Manipulator Artifact (RMMA); robotics in manufacturing; statistical analysis; systems integration.

Table of Contents

List of Tables

List of Figures

Acronyms

2D two-dimensional. iv, vi, x, xi, 2, 12–14, 31, 34, 40, 42, 44, 45

3D three-dimensional. 2, 7, 9

AGV automatic guided vehicle. 1, 2, 5, 7, 17

AM additive manufacturing. 1

AMR autonomous mobile robot. 2, 3, 5, 8, 17, 18

ANOVA analysis of variance. xiii, xiv, 3, 46–50, 52, 57, 58, 71, 72

ap Assembly Point. iii–vi, x, xi, xiii, 9, 16–20, 22, 24, 25, 31–33, 38–46, 48, 49, 51–54, 56, 57, 59, 61, 62, 70, 71

AR augmented reality. 2

ARC average rate of change. x, 22

CNC computer numerical control. 1

CRPI Collaborative Robot Programming Interface. 7, 14–17, 72

CSV Comma Separated Value. 10, 22, 23

DoF Degrees of Freedom. x, xii, 5, 32–34

EOAT end-of-arm tool. iii–vi, ix–xi, 7, 10, 13–18, 20–25, 29, 31–33, 35, 38–45, 70

FPS frames-per-second. 10, 22

GPS global positioning system. 18

I/O input / output. vi, 7, 14, 81

lr Large Reflector. iv, x, xi, 9, 16–18, 20, 22, 23, 31, 32, 38, 40, 44

MP Megapixel. 9

MS mean square. xiii, xiv, 53

NIST National Institute of Standards and Technology. i, 1, 7, 72, 73

NTP Network Time Protocol. 6, 18, 19

OTS optical tracking system. i, iii–vi, x–xii, 2, 3, 9–13, 18–22, 24, 25, 31–43, 45, 69, 70, 72

POE power over Ethernet. 18

PTP Precision Time Protocol. 19, 72

RCS Real-time Control System. 7

RLS retro-reflective laser sensor and emitter. iv, 7, 8, 14–17, 24, 38, 70

RMMA Re-configurable Mobile Manipulator Artifact. i, iii–vi, ix–xv, 2, 3, 5–16, 20–24, 27, 30–32, 34–36, 38–47, 49, 51–53, 55, 57, 63, 68, 70–72, 81, 82

SNTP Synchronous Network Time Protocol. 19, 72

SS sum of squares. xiii, 47

SVD Singular Value Decomposition. 34

TCP/IP Transmission Control Protocol / Internet Protocol. 5–7

ULAPI User-Level Application Programming Interface. 7

USB Universal Serial Bus. 78

USNO United States Naval Observatory. 18

UTC Coordinated Universal Time. 18

XML Extensible Markup Language. 7

.

Nomenclature

Variables are subdivided into three categories: index variables, robotics variables, and statistics variables, with each using separate conventions. Index variables are denoted by lowercase Latin letters, however, for some index variables, a dot (".") in place of the given variable indicates that a value should be summed over all values of the index. For example if the variable, y_{abc}, is indexed by variables a, b, and c, then $y_{.bc}$ means that, for each value or b and c, the values of y should be summed over all values a. For robotics variables, scalars are denoted by lowercase Latin or Greek letters with no arrow (e.g., i and x). Furthermore, vectors are denoted by lowercase Latin letters with with an arrow (e.g., $\vec{f}_1$), and matrices are denoted by capital Latin letters, with H specifically used to

denote a homogeneous transformation matrix. For matrices and vectors, the applicable coordinate system(s), if any, are denoted as either a superscript or subscript in curly braces (e.g., ${}^{\{OTS.cart\}}\vec{c}_i$ and ${}^{\{OTS\}}\boldsymbol{H}_{\{MAP\}}$). Otherwise, an arbitrary, Cartesian coordinate system is assumed. Boldface is used to denote the unknown vectors or matrices in calibration problems (e.g., $\boldsymbol{t}_i$ and $\boldsymbol{R}_i$). Finally, statistics variables use common statistics conventions, except that all non-subscripted Latin letters used are presented in calligraphic font (e.g., y_{abc} and $\mathcal{H}_0$) to distinguish statistics variables from robotics variables

Index Variables

a An index variable indicating the level of the factor "measured RMMA side". The value 1 indicates the response was observed on the "RMMASq2" side of the RMMA, and the value 2 indicates the response was observed on the opposite side of the RMMA ("RMMASq3"). A dot (".") over this subscript indicates a variable is summed over all values of this index.

b An index variable indicating the level of the factor "coordinate registration method". The value 1 indicates the edge coordinate registration method was used, and the value 2 indicates that the bisect coordinate registration method was used (also see Eq. 7). A dot (".") over this subscript indicates a variable is summed over all values of this index.

c An index variable indicating the replicate number for factor level combination a and b (also see Eq. 7). Note that the valid range for c varies with a and b because the experiment was unbalanced (see also definition for n_{ab}). A dot (".") over this subscript indicates a variable is summed over all values of this index.

i Integer subscript denoting one of trials 1-11.

j Integer subscript denoting one of 9 registrations points detected per trial by the EOAT. See definition of $\vec{r}_j$.

Robotics Variables

$\vec{\boldsymbol{t}}_i$ A calibrated, unknown 2 x 1 translation vector for transforming between the $\vec{l}_{i,\vec{r}_j}$ points in the manipulator base coordinate system to the OTS coordinate system for the ith trial.

$\boldsymbol{R}_i$ A calibrated, unknown 2 x 2 rotation matrix for transforming between the $\vec{l}_{i,\vec{r}_j}$ points in the manipulator base coordinate system to the OTS coordinate system for the ith trial.

${}^{\{cartproj\}}\boldsymbol{H}_{\{transv\}}$ A calibrated, unknown 3 x 3 homogeneous transformation to transform between the projected cart rigid body centroid (see definition of ${}^{\{OTS\}}H_{i\{cartproj\}}$) and the cart transporter vehicle base.

${}^{\{OTS\}}\boldsymbol{H}_{\{MAP\}}$ A calibrated, unknown 3 x 3 homogeneous transformation to transform between the cart transporter vehicle map coordinate system to the OTS coordinate system.

θ The heading, or yaw, rotation of either the cart transporter vehicle within its map coordinate system or the cart rigid body in the OTS coordinate system.

θ_x Rotation angle about the x axis of a given coordinate system.

θ_y Rotation angle about the y axis of a given coordinate system.

θ_z Rotation angle about the z axis of a given coordinate system.

$\theta_{\vec{n}}$ Rotation angle about an arbitrary axis, $\vec{n}$, of a given coordinate system.

$\vec{ap}_{1-4}.b$ Used in some figures and tables to denote the 2D position for ap points localized by the EOAT after the bisect registration was performed, specifically. If this variable is used in a figure or table, then $\vec{ap}_{1-4}$ denotes the points localized by the EOAT after the edge registration was performed.

$\vec{ap}_{1-4}$ 2D position vector for one of four 3 mm diameter retro-reflective targets placed on the RMMA. These targets are localized by the EOAT of the manipulator using a fine spiral search to verify coordinate registration and manipulator position accuracy. Variables $\vec{ap}_{initial}$ and $\vec{ap}_{final}$ are also defined as example 2D localization points in Fig. 12 to describe the spiral search method.

$\vec{lr}_{1-4}$ 2D position vector for one of four 42 mm diameter retro-reflective targets placed on the RMMA for use with the bisect coordinate registration method. $lr_{initial}$, $lr_{adjusted}$, and lr_{final} are also defined as example 2D localization / registration points in Fig. 11 to describe the coarse spiral search and bisect registration method.

$\vec{corner}$ A 2D position vector, with components along either the x and y axes of the manipulator base coordinate system or the x and z axes of the OTS coordinate system, specifying the location of the RMMA table corner. Finding this point and the rotation offset between the cart base and RMMA is the main objective of the edge coordinate registration method.

$\vec{f}_1$ The first of two successive 3DoF position vectors of the EOAT rigid body centroid measured in the OTS coordinate system and occurring at time s_1. This variable was used in computing the ARC of the EOAT for OTS data selection. The position components of this vector along the x, y, and z axes of the OTS coordinate system are denoted $\vec{f}_1.x$, $\vec{f}_1.y$, and $\vec{f}_1.z$, respectively.

$\vec{f}_2$ The second of two successive 3DoF position vectors of the EOAT rigid body centroid measured in the OTS coordinate system and occurring at time s_2. This variable was used in computing the ARC of the EOAT for OTS data selection. The position

components of this vector along the x, y, and z axes of the OTS coordinate system are denoted $\vec{f}_2.x$, $\vec{f}_2.y$, and $\vec{f}_2.z$, respectively.

$\vec{i}$ The first of three imaginary components of a quaternion rotation (see Eq. 16 - 18 in Appendix D).

$\vec{j}$ The second of three imaginary components of a quaternion rotation in a given coordinate system (see Eq. 16 - 18 in Appendix D).

$\vec{k}$ The third of three imaginary components of a quaternion rotation in a given coordinate system (see Eq. 16 - 18 in Appendix D).

$\vec{l}_{i,\vec{r}_j}$ A vector storing the 2D (i.e., with position components along the x and y axes) position of the EOAT midpoint, when paused over the jth registration point and as logged by the manipulator controller (i.e., in the manipulator base coordinate system) for the ith trial.

$\vec{n}$ See definition of $\theta_{\vec{n}}$.

$\vec{o}_{i,\vec{r}_j}$ A vector storing the 2D (i.e., with position components along the x and z axes) position of the EOAT midpoint, when paused over the jth registration point and measured in the OTS coordinate system for the ith trial.

$\vec{r}_1$ The first of three 2D reference points on the edge of the RMMA detected by the manipulator EOAT for the edge coordinate registration method. The reference points are used to localize a corner point on the RMMA. This point is colinear with $\vec{r}_2$ so that a rotation offset between the manipulator and RMMA can be determined.

$\vec{r}_2$ The second of three 2D reference points on the edge of the RMMA detected by the manipulator EOAT for the edge coordinate registration method. This point is colinear with $\vec{r}_1$ so that a rotation offset between the manipulator and RMMA can be determined.

$\vec{r}_3$ The third of three 2D reference points on the edge of the RMMA detected by the manipulator EOAT for the edge coordinate registration method.

$\vec{r}_j$ One of 9 registration points that was detected by the EOAT per trial. Note that $\vec{r}_1$, $\vec{r}_2$ and $\vec{r}_3$ correspond to the same points defined as part of the edge coordinate registration method (see corresponding definitions). The point $\vec{r}_4$ corresponds to either $\vec{ap}_1$ or $\vec{ap}_3$ (see definition of $\vec{ap}_{1-4}$), depending on the side of the RMMA measured; $\vec{r}_5$ corresponds to $\vec{ap}_2$ or $\vec{ap}_4$ (see definition of $\vec{ap}_{1-4}$); $\vec{r}_6$ corresponds to to either $\vec{lr}_1$ or $\vec{lr}_3$ (see definition of $\vec{lr}_{1-4}$); $\vec{r}_7$ corresponds to to either $\vec{lr}_2$ or $\vec{lr}_4$, depending on the side of the RMMA measured; $\vec{r}_8$ corresponds to either $\vec{ap}_1.b$ or $\vec{ap}_3.b$ (see definition of $\vec{ap}_{1-4}.b$) as localized immediately following bisect registration; $\vec{r}_9$ corresponds to either $\vec{ap}_2.b$ or $\vec{ap}_4.b$ (see definition of $\vec{ap}_{1-4}.b$) as localized immediately following bisect registration.

b_1 An intercept term for one of two perpendicular lines that corresponds to the table edge of the RMMA and used as part of the intermediate computations implementing the edge coordinate registration method.

b_2 Another intercept term for one of two perpendicular lines that corresponds to the table edge of the RMMA and used as part of the intermediate computations implementing the edge coordinate registration method.

m The slope of the RMMA table edge computed from $\vec{r}_1$ and $\vec{r}_2$ as part of the edge coordinate registration method. Defined in Eq. 1.

q_w The value of the real component for a quaternion rotation in a given coordinate system (see Eq. 16 - 18 in Appendix D).

q_x Value of the $\vec{i}$ component for a quaternion rotation (see Eq. 16 - 18 in Appendix D).

q_y Value of the $\vec{j}$ component for a quaternion rotation (see Eq. 16 - 18 in Appendix D).

q_z Value of the $\vec{k}$ component for a quaternion rotation (see Eq. 16 - 18 in Appendix D).

$Rot(\theta_x, \theta_y, \theta_z)$ The XYZ Euler angle representation of a rotation.

$Rot(\vec{n}, \theta_{\vec{n}})$ The Axis-Angle representation of a rotation.

s_1 See definition of $\vec{f}_1$.

s_2 See definition of $\vec{f}_2$.

x Position component (in mm) along the x axis of a given coordinate system.

y Position component (in mm) along the y axis of a given coordinate system.

z Position component (in mm) along the z axis of a given coordinate system.

${}^{\{MAP.transv\}}\vec{v}_i$ A 3 x 1 vector containing the 3DoF pose of the cart transporter vehicle in the vehicle map coordinate system for the ith trial.

${}^{\{MAP\}}H_{i\{transv\}}$ A 3 x 3 homogeneous transformation matrix storing the 3DoF pose of the cart transporter vehicle measured in the vehicle map coordinate system for the ith trial. This variable stores the same information as ${}^{\{MAP.transv\}}\vec{v}_i$ (see corresponding definition), but in a different representation.

${}^{\{OTS.cart\}}\vec{c}_i$ A 6 x 1 vector containing the 6DoF pose of the cart rigid body centroid measured in the OTS coordinate system for the ith trial.

${}^{\{OTS\}}H_{i\{cartproj\}}$ A 3 x 3 homogeneous transformation matrix containing the 6DoF pose of the cart rigid body centroid measured in the OTS coordinate system and projected to a 3DoF pose for the ith trial.

Statistics Variables

$(\tau\beta)_{ab}$ The effect of the interaction between factors "measured RMMA side" and "coordinate registration method" on the response (see definition of y_{abc} and Eq. 7).

α The specified significance level for a given hypothesis test. Unless otherwise stated, all hypothesis tests in this report use a significance value of 0.05.

β_b The effect of the bth level of factor "coordinate registration method" on the response (see definition of y_{abc} and Eq. 7).

ε_{abc} The effect of random experimental error on the response (see definitions of y_{abc} and Eq. 7).

$\mathcal{MS}_{Error}$ The mean square (MS) attributed to Error. Generally, the mean square of an effect is the sum of squares of the effect divided by the degrees of freedom of the effect.

$\mathcal{SS}_{Coordn.Reg.Method}$ Contribution to $\mathcal{SS}_{Total}$ attributed to factor "coordinate registration method" for an ANOVA. Defined in Eq. 11.

$\mathcal{SS}_{Error}$ Contribution to $\mathcal{SS}_{Total}$ attributed to random experimental error for an ANOVA. Defined in Eq. 13.

$\mathcal{SS}_{Interaction}$ Contribution to $\mathcal{SS}_{Total}$ attributed to the interaction between factor "measured RMMA side" and factor "coordinate registration method" for an ANOVA. Defined in Eq. 12.

$\mathcal{SS}_{Side}$ Contribution to $\mathcal{SS}_{Total}$ attributed to factor "measured RMMA side" for an ANOVA. Defined in Eq. 10.

$\mathcal{SS}_{Total}$ Total sum of squares (SS) for an ANOVA. Defined in Eq. 9.

$\mathcal{D}_1$ The Durbin-Watson statistic computed on the sample of residuals for the registration time response.

$\mathcal{D}_2$ The Durbin-Watson statistic computed on the sample of residuals for the initial-to-final spiral search distance for $\vec{ap}_1$ or $\vec{ap}_3$ response.

$\mathcal{D}_3$ The Durbin-Watson statistic computed on the sample of residuals for the digital level readings taken from the front digital level.

$\mathcal{D}_4$ The Durbin-Watson statistic computed on the sample of residuals for the digital level readings taken from the side digital level.

$\mathcal{D}_L$ Lower bound of the critical values for the Durbin-Watson statistic for a given Durbin-Watson test. The null hypothesis of the Durbin-Watson test is rejected if the Durbin-Watson statistic is less than this value. If the Durbin-Watson statistic is between $\mathcal{D}_L$ and $\mathcal{D}_U$, the test is inconclusive.

$\mathcal{D}_U$ Upper bound of the critical values for the Durbin-Watson statistic for a given Durbin-Watson test. The null hypothesis of the Durbin-Watson test is not rejected if the Durbin-Watson statistic is greater than this value.

$\mathscr{d}_{abc}$ The standardized residual of a response variable observation (see definition of y_{abc}).

e_{abc} The residual of a response variable observation (see definition of y_{abc}).

$\mathcal{F}_0$ Denotes the F statistic of a given effect in an ANOVA, which is generally the mean square (MS) of the effect divided by the $\mathcal{MS}_{Error}$.

$\mathcal{H}_0$ Denotes the null hypothesis for a given hypothesis test.

$\mathcal{H}_a$ Denotes the alternative hypothesis for a given hypothesis test.

n_{ab} The total number of observations for the ath level of factor "measured RMMA side" and the bth level of factor "coordinate registration method". Since the experiment was unbalanced, but found to be proportional, this variable conforms to Eq. 8. Either 5 or 6 observations were recorded depending on the level of each factor.

$\mathcal{R}^2$ Coefficient of determination for a given linear regression fit.

y_{abc} The observed response variable for the ath level of factor "measured RMMA side", the bth level of factor "coordinate registration method", and the cth replicate of the corresponding factor level combination. The response variable, which corresponds to either the registration time or the initial to final spiral search distance for either AP_1 or AP_3 (see definition of $AP_1 - 4$), is modeled using a linear experimental model defined in Eq. 7.

μ The effect of the constant overall mean on the response (see definition of y_{abc} and Eq. 7).

$\mu_{front,rmmasq2}$ The population mean for the sample of digital level readings recorded on the "RMMASq2" side of the RMMA by the front digital level.

$\mu_{front,rmmasq3}$ The population mean for the sample of digital level readings recorded on the "RMMASq3" side of the RMMA by the front digital level.

$\mu_{side,rmmasq2}$ The population mean for the sample of digital level readings recorded on the "RMMASq2" side of the RMMA by the side digital level.

$\mu_{side,rmmasq3}$ The population mean for the sample of digital level readings recorded on the "RMMASq3" side of the RMMA by the side digital level.

τ_a The effect of the ath level of factor "measured RMMA side" on the response (see definition of y_{abc} and Eq. 7).

1. Introduction

Recent work has demonstrated both a continued, growing interest in the utilization of mobile manipulators towards commercial and industrial applications, as well as the need for standardized performance measurement methods. Mobile manipulators generally consist of a robotic arm mounted on a mobile base of varying levels of autonomy. For example, the mobility component can consist of an automatic guided vehicle (AGV) that follows pre-programmed paths or a mobile robotic platform that can re-compute routes around unexpected obstacles. The potential benefits of such systems have been noted for uses outside of manufacturing settings. For example, recent interest has been shown in using mobile manipulators for healthcare applications, such as contactless, curbside admission screening at hospitals and assisting with in-home care [1, 2]. However, even more critically, is that the addition of mobility allows the manipulator arm to engage in a wider variety of industrial applications. One example is applying mobile manipulators towards assembling, processing, surfacing, or prototyping large scale components such as wind turbines, aircraft, or ships [3]. Additionally, flexible manufacturing, the ability to tend multiple conveyors in distinct locations, and material handling also become possible [3]. Recently, interest has been demonstrated in using mobile manipulators to tend computer numerical control (CNC) machines, though it has been noted that the harsh, unstructured environmental conditions of workshops pose a challenge to the localization systems of the mobility component [4]. Furthermore, another potential application of mobile manipulators in manufacturing that has garnered recent interest centers on additive manufacturing (AM) [5]. Specifically, instead of using mobile manipulators to treat or assemble large scale components, such systems can allow for an expanded build volume in large-scale conformal AM [5]. However, poor accuracy and repeatability in the mobility component have been identified as challenges in using mobile manipulators for such applications [5]. These limitations highlight the need for standardized methods to characterize the uncertainty of mobile manipulator systems, which may further enable such systems to perform useful work towards manufacturing processes requiring a high degree of precision and accuracy.

The performance assessment of mobile manipulators has focused on measures reflective of "safety, precision, and accuracy" [6]. In the past, research predominantly emphasized manipulator tipover stability and the enhancement of coordination between the vehicle and robotic arm in various environments [6–8]. It was also noted that measurement systems existed to assess the individual sub components of a mobile manipulator. Examples of such systems include laser interferometers (non-contact) and artificial cues (contact-based) used to assess the performance of manipulator arms [6, 9, 10]. However, the performance measurement of mobile manipulators as a complete system represented a relatively new area of research [3]. As the potential application domains continue to expand, it becomes more important for users and manufacturers to ensure mobile manipulator accuracy, repeatability, and coordination [6, 11].

Therefore, the National Institute of Standards and Technology (NIST) has endeavored to advance measurement science pertaining to the performance of mobile manipulators

[12–14]. Past work included the development of the Re-configurable Mobile Manipulator Artifact (RMMA), which introduced a cost-effective, and flexible artifact for measuring mobile manipulator performance across numerous simulated manufacturing tasks and the use of an optical tracking system (OTS) to establish a ground truth reference of comparison to the RMMA [9, 15, 16]. Both measurement techniques were applied towards measuring both a mobile manipulator that consisted of an AGV and an autonomous mobile robot (AMR) for the mobile platform [6, 15, 17–19]. Additionally, the RMMA was used to compare coordinate registration methods for use with the mobile manipulators [20].

This project focused on addressing three experiments that advanced the previously described work. First, the artifact-based measurement methodology with ground truth reference was applied to a new type of mobile manipulator, the mobile manipulator-on-a-cart. The mobile manipulator-on-a-cart featured a vehicle capable of sensing and docking with a detachable cart payload structure. Rather than attach the manipulator directly to the vehicle, the manipulator was instead attached to the separable cart, as shown in Fig. 1. This type of mobile manipulator can potentially increase the flexibility and concurrency of workflows in addition to maximizing hardware utilization. For example, additional time and cost savings can result since the vehicle would be re-usable to transport other payloads while the manipulator-on-a-cart is engaged in an assembly task. Furthermore, the manipulator would no longer be reliant on a specific, individual vehicle for transportation between task locations. Potential challenges in measuring this system were expected to include new sources of performance uncertainty that might arise due to the lack of a constant alignment between the cart transporter and manipulator-on-a-cart coordinate systems. Additionally, uncertainty in the manipulator position was expected to be possible due to the instability introduced from the cart being on wheels.

Previous experiments compared three non-contact techniques for coordinate registration as applied on a mobile manipulator using an AGV [20]. This included laser-based fine (i.e., spiral search) and bisect methods (see Sec. 3.1.3 - 3.1.2) for localizing retro-reflective targets placed on the RMMA, as well as visual fiducials tracked via an augmented reality toolkit. More recently, experiments on the AMR used the same laser bisect method [6]. For the second part of the mobile manipulator-on-a-cart project, the primary interest was to introduce an additional, alternative technique for rapid coordinate registration to the mobile manipulator-on-a-cart system. Specifically, the speed and accuracy of the new coordinate registration technique, which used a non-contact, laser-based method to search for retro-reflective targets placed along the edges of the RMMA table surface, was compared against the previously used laser bisect technique.

The third part of this project investigated a limitation of previous experiments performed with the AMR [6]. Essentially, the data analysis techniques used for these prior measurements assumed that the three-dimensional (3D) positional data could be projected to 2D with negligible error. However, it was also suspected that the flooring may not have been uniformly level between the two docking locations used, which were positioned on opposite sides of the RMMA. By determining whether or not there was a significant difference in the cart leveling between the two docking positions for the mobile manipulator-on-

a-cart, improvements for future data analysis or calibrations can be recommended based on this knowledge.

First, the report provides an overview of the hardware, software, and configurations used for the mobile manipulator-on-a-cart platform, the RMMA, and OTS (Sec. 2). In Sec. 3, the experimental design is outlined by first detailing the bisect and edge coordinate registration methods to be compared and the spiral search localization method used to verify the accuracy of the coordinate registration as background. To ensure data correspondence between the OTS, robot controllers, and digital levels, system clock synchronization was applied. Additional information on how this synchronization was achieved is provided before detailing the test procedure itself. In Sec. 4, the analysis of the captured data is divided into three parts. First, while performing mock-assembly tasks, the position and orientation of the mobile manipulator-on-a-cart system captured from the OTS ground truth system was compared with the position and orientation collected from the system control computers, manipulator, and cart transporter vehicle logs. This section also includes an outline of the data extraction algorithms used to select and aggregate the data for the performed assembly tasks from each measurement technique (e.g., the OTS and computer/robot logs). Calibration methods were also needed to express the data in a common coordinate system. In the second part of Sec. 4, the report documents the comparison of the speed and accuracy of the bisect coordinate registration method and the new edge coordinate registration method. The comparison was conducted using an analysis of variance (ANOVA), with additional model adequacy checks provided to validate the reliability of the conclusions made. Additionally, plots displaying the sample average response per factor combination were examined. Finally, the third part of Sec. 4 documents the statistical inference techniques used to compare the two measured docking locations of the RMMA. Again, the specific goal was to determine if there was a significant difference in the cart leveling between the two measured docking locations next to the RMMA. In Sec. 5, the report concludes by summarizing and discussing the findings along with limitations and future work.

2. Platform and Operating Environment

Figure 1 provides a summary of the hardware sub-components utilized in the mobile manipulator-on-a-cart system[1], which will be detailed throughout this section. A complete network and software diagram is provided in Appendix A (Fig. 38).

2.1 Cart Transporter

The technical specifications for the cart transporter robot utilized for this work were provided by the manufacturer [21]. Similar to the AMR measurements [6], the cart transporter

[1]Certain commercial equipment, instruments, or materials are identified in this paper in order to specify the experimental procedure adequately. Such identification is not intended to imply recommendation or endorsement by the National Institute of Standards and Technology, nor is it intended to imply that the materials or equipment identified are necessarily the best available for the purpose.

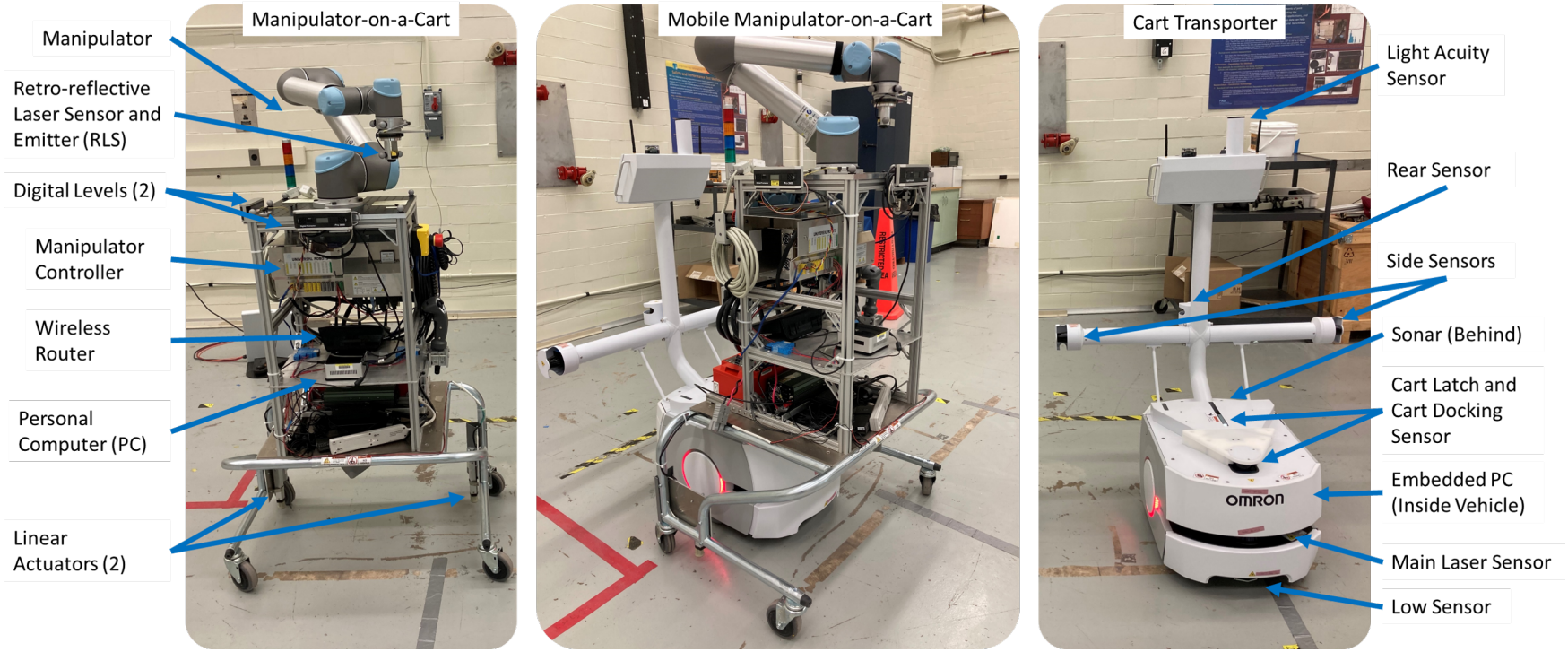

Fig. 1. The manipulator-on-a-cart and hardware components (left). The cart transporter docking with the manipulator-on-a-cart (center). The cart transporter vehicle (right).

utilized for this experiment was selected as an extension of previous work, which applied the performance measurement methodology to a mobile manipulator featuring an AGV [15, 17–19]. The AGV was restricted to using pre-specified paths while navigating between goals [15]. In contrast, the autonomy of the cart transporter featured in this work was more comparable to the AMR, since the cart transporter could also intelligently and autonomously compute routes and localize itself based on a user-configurable environmental map [6, 21].

Some key differences to the AMR included the additional sensors and mechanical components for detecting and latching onto the detachable cart, as well as an additional lower front sensor used to detect low, overhanging obstacles and negative obstacles [6, 21]. The lower front sensor was disabled for these experiments because the detection of uneven flooring as an obstacle hindered the cart transporter ability to navigate through the lab space. The environmental map of the lab, which will be referred to as the "cart transporter map", was generated by following the manufacturer-specified procedure [22]. This procedure involved manually driving the cart transporter through the lab space to scan key static room features, such as walls, using the on-board laser scanners. Additionally, the cart transporter map coordinate system utilized a 2-D, right-handed coordinate system as approximately shown in Fig. 2. The exact location of the map coordinate system origin within the lab was unknown (further addressed in Sec. 4.1.3), and the 3 DoF pose of the vehicle in the map consisted of a Cartesian position (along x and y axes) and a heading, θ. The poses were logged with a timestamp formatted in seconds since epoch [23]. Once the initial map of the lab was generated, the map was customized with goals and preferred lines, as shown in Fig. 2, which represented a preferred path for the vehicle to adhere to. Preferred lines were used to ensure safe navigation around the RMMA, as well as to guide the vehicle to the starting position of the cart (denoted as "CartDock1"). Two additional goal points, denoted "RMMASq2" and "RMMASq3" were placed on opposite sides of and facing the RMMA to allow the cart transporter to dock next to either side of the square reflector pattern (see Sec. 2.3). The commanded position for each of these goal points is shown in Table 1. Finally, an arbitrary goal point was added as the initial starting location for the cart transporter itself ("LDStart"). In contrast to the AMR [6], it should be noted that the cart transporter docked with the main safety laser scanner facing the RMMA. To prevent the vehicle from detecting the RMMA as an obstacle, each goal point intended for RMMA docking was placed approximately 1000 mm ahead of the final docking location next to the RMMA. After arriving at each goal point, the cart transporter was issued a "move straight" command with input parameters that set the distance to 1000 mm, the front clearance to 25 mm, and the speed to 150 mm/s. The other input parameters were kept at their default values. An example map that demonstrates this configuration is shown in Fig. 2.

The cart transporter[2] map was generated and configured using the manufacturer supplied software (version 4.5.2) running on a Windows 7, 64-bit laptop [22]. Additionally, custom C++ code for sending clear-text commands to the cart transporter over Transmis-

[2]The on-board cart transporter software included controller firmware version 1.9.0d, manufacturer software operating system version 4.8.0, and automation management software version 4.9.9.

sion Control Protocol / Internet Protocol (TCP/IP) sockets was implemented by using the same code written as part of previous experiments as a starting point [6]. Two modes of communication with the client application were supported by the cart transporter [22, 23]. The first mode of communication followed a client-server model in which one or more client applications sent pre-defined commands to the cart transporter server. Once the TCP/IP connection was established, the client applications could send pre-defined commands to the cart transporter, which either executed the command or responded with the queried data (such as the current vehicle pose) [23]. In the second mode of communication, the cart transporter could be configured to continuously execute a given command or set of commands on a user-specified interval. The cart transporter, which then acted as the client, forwarded the result of these commands to an external application that acted as the server. Most importantly, however, was that if a set of commands were configured to run using this method, then they were executed in the same computation cycle by the cart transporter [23]. Therefore, to ensure data synchronization, the second mode of communicating with the cart transporter was used to query the current vehicle pose. The time interval to generate the pose messages was set to 0.01 seconds. To provide further assurance of data synchronization, the system clock of the cart transporter was synchronized via Network Time Protocol (NTP) (see Sec. 3.2 for details).

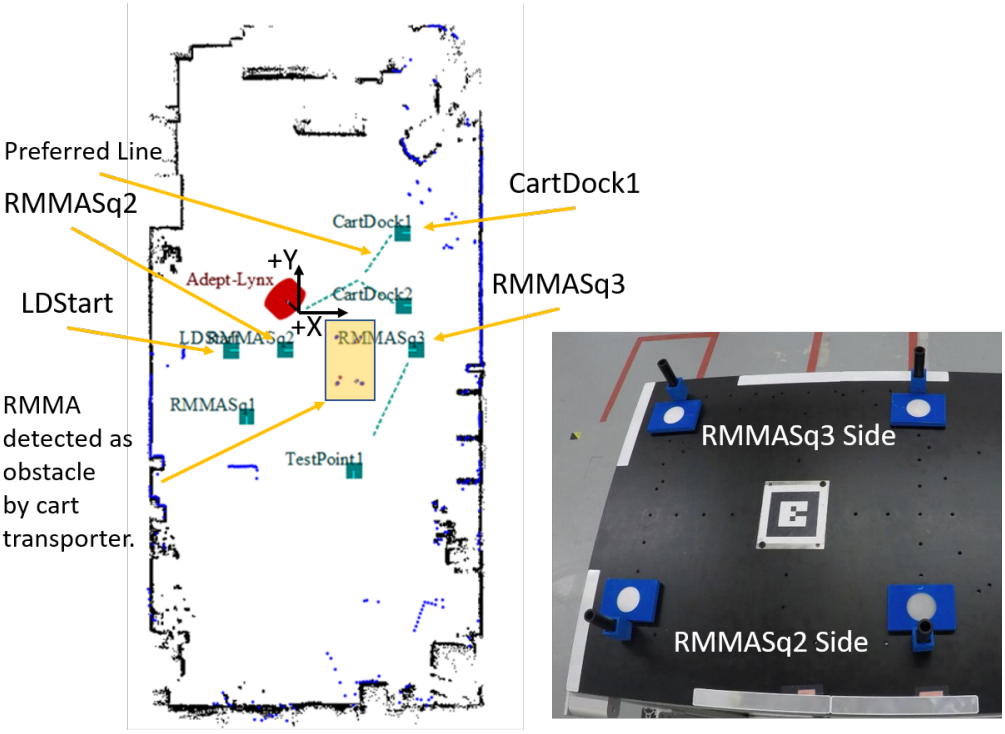

Fig. 2. Cart transporter map of the lab space as configured with goal points and preferred lines (left). Note that the approximate location and orientation of the map coordinate system origin is annotated. The docking locations next to the RMMA that corresponded to the goal points (right).

Table 1. Commanded position of the goal points used to dock the cart transporter to the RMMA. Note that the positions shown here are 1000 mm away from the RMMA in the x direction. A "move straight" command was issued to the cart transporter after reaching each goal point to allow the cart transporter to dock closer to the RMMA without detecting it as an obstacle.

Goal	x	y	θ
RMMASq2	-50 mm	-792 mm	0°
RMMASq3	3494 mm	-788 mm	180°

2.2 Manipulator-on-a-Cart

A manipulator, which was the same manipulator used in prior experiments, was mounted to a custom-built payload structure and fixed to the detachable cart [6]. According to the manufacturer specification, the maximum reach and repeatability of the manipulator arm was 850 mm and 0.1 mm, respectively [6, 24]. The manipulator controller software ran version 3.1.18213 and used a 3D right-handed coordinate system in which the x and y axes of the origin (placed at the center of the manipulator base) were defined parallel to the ground plane while the z axis was defined perpendicular to the ground plane (e.g., the up/down, or the vertical direction). Since the manipulator base was mounted at a rotational offset of 135° from the front of the cart payload structure, the rotation offset was corrected such that the positive direction of the x axes aligned with the front of the cart payload structure. As with prior experiments, the short reach of the manipulator, which was less than that of the manipulator arm used in the prior experiments with the AGV [15], restricted the arm from being able to access the entire RMMA table surface from a single docking location. This restriction necessitated the use of multiple dock points to allow the manipulator full access to the assembly points required for the test. To digitally detect retro-reflective targets, which served as mock-assembly points on the RMMA, a retro-reflective laser sensor and emitter (RLS) was attached to the end-of-arm tool (EOAT) of the manipulator and is shown in Fig. 3 [25]. Use of the RLS for non-contact registration and localization reduced the risk of collision with the RMMA and resembled the task of classic peg-in-hole assembly [17]. Communication with the manipulator controller was facilitated by connecting the RLS to the tool I/O port. To perform the registration and localization techniques, custom software was written using the code from prior experiments as a starting point [6]. The code used the Collaborative Robot Programming Interface (CRPI) and small portions of the NIST Real-time Control System (RCS) library that pertained to pose format conversions [26, 27], and the manipulator base rotation misalignment was corrected by specifying the 135° offset in an Extensible Markup Language (XML) configuration file. Additionally, the User-Level Application Programming Interface (ULAPI), which was packaged with CRPI, was utilized to implement multi-threading and synchronization, as well as additional TCP/IP socket communications [28]. The detachable cart was outfitted with two linear actuators (see Appendix C for detailed specifications), which were added to prevent the cart from moving after it had been docked next to the RMMA. CRPI was used to change the digital output state such that each linear actuator could be independently set to extend

to a fixed, constant distance.

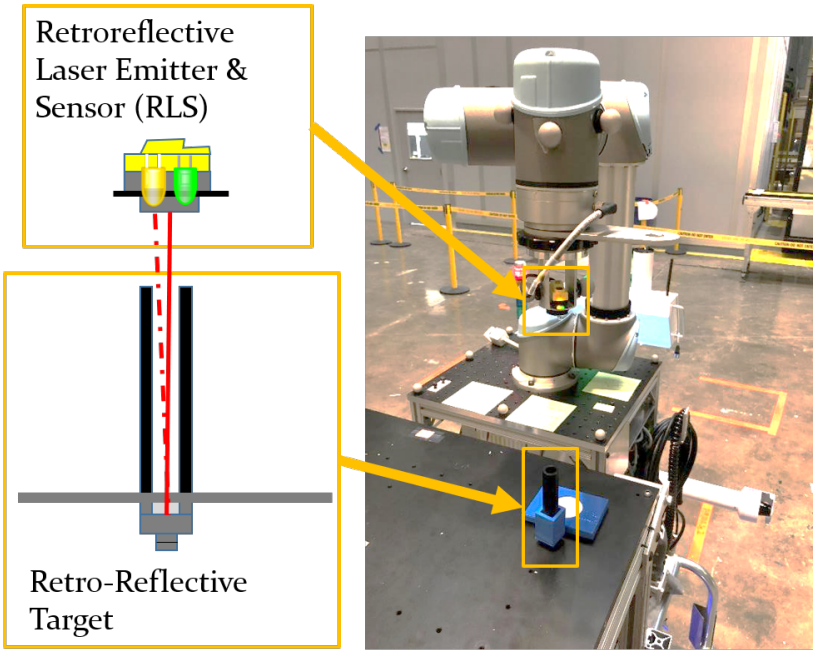

Fig. 3. The manipulator used an RLS to digitally detect a retro-reflective target [29].

Additionally, the pior experiments that used the AMR indicated that one source of uncertainty could have stemmed from inconsistent floor leveling that was present throughout the lab [6]. To further investigate this, two digital levels were mounted along two sides of the optical breadboard that also supported the manipulator arm. Each level, which outputted angles between $\pm 180°$, inclusive, was specified to have an accuracy of $\pm 0.05°$ when the level was between $0°$ and $10°$ and a repeatability of $\pm 0.05°$ [30]. Each level was connected to a Windows 7 computer using the RS232 serial output of the digital levels (details in Appendix B) and calibrated according to the manufacturer-specified procedure before use [30]. Terminal emulation software, installed on the on-board computer, was used to read the serial output and to log the digital level readings to a clear-text output file [31]. Wireless remote access to the on-board computer was achieved to manually start and stop the digital level recordings via the terminal emulation software [32]. Once connected, the digital level was able to transmit readings every 533 msec over RS232 using a 9600 baud rate, no stop bit, and no parity [30]. All of the hardware placed on the cart (with the exception of the digital levels) was powered by a 900 W, 24 V DC to AC power inverter connected to two 12 V, 28 Ah batteries [33, 34].

2.3 RMMA

The RMMA (Fig. 4) consisted of machined, anodized aluminum and was re-configurable in the sense that it allowed for an adjustable height, table surface rotation, and geometric

configuration of drilled, tapped mounting holes (for example, a square, circle, or sinusoid). The pre-defined, user-specified uncertainty allowed for comparison to a ground truth reference [15]. As with the previous studies, the RMMA was used for the "indexed" case in which the cart transporter incremented between a set of discrete, finite stops placed next to the RMMA [6, 15].

Three different types of reflective targets that were detected by the mobile manipulator are shown in Fig. 4. Each type of target was used for a different coordinate registration and/or localization method, which are further detailed in Sec. 3.1.1 - 3.1.3. Eight strips of reflective tape were used for the edge coordinate registration method, which was named for the process of detecting the outer edges of the 203.2 mm x 25.4 mm tape. The four circular, 42 mm diameter reflectors were denoted $\vec{lr}_1$, $\vec{lr}_2$, $\vec{lr}_3$, and $\vec{lr}_4$ (with "lr" standing for "large reflector") and were used for the bisect coordinate registration method. Finally, four 3 mm diameter reflectors, which were located within the light collimators depicted in Fig. 4 and were denoted $\vec{ap}_1$, $\vec{ap}_2$, $\vec{ap}_3$, and $\vec{ap}_4$ (with "ap" standing for "assembly point"), were used for the spiral search localization method. The spiral search localization was performed after each coordinate registration to verify the accuracy of the coordinate registration. The $\vec{ap}$ reflectors were arranged in a square with side length 457 mm. However, as mentioned in Sec. 2.2, the limited arm length of the manipulator restricted the ability to access all reflective targets from any one side of the RMMA. Therefore, when the manipulator was docked at the "RMMASq2" goal point, the arm could only reach $\vec{lr}_1$, $\vec{lr}_2$, $\vec{ap}_1$, and $\vec{ap}_2$. Similarly, when the manipulator was docked at the "RMMASq3" goal point, the arm could only reach $\vec{lr}_3$, $\vec{lr}_4$, $\vec{ap}_3$, and $\vec{ap}_4$.

2.4 Optical Tracking System

The optical tracking system (OTS) used the same technical specifications and configuration that was utilized in prior studies, with the exception of using the then-current version of the manufacturer-supplied software (version 2.2) [6, 35]. The system comprised of 20, 4 Megapixel (MP) resolution cameras positioned to observe as much of the 9000 mm x 22000 mm x 7000 mm (width x length x height) laboratory space as was possible. Eight of the 20 cameras were focused directly on the RMMA, with one of these cameras mounted to the ceiling above to provide a direct, overhead view of the RMMA [6]. The system was recalibrated using the manufacturer-specified procedure immediately prior to measurement, and the results of this calibration as reported by the manufacturer-supplied software are shown in Fig. 5 [36]. As noted in Fig. 5, the corresponding mean error of the calibration was reported by the software to be 0.720 mm, which was indicated in the name of the generated calibration file. In addition to an assortment of other fabric coverings, paper tape covers, shown in Fig. 4, were used to assist in masking extraneous reflections when calibrating the OTS and recording static ground truth reference measurements of the RMMA reflective target locations. Furthermore, the OTS coordinate system was defined during calibration by using a square artifact to set the ground plane. The OTS used a 3D right-handed coordinate system in which the x and z axes of the origin were defined parallel to

the ground plane while the y axis was defined perpendicular to the ground plane (e.g., the up/down, or the vertical direction) [36, 37].

The rigid body tracking of the OTS was used for ground truth measurement. For the placement of the retro-reflective optical tracking markers, several factors needed to be considered. To avoid occlusions, but also allow for the tracking of finer movements, such as those performed as part of the coordinate registration and localization methods, suitable sized markers were needed. Ultimately, markers of 19 mm diameter were selected. Furthermore, the selected placement of the markers was intentionally asymmetric, which assisted in the labeling process used by the motion capture system [38]. Furthermore, for the markers placed on the EOAT, it was important to assure that the markers were not placed across different links of the robot (i.e., with a robot joint, such as the wrist, between any two markers). This was because the motion capture software assumed that the markers of a rigid body maintained a constant spatial relationship to the other markers in the rigid body (e.g., the rigid body cannot be deformed). Therefore, the rotation of the wrist joint could result in markers becoming unlabeled from the rigid body [39]. Finally, prior experiments had established the static (e.g., when the rigid body is not in motion) uncertainty of the OTS positional tracking to be 0.022 mm and the dynamic (e.g., when the rigid body is in motion) positional tracking uncertainty to be 0.26 mm [15, 16].

Figures 6 - 9 show the marker placement and labeling for the four defined rigid bodies in the OTS coordinate system. Note that the rigid body in Fig. 6 was used to acquire static measurements of the RMMA and retro-reflective target positions for ground truth reference, while the rigid body in Fig. 9 was used to measure the RMMA during the experimental trials. Therefore, markers M2, M4, M11, M13-M16, and M19 in Fig. 6 were not present in the rigid body shown in Fig. 9 because they were replaced with the appropriate retro-reflective targets. The data output for each frame contained a timestamp, frame number, quaternion rotation (with components q_x, q_y, q_z, and q_w as defined in see Eq. 16 - 18, Appendix D), Cartesian position (with components along the x, y, and z axes), and mean marker error associated with each rigid body centroid. Additionally, a quaternion rotation, position, and marker quality for each marker associated with each rigid body was also recorded. Data captures were recorded at 120 frames-per-second (FPS) and exported in Comma Separated Value (CSV) format.

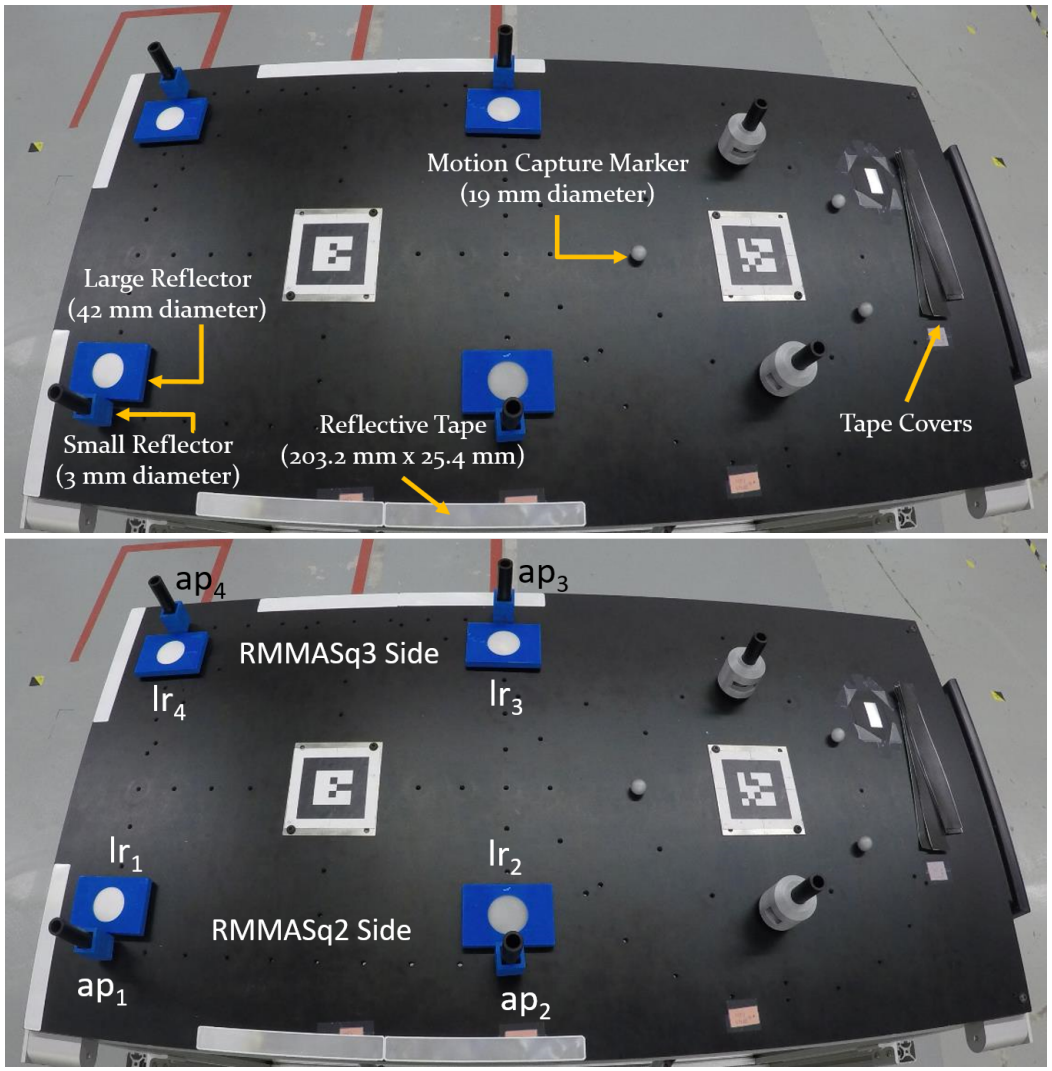

Fig. 4. The Re-configurable Mobile Manipulator Artifact (RMMA), retro-reflective targets, and OTS markers (top). Retro-reflective target labeling on the RMMA used for bisect registration and spiral search localization (bottom).

Calibration Summary	
Overall Result	Exceptional
Maximum Error (px)	0.223
Minimum Error(px)	0.099
Average Error (px)	0.157
Wand Error (mm)	0.082
Calculation Time	0:52

Fig. 5. Screenshot of the OTS calibration summary as reported by the manufacturer-supplied software. The corresponding mean error was 0.720 mm.

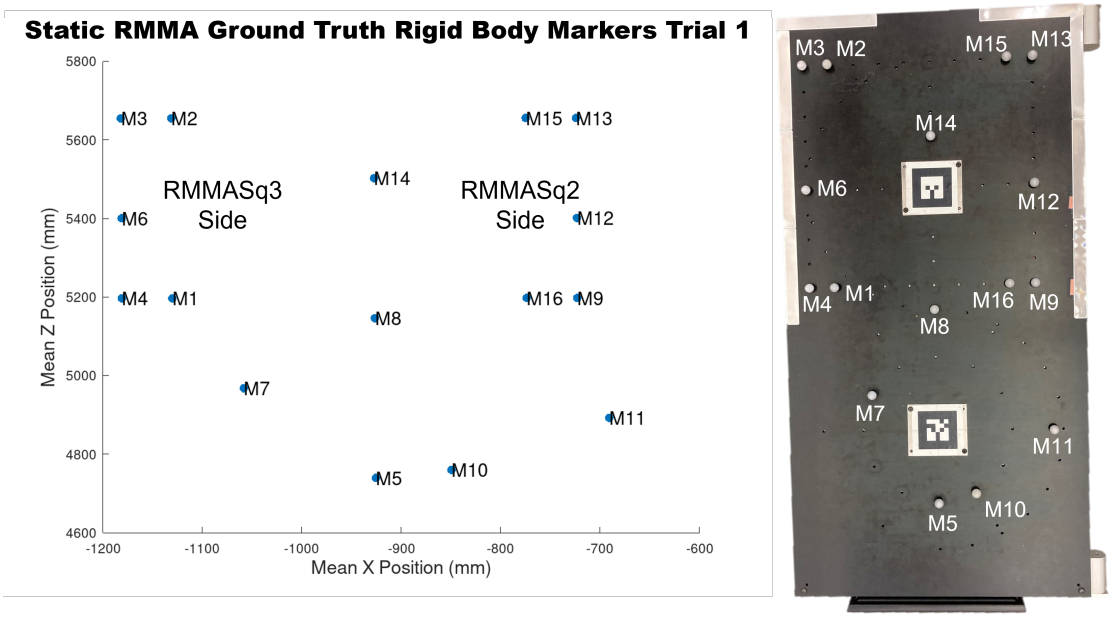

Fig. 6. Example 2D plot of average position and labeling of OTS markers for static RMMA ground truth measurements, as extracted from the OTS (left). Corresponding marker position and labeling on the RMMA (right).

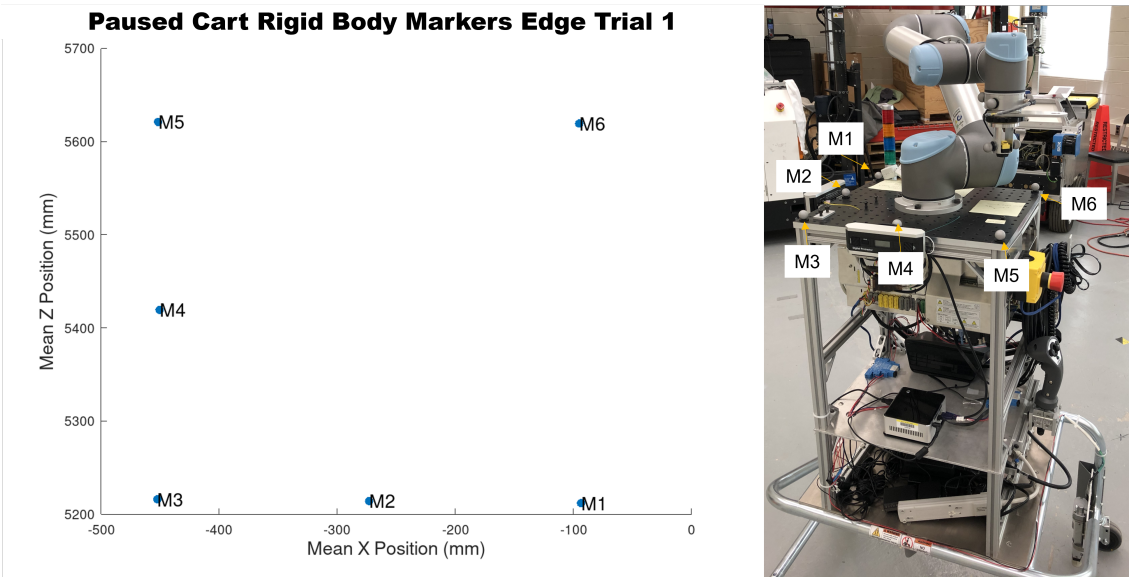

Fig. 7. Example 2D plot of average position and labeling of OTS markers for cart base measurements, as extracted from the OTS (left). Corresponding marker position and labeling on the cart base (right).

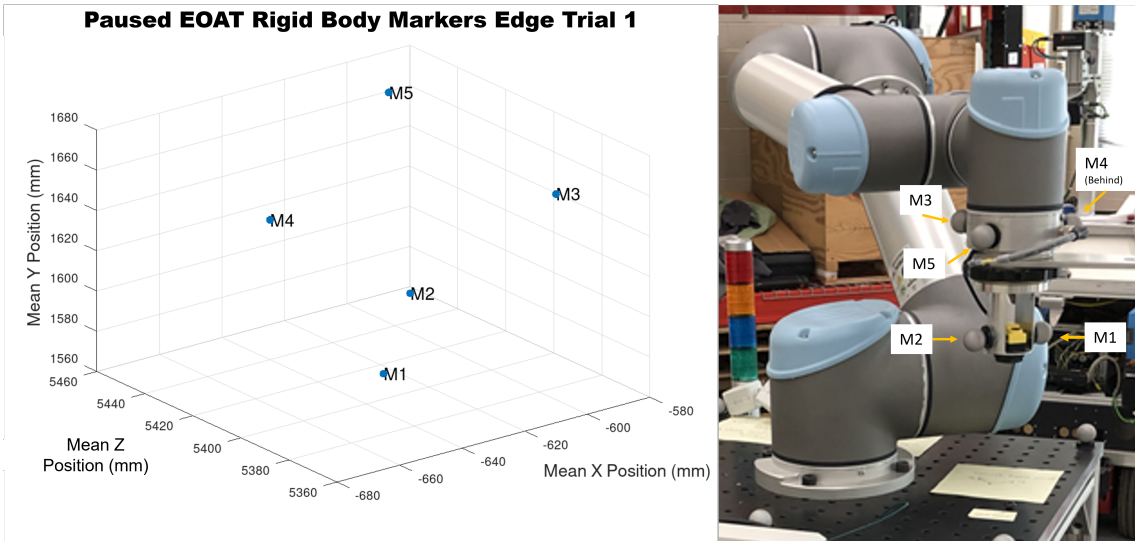

Fig. 8. Example 2D plot of average position and labeling of OTS markers for EOAT measurements, as extracted from the OTS (left). corresponding marker position and labeling on the EOAT (right).

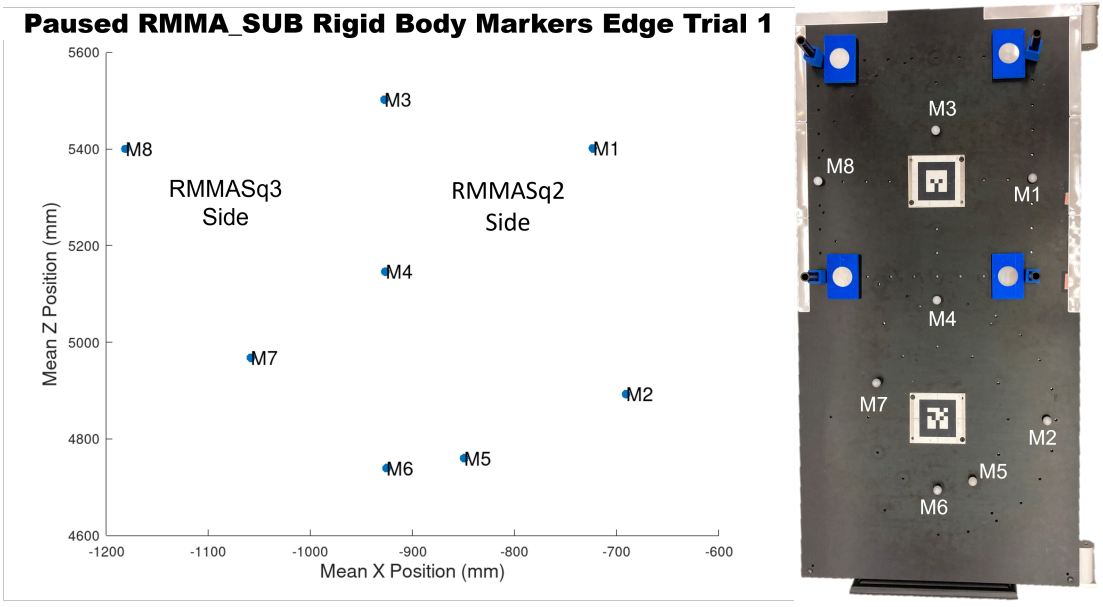

Fig. 9. Example 2D plot of average position and labeling of OTS markers for RMMA measurements during experiments (denoted as the "RMMA Sub" rigid body), as extracted from the OTS (left). Corresponding marker position and labeling on "RMMA Sub" (right).

3. Experiment Design

In this section, the experimental design and procedure are described. First, background details are included on how the two coordinate registration methods and the spiral search localization operated. Then the steps taken to ensure that data across the multiple systems was aligned via time synchronization is discussed. Finally, the experimental procedure itself is outlined.

3.1 Background

3.1.1 Edge Registration

Fig. 10 provides an overview of the edge coordinate registration algorithm. The edge registration method searched for a corner of the RMMA using three, 2D reference points ($\vec{r}_1$, $\vec{r}_2$, and $\vec{r}_3$) located on the edges of the reflective tape. For the purpose of this description, each reference point is defined to correspond with the Cartesian position of the EOAT relative to the base of the manipulator when the EOAT detected the edge of the reflective tape using the RLS. To complete the registration, the reference points were used to solve for the intersection of two perpendicular lines that outlined the edges of the RMMA table surface, as shown in Eq. 1-3. Reference points $\vec{r}_1$ and $\vec{r}_2$ were also needed to determine the orientation offset between the manipulator base and the RMMA in a similar manner as the bisect registration method used and documented in prior work [6, 18–20, 40].

$$m = \frac{\vec{r}_2.x - \vec{r}_1.x}{\vec{r}_2.y - \vec{r}_1.y} \tag{1}$$

$$\vec{corner}.x = m(\vec{corner}.y) + b_1 \tag{2}$$

$$\vec{corner}.x = -\frac{1}{m}(\vec{corner}.y) + b_2 \tag{3}$$

To locate each reference point, three steps of manipulator movements were used. In the first step (step a.), the arm continuously panned the EOAT backwards from an arbitrary stage position towards the base of the manipulator. The RLS input / output (I/O) was repeatedly polled to determine if the retro-reflective tape placed at the edge of the table had been detected. When the tape was detected, an interrupt was sent to the manipulator controller in the form of a CRPI command that moved the robot arm to its current position. If the tape was not detected by the RLS, the manipulator would continue panning towards the robot arm base until the current position of the EOAT was over the cart payload structure. The arm would then pan away from the robot arm base a maximum distance (101.6 mm away from the original stage position) to search for the tape in the opposite direction. In the next step (step b.) the manipulator instead moved in larger discrete steps (2 mm). However the manipulator still panned in the direction towards its base until the retro-reflective tape was no longer detected. Finally, the manipulator panned in smaller, discrete steps (0.25

mm) away from its base until the RLS detected the edge of the tape. For $\vec{r}_2$ the initial direction of step a. was reversed. Additionally, the continuous pan (step a.) for $\vec{r}_3$ was adjusted using the slope, m, defined in Eq. 1. This ensured that any angle offset between the cart and RMMA did not result in the wrong tape being detected by the RLS.

The following data pertaining to the edge coordinate registration method were captured from the manipulator controller using CRPI as well as the laptop running the custom control software. This information included the amount of time, in seconds, taken to find each reference point ($\vec{r}_1, \vec{r}_2, \vec{r}_3$) and the corner point (which was taken as the sum of the times to locate each reference point), and the starting and ending pose of the EOAT when locating each reference point and the corner point. It should be noted that the timestamps were obtained from the laptop system clock and the time to search included any time duration in which the control program was actively reading the status of the RLS to search for the retro-reflective surface. Here, the manipulator pose was expressed as a position vector (with components along the x, y, and z axes) in mm and an XYZ Euler angle rotation vector in degrees of the EOAT relative to the manipulator base. The conversion of a rotation expressed as an XYZ Euler angle to a quaternion representation is presented in Appendix D. Also included were the integer number of large, 2 mm steps and small, 0.25 mm steps taken to locate each reference point, in addition to integer flags that indicated which reference point was being located and whether or not the reference point was successfully found.

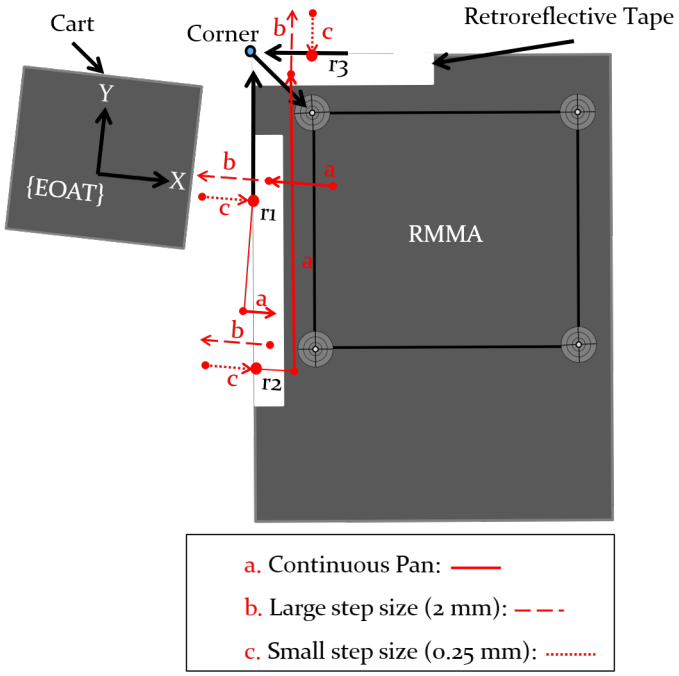

Fig. 10. Diagram summarizing the edge coordinate registration method. Three reference points ($\vec{r}_1$, $\vec{r}_2$, and $\vec{r}_3$) on the retro-reflective tape were located using the RLS to determine the position and orientation offset between the cart base and the top corner of the RMMA.

3.1.2 Bisect Registration

The same bisect coordinate registration method utilized in previous experiments was also used for this experiment [20]. On each side of the RMMA, two large (42 mm diameter) targets were fixed to the RMMA as pictured in Fig. 4. With the bisect method (pictured on the right of Fig. 11), it was initially assumed that the RLS was positioned over the retro-reflective material of the target, though not necessarily at the center of the target. The manipulator would trace four lines along two perpendicular axes of the target, which searched for the outer boundary of the target using the RLS. A step size of 0.5 mm was used [20]. By using the offset between the initial position of the EOAT and the outer boundary, the center of the reflector in manipulator base coordinates could be computed. This determined the positional offset between the manipulator base and the other $\vec{ap}$ reflectors. By localizing the center point of two, colinear $\vec{lr}$ targets (Ex. $\vec{lr}_1$ and $\vec{lr}_2$ when the manipulator was docked at the "RMMASq2" goal point), an angle offset between the cart and the RMMA could also be computed.

As in previous work, initial search points (expressed in the manipulator base coordinates) were recorded for each target and stored in a configuration file to be read by the CRPI-based manipulator control program at runtime [6]. Despite the pre-specification of these initial search points, sources of uncertainty in the mobile manipulator-on-a-cart system, such as in the cart transporter pose perception, in the cart latch mechanism, or due to manipulator repeatibility, among others, could cause the manipulator to deviate from the target position and necessitate a localization search. The initial search point was recorded using the following procedure at each goal point. First, the vehicle was used to dock the cart next to the RMMA at the given goal point. Next, the current vehicle pose upon docking (after completing the move straight command, but before detaching from the cart) was recorded in the configuration file. The manipulator was then manually jogged such that the RLS laser was positioned over the center of each $\vec{lr}$, with each position being recorded in the configuration file. These pre-taught points for the EOAT and poses for the cart transporter are shown in Table 2. Note that the manipulator points and the vehicle heading presented in the table were rounded to the nearest thousandth for readability. However, the manipulator controller and vehicle controller reported these values to six decimal places. The vehicle x and y coordinates were not rounded because they were reported by the vehicle controller to three decimal places. Additionally, the EOAT points are expressed in terms of the manipulator base coordinate system, and the cart transporter poses are expressed in terms of the cart transporter map coordinate system. When the bisect coordinate registration routine began, the initial search point for each $\vec{lr}$ was transformed using the vehicle pose at the time of recording to express the initial search point in vehicle coordinates. Finally, this initial search point was then inversely transformed using the current vehicle pose. This transformation attempted to adjust the initial $\vec{lr}$ search points to account for variation present in repeatedly docking the vehicle at the same goal point.

It was possible, however, that the size of the variation in the vehicle docking could exceed the size of each $\vec{lr}$ target. In this case, a large square spiral pattern, which is pictured on the left of Fig. 11 and referred to as a "Coarse Spiral Search", was used prior

Table 2. The pre-taught initial search points (top) and corresponding vehicle poses (bottom) used for the bisect coordinate registration method. Note that the points/poses are rounded to the nearest thousandth, the EOAT points are expressed in terms of the manipulator base coordinate system, and the cart transporter poses are expressed in terms of the cart transporter map coordinate system.

Manipulator EOAT Point			
Side	*Target*	x	y
RMMASq2	$\vec{lr}_1$	472.041 mm	254.375 mm
RMMASq2	$\vec{lr}_2$	461.336 mm	-203.981 mm
RMMASq3	$\vec{lr}_3$	471.185 mm	252.572 mm
RMMASq4	$\vec{lr}_4$	461.994 mm	-203.444 mm
Cart Transporter Pose			
Side	x	y	θ
RMMASq2	966.188 mm	-828.645 mm	2.238°
RMMASq3	2468.470 mm	-793.242 mm	−177.936°

to attempting the bisect registration method as was done in previous experiments [6]. The coarse spiral search used the same search pattern as the fine spiral search and the same maximum radius of 75 mm. However, the coarse spiral search instead used a larger step size of 10 mm, which was the same step sized used for the coarse spiral search in previous experiments [6].

Data were also collected using CRPI and the laptop running the custom control software. Like the data captured for the edge registration, all manipulator poses were expressed as a position vector (with components along the x, y, and z axes) in mm and an XYZ Euler angle rotation vector in degrees of the EOAT relative to the manipulator base. If the coarse spiral search was needed, the start and end pose of the EOAT when locating each $\vec{lr}$, the time elapsed during the search in seconds, the integer number of steps taken in the search pattern, and additional flags indicating whether or not the search was successful were logged. For the bisect method, the starting and ending pose of the EOAT when locating the center point of each $\vec{lr}$, the elapsed time to locate the center point of each $\vec{lr}$ during the coordinate registration in seconds, the number of steps taken in the bisect search pattern, and additional flags indicating whether or not each $\vec{lr}$ was successfully found were logged. As with the edge registration method, the elapsed search time included any duration in which the control program was actively reading the status of the RLS.

3.1.3 Fine Spiral Search Localization

As mentioned in Sec. 2.3, a square spiral search pattern (pictured in Fig. 12) was used to localize the 3 mm diameter target $\vec{ap}$ reflectors and served to verify the accuracy of the previously described coordinate registration methods. The spiral search pattern used the same maximum radius of 75 mm and the same step size of 0.5 mm as was used in previous experiments with the AGV and the AMR [6, 15].

The following data related to the spiral search pattern were also collected using CRPI

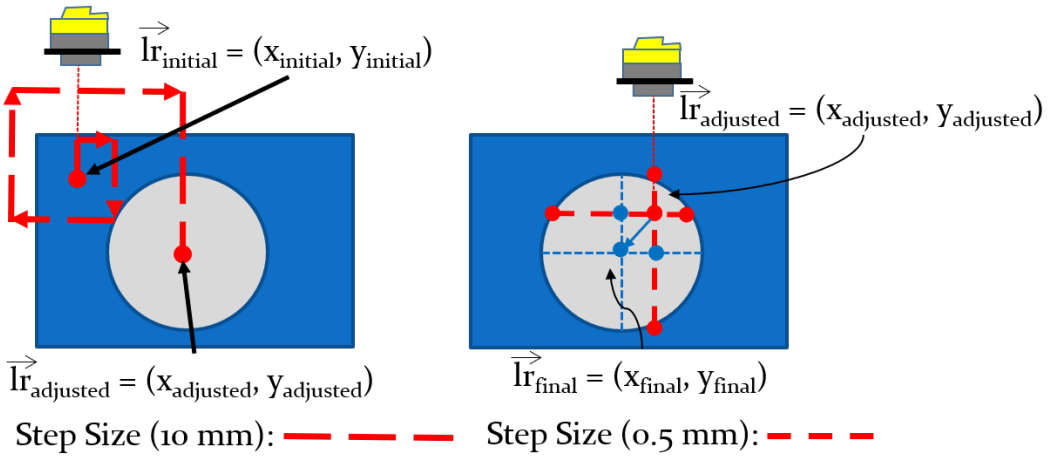

Fig. 11. The coarse spiral search localization method (left). The bisect coordinate registration method (right). $\vec{lr}_{initial}$ is an example initial point requiring coarse spiral search localization, $\vec{lr}_{adjusted}$ is an example point returned after coarse spiral search localization, and $\vec{lr}_{final}$ is an example point returned after bisect registration.

and the laptop running the custom control software. As with the edge and bisect coordinate registration methods, all manipulator poses were expressed as a position vector (again, with components along the x, y, and z axes) in mm and an XYZ Euler angle rotation vector in degrees of the EOAT relative to the manipulator base (again see Appendix D for a quaternion representation conversion). The starting and ending pose of the EOAT (used to compute the initial-to-final search distance), the elapsed search time in seconds for each $\vec{ap}$ point, the integer number of steps taken in the spiral search pattern when searching for each $\vec{ap}$ point, and additional flags indicating whether or not each $\vec{ap}$ point was successfully found were logged.

3.2 Time Synchronization

As mentioned in Sec. 1, time synchronization across clients was important for ensuring the data captured from the computer running the OTS software could be aligned with both the data captured from the robot logs and digital levels. Time synchronization was achieved using a Stratum 1 NTP time server with an integrated global positioning system (GPS) receiver. The time server was connected to a switch (as shown in Fig. 38) via power over Ethernet (POE) and distributed time over NTP to the local area network (LAN) in broadcast mode. The time server was synchronized within approximately 1 μs of Coordinated Universal Time (UTC), United States Naval Observatory (USNO)). Each synchronization client was within three hops of the time server. The integrated antenna, receiver, and time server were located on the roof of the lab space with good line of sight of typically 11 satellites. Note that "hops" refers to the number of switches or routers between a communication source and destination [41]. Unlike past experiments with the AMR, which used

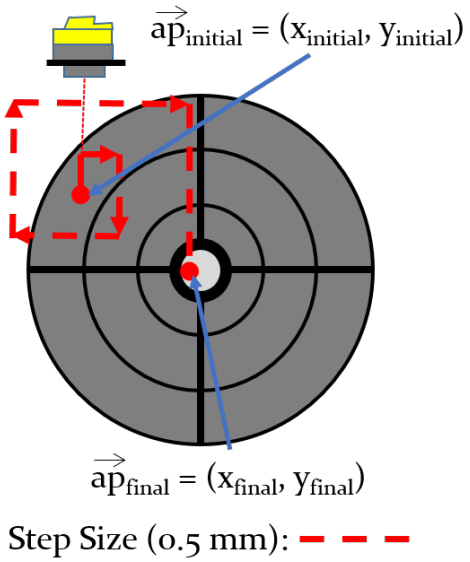

Fig. 12. Diagram of the square, spiral search localization method. $\vec{a}p_{initial}$ is an example initial point before localization and $\vec{a}p_{final}$ is an example point returned after localization.

an NTP server synchronized over the Internet, synchronization to the local time server minimized the number of intermediate nodes and therefore reduced the path delay variability in the time distribution of the experimental setup. [6].

The time server synchronized with the following computers using publicly available software [42]. The computer running the OTS software was synchronized over wired connection with a delay variability of approximately within 0.1 s (as reported by the software). The control laptop controlling the vehicle and manipulator arm was synchronized over a wired connection. The on-board cart PC used to record the digital level readings was synchronized over two wireless hops. Finally, the cart transporter controller was synchronized over two wireless hops without requiring additional software. Note that the manipulator controller clock was not directly synchronized because it did not support NTP and that previous studies have shown increased jitter (i.e., transmission delay variability) in wireless hops, which can impact time synchronization precision [43]. While the laptop delays could be estimated by the NTP client software, the synchronization precision of the cart transporter was not readily verifiable. Since the cart transporter and control laptop may have only been synchronized with an estimated 1 s delay variability, data analysis was limited to tracking the static rigid bodies only. Future improvements planned for this configuration includes the minimization of the number of hops between the nodes and devices, which can be assisted through the further aggregation of the sensors and data capture to a few computer nodes. Additional improvements include exploring the use of an access point that supports Synchronous Network Time Protocol (SNTP) for wireless synchronization of clients and utilizing Precision Time Protocol (PTP) to synchronize the computer running the OTS software. This could allow for future data analysis to include examination of

dynamic performance.

3.3 Test Procedure

This section details the experimental procedure used to collect data from the OTS, robot controller logs, and the digital levels. First, static measurements of the RMMA with markers configured as shown in Fig. 6 were taken prior to measurement. In total, five static recordings, each containing ten seconds of continuous data, were captured. As mentioned in Sec. 2.4, these recordings were used to establish a ground truth reference for the positions of the $\vec{lr}$ and $\vec{ap}$ reflectors for later comparison with the actual detected position of the EOAT over these targets. The cart transporter was initially parked at an arbitrary home location (i.e., the "LDStart" goal point). The manipulator-on-a-cart was also initially docked ahead of an arbitrary location (i.e., the "CartDock1" goal point). Upon starting the control programs outlined in the previous section, the cart transporter proceeded to the initial docking location of the manipulator-on-a-cart. The cart transporter then docked with and latched to the cart. Next, the cart transporter parked at the "RMMASq2" goal point. Upon reaching the goal, the cart transporter executed the 1000 mm straight move command to approach the RMMA. At this point, right before the cart transporter unlatched from the cart, the current vehicle pose was logged and sent to the manipulator control code. At the same time, an operator started recording data from the OTS.

With the manipulator-on-a-cart now unlatched from the cart transporter, the actuated feet descended to keep the cart in place. The manipulator-on-a-cart paused for 15 seconds, during which an operator manually started recording data from each digital level. When the 15 second pause had concluded, the operator stopped recording digital level data and the manipulator began to move out of its stow position through three intermediate stage poses to allow access to the RMMA. After the final stage position had been reached, the manipulator EOAT height was kept fixed at 297 mm above its base, and the EOAT was kept facing directly downward towards the floor, which corresponded to constant rotation of 180° about the x axis of the manipulator base coordinate system (see Appendix D for quaternion conversion). After staging, the manipulator performed the edge registration and subsequently performed verification by using the spiral search localization on two of four, colinear 3 mm diameter reflective targets positioned at the corners of the square on the RMMA. For example, if the manipulator was docked at the "RMMASq2" goal point, $\vec{ap}_1$ and $\vec{ap}_2$ were localized, but if the manipulator was docked at the "RMMASq3" goal point, $\vec{ap}_3$ and $\vec{ap}_4$ were localized. It should be noted that, upon locating each retro-reflective target for coordinate registration and spiral search verification, an additional 15 second pause was included. This was included to further minimize the impact of any latency in the time synchronization of data and to assist with the OTS data selection methods (see Sec. 3.2 and 4.1.1). A second verification was then performed on the other 3 mm diameter reflector at the opposite corner of the square. The control program for the manipulator automatically logged the needed data upon completion of the second verification, the manipulator stowed, and the OTS recording was stopped and re-started. The manipulator then paused

for 15 seconds and performed the same steps again without re-docking the cart or lifting the actuated feet. However, the bisect registration was then substituted for the edge registration and there was no digital level recording during the initial 15 second pause. After completing and verifying both coordinate registration methods, the cart transporter re-docked and latched to the cart. The cart transporter then docked the cart at the other side of the RMMA (i.e., at "RMMASq3").

This process of alternating between stops and performing both registration methods at each stop without re-docking continued until the manipulator battery depleted. In total, 11 valid trials of data, or 22 total observations, were captured (with data capture anomalies documented in Appendix E). This included five to six replicates per treatment combination that consisted of the measured RMMA side (i.e., "RMMASq2" or "RMMASq3") and/or the coordinate registration method (i.e., Edge or Bisect) were captured. Six trials were captured at the "RMMASq2" side for both coordinate registration methods and five trials captured at the "RMMASq3 side" for both coordinate registration methods. The cart batteries ran out just before a sixth trial could be obtained on the "RMMASq3" side of the RMMA, as explained in Appendix E. Note that, in an ideal case, the reliability of applied inferential statistical techniques for data analysis (such as two-sample comparison tests and two factor factorial analysis) could be improved by randomly assigning treatment combinations to each run. For example, randomly choosing a goal point ("RMMASq2" or "RMMASq3") and randomly choosing a registration method (Edge or Bisect). However, the time required for each coordinate registration method and spiral search verification combined with the limited battery life of the manipulator restricted the ability to implement such random ordering (see discussion of limitations and future work in Sec. 5).

4. Analysis and Results

The data selection, extraction, aggregation, and plotting was mostly conducted using version 4.2.2 of a programming language for numerical and matrix computations and using a corresponding statistics package [44, 45]. The following sections detail the methods utilized to extract and aggregate the OTS marker data, the data captured for the two coordinate registration methods and spiral search localization (logged from the manipulator controller and control program), and the cart transporter pose obtained from the cart transporter controller. An analysis of the cart base and EOAT uncertainty is then provided. The speed and accuracy of the two coordinate registration methods are compared based on the logged data. Finally, the digital level readings are compared between each side of the RMMA.

4.1 Data Selection and Calibration

Before proceeding with the data analysis, the methods used to pre-process and extract the collected data are described. First, a description is provided regarding how the appropriate OTS marker frames from the paused time intervals were extracted. Then, the process used to calibrate a coordinate transformation from the coordinate systems of the data that origi-

nated from the robot logs to the OTS coordinate system is described. This process included finding a suitable coordinate transformation matrix for the manipulator base coordinates to the OTS coordinate system and for the cart transporter map coordinate system to the OTS coordinate system.

4.1.1 Selecting OTS Marker Data

The extraction and aggregation of the static, ground-truth RMMA measurements was straightforward. For each trial, the centroid and marker position data was averaged over all non-occluded frames. The average and standard deviation of the static RMMA marker data were then exported to external CSV files and plotted. Boxplots for the standard deviations of the static marker data associated with the RMMA ground truth measurements are shown in Fig. 13. The plot includes all five trials of static measurements. From the plot, it was observed that the standard deviation of the marker positional components were well below the 0.26 mm dynamic measurement uncertainty [15, 16]. Overall, the central tendency of the x and z component-wise standard deviations also were below the 0.022 mm static measurement uncertainty [15, 16]. However, several markers across several trials were observed to exceed the static measurement uncertainty in the y component (i.e., the height component). No potential outliers or outlier values were present in the boxplots.

As previously described, the OTS marker data were captured and exported across two separate, continuous files per trial (one for the edge registration and one for the bisect registration) recorded at 120 FPS. With the EOAT assumed to be paused for 15 seconds over the final, detected edge registration reference points ($\vec{r}_1$, $\vec{r}_2$, $\vec{r}_3$), bisect ($\vec{lr}_1$, $\vec{lr}_2$, $\vec{lr}_3$, and $\vec{lr}_4$) points, and spiral search ($\vec{ap}_1$, $\vec{ap}_2$, $\vec{ap}_3$, and $\vec{ap}_4$) points, the first task was to detect when the EOAT was paused.

In contrast to the data selection methods used in prior experiments with the mobile robot [6], which detected pauses by examining the standard deviation in the x and y components of the EOAT markers across a 5s (600 frame) contiguous, sliding window of data, a different data selection method was used for this experiment. Instead, the average rate of change (ARC) of the EOAT was computed using the x, y, and z components of the EOAT rigid body centroid (see Fig. 8) was computed on approximately 1 second intervals. If $\vec{f}_1 = (\vec{f}_1.x, \vec{f}_1.y, \vec{f}_1.z)$ and $\vec{f}_2 = (\vec{f}_2.x, \vec{f}_2.y, \vec{f}_2.z)$ are the position vectors of the EOAT rigid body centroid at corresponding successive times s_1 and s_2, respectively, then the formula used to compute the ARC (i.e., the approximate speed of the marker) over the interval is given by: $\frac{||\vec{f}_2 - \vec{f}_1||_2}{|s_2 - s_1|}$.

The time at which the robot was paused was determined by detecting when the approximate speed of the marker fell below a threshold value for a specified time interval. The exact speed threshold value and time duration used was adjusted depending on which pause was being detected and which registration method was being used. For example, for the first pause of the edge registration method, the speed threshold was 0.5 mm/s. The corresponding time duration was adjusted to either 10 seconds, 15 seconds, or 13 seconds for different trials. This was done to ensure that the initial pause was not detected before

Fig. 13. Boxplots of the standard deviation marker position components for static ground truth RMMA measurements ('+' - Potential Outlier, 'O' - Outlier).

the actuated feet on the cart had finished lowering. For all other pauses of the edge registration, the speed threshold was set to 0.3 mm/s over a time duration of 5 seconds. For the bisect method, the speed threshold was set to 0.5 mm/s for the pauses occurring after the detection of the $\vec{lr}$ points, and the speed threshold was instead set to 0.2 mm/s for the pauses corresponding to the detection of the $\vec{lr}$ points. This was done to ensure that the small movements of the manipulator arm performed as part of the bisect coordinate registration method were not detected as a pause. The time interval was also kept to 5 seconds for all bisect pauses. The end of the 15 second pause was determined by detecting when the approximate speed of the marker exceeded another threshold value of 5 mm/s over a time duration of 1 second. After finding the frames that bound the 15 second pause interval, the average and standard deviation position for 600 data frames (5 seconds) within the 15 second pause interval was computed for all rigid body and the individual markers (including the cart base, EOAT, and RMMA during the experiment) and saved to a separate CSV file for plotting. Additionally, the average rigid body quaternion orientation was approximated by taking the component-wise average of the quaternion vectors and normalizing the result. If a frame was missing or occluded, then an additional frame at the end of the 5

second interval was included.

Figures 14 - 16 show boxplots of the aforementioned marker standard deviations across all pauses and all trials for the rigid body data captured during the edge coordinate registration and subsequent verification. From Fig. 14 and Fig. 16, it was observed that the cart and RMMA component-wise standard deviations all fell below the 0.26 mm dynamic measurement uncertainty of the OTS [15, 16]. In Fig. 14, a single outlier was present for each marker that exhibited more variation than the other values. However, the outlier values still fell below the dynamic measurement uncertainty. Despite this, most of the component-wise standard deviations for the EOAT also fell below the 0.26 mm dynamic measurement uncertainty, with the exception of the z component for one pause captured for markers M3 and M5 on the EOAT[3]. Note that this value occurred when measuring the EOAT on the "RMMASq3" side of the RMMA. By comparing the timestamp and pause number of the instance where the higher standard deviation occurred to the corresponding OTS take file, the EOAT was verified to be paused over the $\vec{a}p_3$ target during the time interval returned by the data extraction code. Since only markers M3 and M5 were affected and the EOAT was verified to be paused, the issue can likely be attributed to a slight occlusion of the markers. This should not have significantly impacted the OTS positional measurement of the RLS since markers M1 and M2 were primarily used to determine the x and z position of the RLS and the component-wise standard deviation of these markers fell below the 0.26 mm dynamic uncertainty even when the outlier values were considered. Generally, the central tendency of the x and z component-wise standard deviations were close to the 0.022 mm static measurement uncertainty. However, as opposed to the static RMMA marker measurements, the boxplots for the EOAT (Fig. 15) exhibited a higher presence of outlier values than those of the other rigid bodies.

Figures 17 - 19 show boxplots of the marker standard deviations across all pauses and all trials for the rigid body data captured during the bisect coordinate registration method and subsequent verification. From Fig. 17 and Fig. 19, it was once again observed that the component-wise standard deviations for the cart and RMMA markers fell below the 0.26 mm dynamic measurement uncertainty of the OTS [16]. The component-wise standard deviation for markers M3 and M5 of the EOAT rigid body again exceeded this measurement uncertainty with the largest outlier seen for the z component of marker M5. Unlike the edge method, the component-wise standard deviations of the EOAT when using the bisect method exceeded the dynamic measurement uncertainty for multiple pauses. The largest of these standard deviations occurred when the EOAT was paused over $\vec{a}p_4$ [4]. Once again, the EOAT was confirmed to have been paused over $\vec{a}p4$ during the time interval returned by the data extraction code. The large standard deviations always seemed to occur on the "RMMASq3" side of the RMMA and always when detecting the same target ($\vec{a}p_3$ for the edge registration and $\vec{a}p_4$ for the bisect registration method). Therefore, the high variation was once again likely due to either marker occlusion or slight manipulator vibration. For example, another high standard deviation for the paused EOAT was observed on markers

[3]Measured for the $\vec{a}p_3$ pause for the trial that started at 02:14:51 PM.

[4]Observed during the trial that started at 02:44:04 PM.

M3 and M5 over $\vec{ap}_4$ for two separate trials [5]. In the latter case, it was manually verified that the EOAT was indeed paused over the $\vec{ap}_4$ reflector by comparing the outputted pause interval time with the corresponding time stamp in the take file. Finally, it should be noted that the EOAT rigid body again displayed more outlier values than the other rigid bodies for the bisect registration method. However, since the standard deviations of markers M1 and M2 on the EOAT again fell below the dynamic measurement uncertainty of the OTS, the analysis using the OTS should not have been significantly impacted by the positional uncertainty.

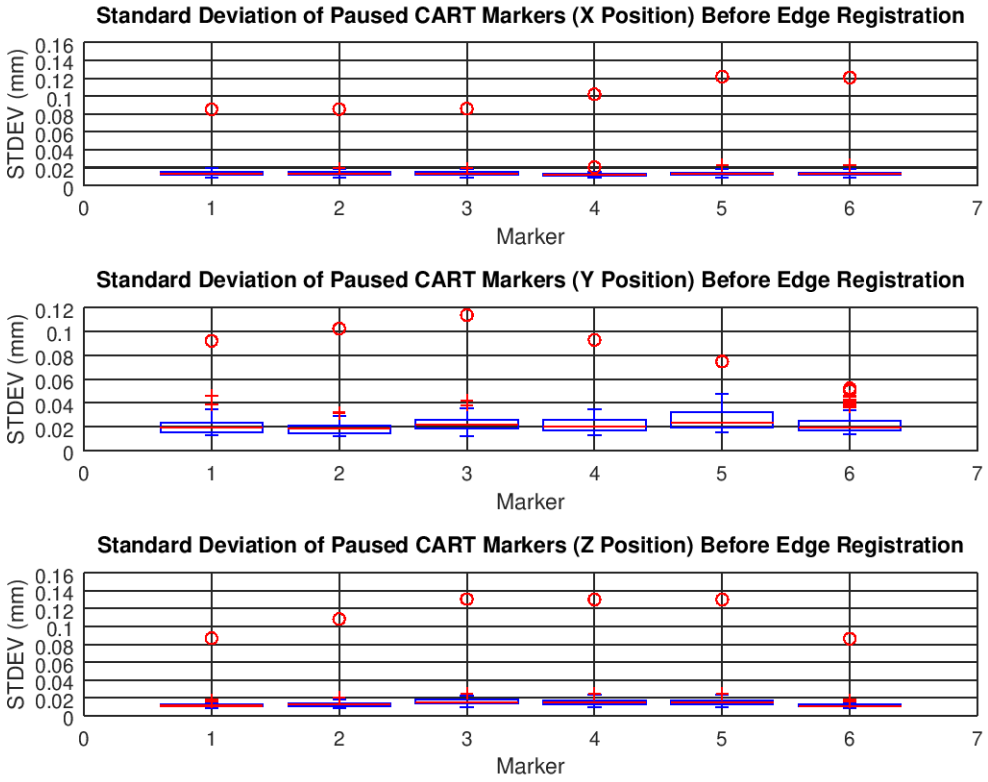

Fig. 14. Boxplots of the standard deviation marker position components for cart base before each edge registration ('+' - Potential Outlier, 'O' - Outlier).

[5]Observed during the trials that started at 02:17:39 PM and 02:57:38 PM.

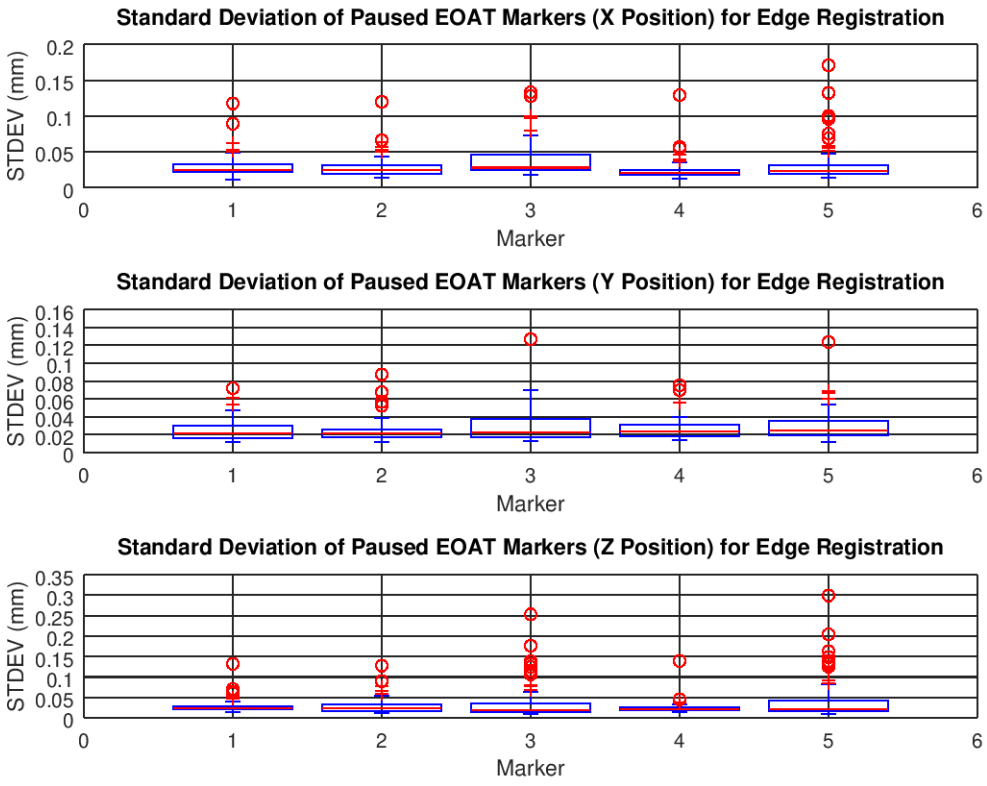

Fig. 15. Boxplots of the standard deviation marker position components for EOAT during each edge registration ('+' - Potential Outlier, 'O' - Outlier).

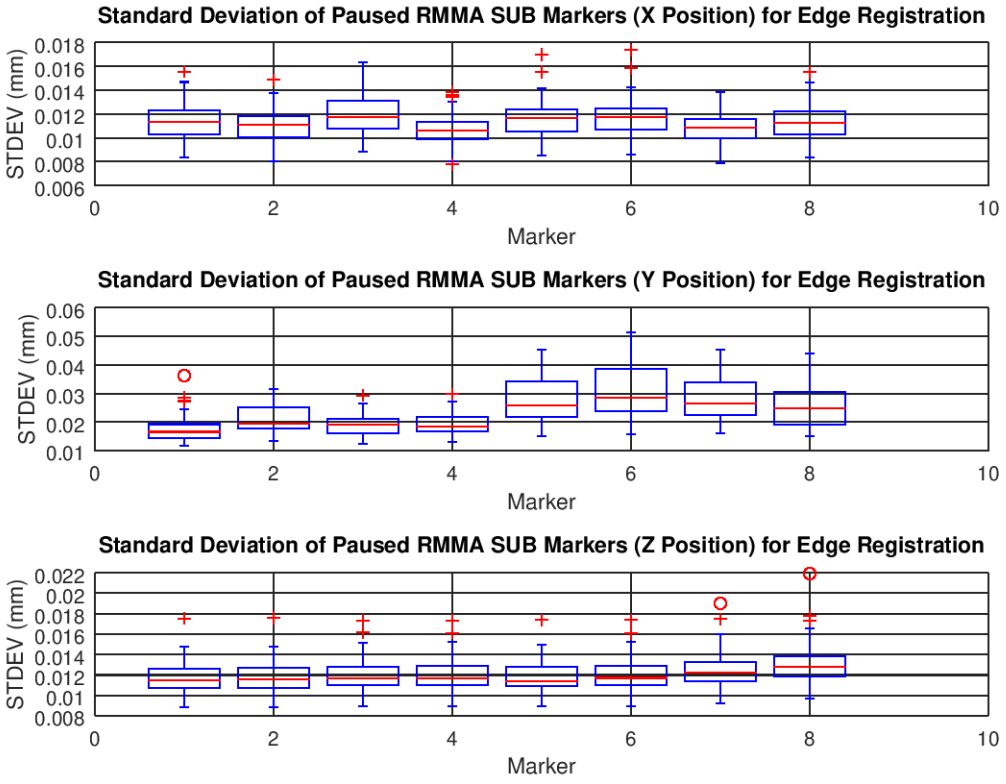

Fig. 16. Boxplots of the standard deviation marker position components for RMMA during edge registration ('+' - Potential Outlier, 'O' - Outlier).

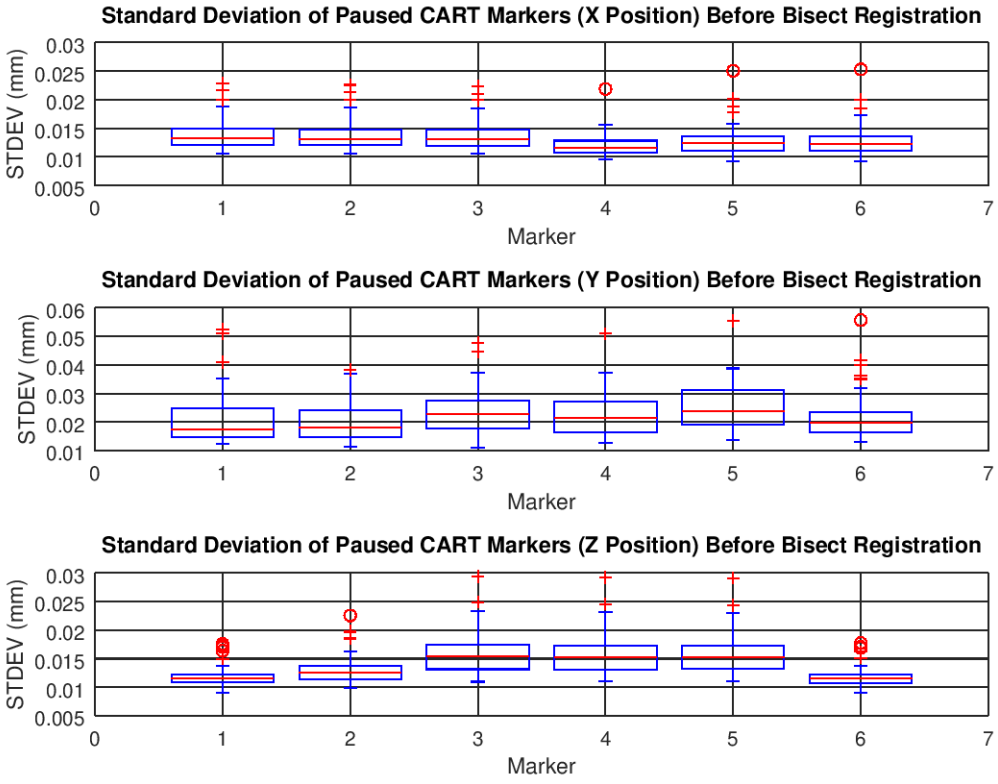

Fig. 17. Boxplots of the standard deviation marker position components for the cart base before each bisect registration ('+' - Potential Outlier, 'O' - Outlier).

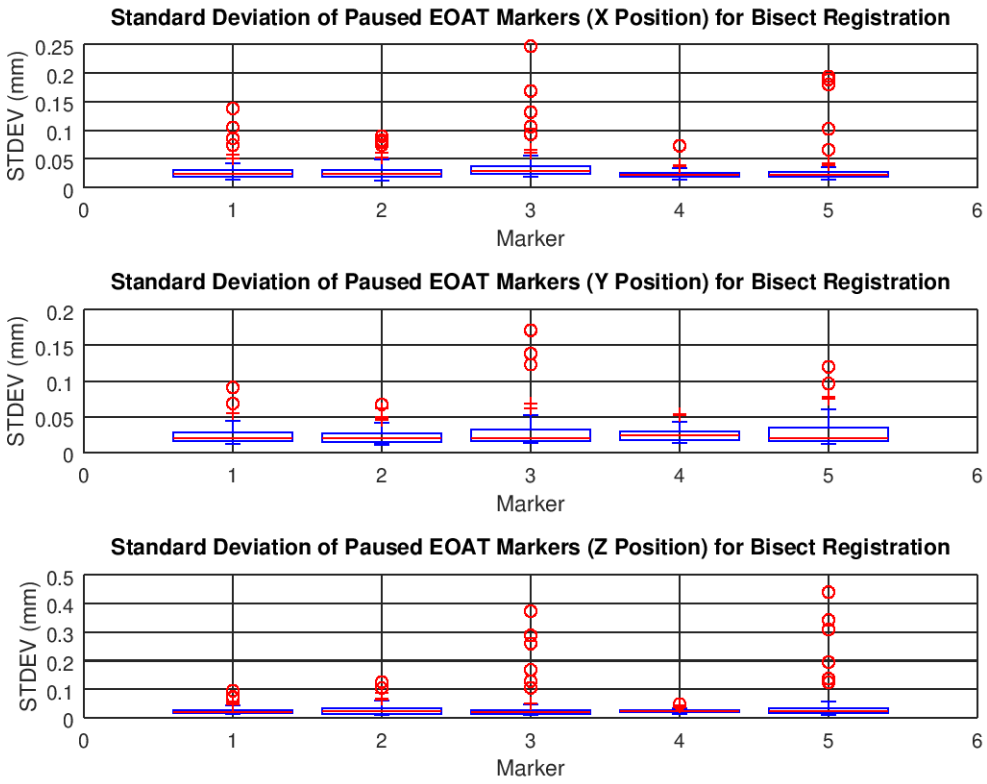

Fig. 18. Boxplots of the standard deviation of marker position components for the EOAT during each bisect registration. (’+’ - Potential Outlier, ’O’ - Outlier)

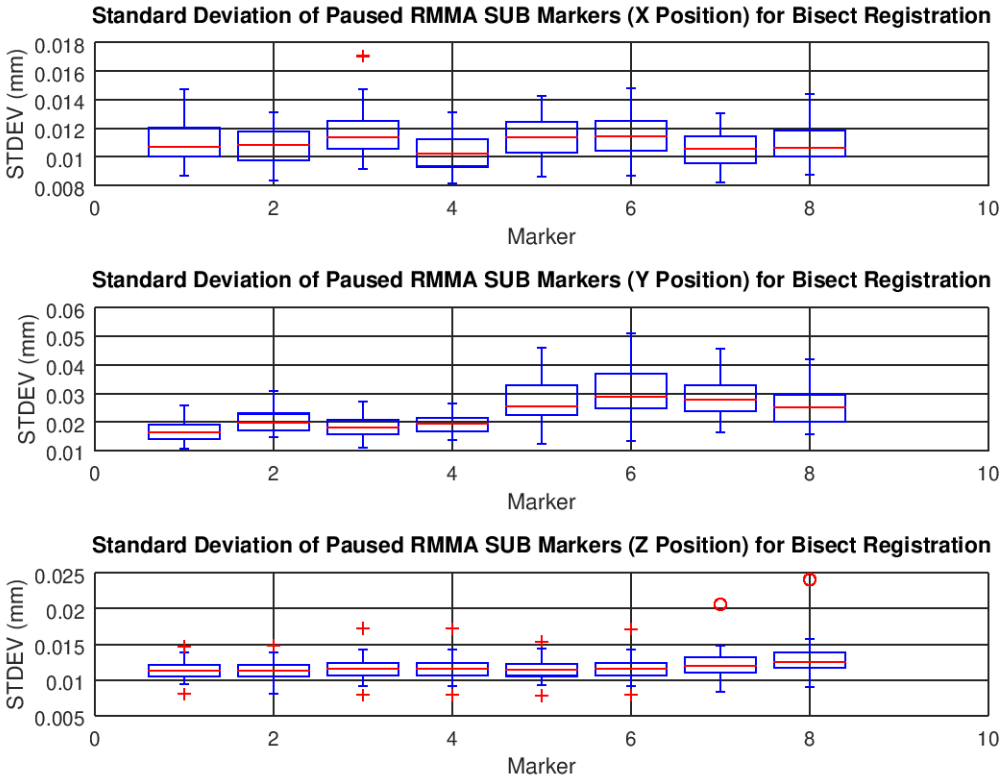

Fig. 19. Boxplots of the standard deviation of marker position components for the RMMA during bisect registration. ('+' - Potential Outlier, 'O' - Outlier)

For the position measurement of each pause, the centroid of the cart base rigid body (Fig. 7) as calculated by the OTS was used. The heading of the cart was determined by computing the angle between the vector denoted by M6 and M5 on the cart (see Fig. 7) and the vector denoted by markers M11 and M9 on the RMMA (see Fig. 9). Additionally, the EOAT rigid body position over each registration point ($\vec{r}_1$, $\vec{r}_2$, and $\vec{r}_3$ for the edge registration, $\vec{lr}_1$, $\vec{lr}_2$, $\vec{lr}_3$, and $\vec{lr}_4$ for the bisect registration, and $\vec{ap}_1$, $\vec{ap}_2$, $\vec{ap}_3$, and $\vec{ap}_4$ for the spiral search localization) was determined by computing the midpoint of markers M1 and M2 (see Fig. 8). The RMMA corner point of the edge registration in the OTS ground truth reference for each trial was computed by solving Eq. 1 - Eq. 2 and substituting the OTS-measured registration points ($\vec{r}_1$, $\vec{r}_2$, and $\vec{r}_3$) for the given trial.

4.1.2 Calibration of EOAT Logged Pose to OTS Coordinate System

For this problem, it was assumed that the OTS markers, M1 and M2 in Fig. 8, tracked approximately the same point that was recorded from the manipulator controller since the OTS markers are placed directly on the EOAT. It was also initially assumed, as in prior experiments, that the position of the EOAT relative to the RMMA ground truth measurements could be projected into 2D due to approximately level flooring [6]. This assumption will be further examined in Sec. 4.5 to inform calibration improvements for future experiments.

Given these assumptions, the calibration problem is now outlined. For each of the 11 trials, indexed by integer subscript i, the manipulator detected a total of nine registration points. Therefore, for the purpose of this discussion, let each registration point be relabeled as $\vec{r}_j$ where j is an integer subscript denoting the registration point. Therefore, $\vec{r}_1$, $\vec{r}_2$, and $\vec{r}_3$ still correspond to the edge registration points $\vec{r}_1$, $\vec{r}_2$, and $\vec{r}_3$ (as defined before in Sec. 3.1.1 and shown in Fig. 10). However, $\vec{r}_4$ now corresponds to either $\vec{ap}_1$ or $\vec{ap}_3$ and $\vec{r}_5$ now corresponds to either $\vec{ap}_2$ or $\vec{ap}_4$ for the spiral search localization after performing edge registration. $\vec{r}_6$ now corresponds to either $\vec{lr}_1$ or $\vec{lr}_3$ and $\vec{r}_7$ now corresponds to either $\vec{lr}_2$ or $\vec{lr}_4$ for the bisect registration. Finally, $\vec{r}_8$ corresponds to either $\vec{ap}_1$ or $\vec{ap}_3$ and $\vec{r}_9$ corresponds to either $\vec{ap}_3$ or $\vec{ap}_4$ for the spiral search localization after performing bisect registration. Let the 2D (i.e., with position components along the x and z axes) position of the EOAT midpoint, when paused over the jth registration point and measured in the OTS coordinate system for the ith trial be stored in vector $\vec{o}_{i,\vec{r}_j} = \begin{pmatrix} z_{i,\vec{r}_j} & x_{i,\vec{r}_j} \end{pmatrix}$. Note that, due to y being the vertical axis in the OTS coordinate system, the x and z components of $\vec{o}_{i,\vec{r}_j}$ were intentionally reversed for the calibration (i.e.,the z axis of the OTS coordinate system corresponded to the x axis of the manipulator coordinate system and the x axis of the OTS coordinate system corresponded with the y axis of the manipulator coordinate system). Furthermore, let vector $\vec{l}_{i,\vec{r}_j} = \begin{pmatrix} x_{i,\vec{r}_j} & y_{i,\vec{r}_j} \end{pmatrix}$ store the corresponding 2D position (i.e., with position components along the x and y axes) of the EOAT midpoint, when paused over the jth registration point and as logged by the manipulator controller (i.e., in the manipulator base coordinate system) for the ith trial. Note that the vectors contain measurements of the same object (i.e., the manipulator EOAT over each registration point) in two different coordinate systems (i.e., the OTS and manipulator base coordinates). The calibration problem

is, for each of the *i* trials, to find a 2x2 rotation matrix, $\boldsymbol{R}_i$, and a 2x1 translation vector, $\vec{\boldsymbol{t}}_{\boldsymbol{i}}$ that optimizes the equation, $min_{\boldsymbol{R}_i,\vec{\boldsymbol{t}}_{\boldsymbol{i}}} \sum_{j=1}^{9} ||\boldsymbol{R}_i \vec{l}_{i,\vec{r}_j} + \vec{\boldsymbol{t}}_{\boldsymbol{i}} - \vec{o}_{i,\vec{r}_j}||$ [46].

An existing, closed-form solution, which was also already adapted into code, was used to solve this problem [47, 48]. It should be noted that, in this solution, $\boldsymbol{R}_{\boldsymbol{i}}$ was assumed to be an orthogonal matrix and the $\boldsymbol{R}_{\boldsymbol{i}}$ matrix returned from this solution might have resulted in a reflection if this assumption was not met [46, 47]. The code included the ability to output a warning if the returned $\boldsymbol{R}_{\boldsymbol{i}}$ was a reflection, however, no warnings occurred when the code was run on the data set [48].

Fig. 20 shows boxplots of the Euclidean distances between the position of the EOAT as measured in the OTS coordinate system and the position of the EOAT as measured by the manipulator controller and transformed to the OTS coordinate system. Note that the corner point for the edge registration as measured by the manipulator controller, though not included in the calibration since it was determined by $\vec{r}_1$, $\vec{r}_2$, and $\vec{r}_3$, is also shown in the OTS coordinate system. From the boxplots, it was observed that the distance between the transformed robot controller coordinates and the corresponding OTS coordinates (which was indicative of the accuracy of the manipulator controller-recorded positions when compared to the OTS ground truth reference) was approximately between 0.025 mm and 2.6 mm. The largest distances were observed when the EOAT was measured on the "RMMASq2" side of the RMMA. The distance between the EOAT positions for the corner point, $\vec{a}p_1$ after the bisect registration (i.e., $\vec{a}p_1.b$), and $\vec{a}p_3$ after the bisect registrations had the largest ranges. It was also noted that no outlier values were observed, though potential outliers were seen for $\vec{r}_3$ on the "RMMASq3" side of the RMMA and $\vec{l}r_2$ on the "RMMASq2" side of the RMMA.

4.1.3 Calibration of Vehicle Logged Pose to OTS Coordinate System

The process used to calibrate the coordinate transformation matrix to express the cart transporter controller pose as a cart centroid position in the OTS coordinate system is now described. It is important to note that the pose computed by the cart transporter was not assumed to have been tracking the same point as the OTS markers placed on the cart base (see Fig. 7) since the cart base was detachable from the cart transporter vehicle, which was thought to possibly introduce alignment variability between the cart and vehicle base. Furthermore, while it was assumed the cart transporter vehicle map origin was located at the centroid of the cart transporter vehicle base upon map creation, this point was not accessible for measurement and meant that prior knowledge of the cart transporter map coordinate system origin location within the lab space was unavailable. Therefore, two unknown coordinate transformations needed to be calibrated: one that transformed the cart transporter vehicle pose to the OTS coordinate system, denoted ${}^{\{OTS\}}\boldsymbol{H}_{\{MAP\}}$, and one that transformed between the cart transporter vehicle pose and the cart base, denoted ${}^{\{cartproj\}}\boldsymbol{H}_{\{transv\}}$.

To formalize the description of the calibration problem, the following is noted. Let ${}^{\{MAP.transv\}}\vec{v}_i = \begin{pmatrix} x_i & y_i & \theta_i \end{pmatrix}$ be a vector containing the 3DoF pose of the cart transporter in the vehicle map coordinate system for the *i*th trial as obtained from the cart transporter

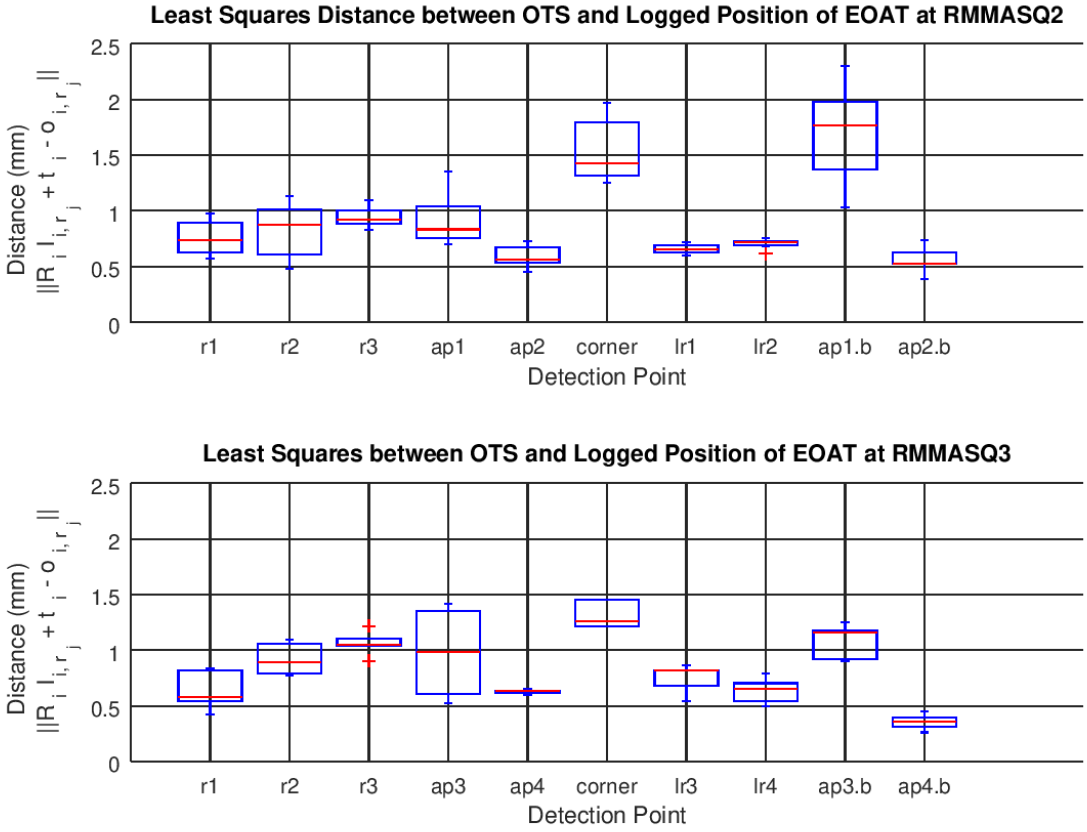

Fig. 20. Boxplots of the least squares distance between the EOAT positions as recorded by the OTS and the calibrated position data from the manipulator controller ('+' - Potential Outlier, 'O' - Outlier). The $\vec{ap}$ points labeled with a "b" indicate the points were localized after performing the bisect registration method.

controller. Therefore, the matrix

$$ {}^{\{MAP\}}H_{i\{transv\}} = \begin{pmatrix} cos(\theta_i) & -sin(\theta_i) & x_i \\ sin(\theta_i) & cos(\theta_i) & y_i \\ 0 & 0 & 1 \end{pmatrix} $$

stores the same corresponding 3DoF pose as represented by a homogeneous transformation matrix. Furthermore, let ${}^{\{OTS.cart\}}\vec{c}_i = \begin{pmatrix} q_{X,i} & q_{Y,i} & q_{Z,i} & q_{W,i} & x_i & y_i & z_i \end{pmatrix}$ be a vector that stores a 6DoF pose consisting of a quaternion rotation (i.e., with rotation components q_x, q_y, q_z, and q_w as defined in Eq. 16 - 18, Appendix D) and position (i.e., with position components along the x, y and z axes) of the cart base rigid body centroid as measured by the OTS for the ith trial. Recall, as described in Sec. 4.1.1, that the average position of the cart rigid body was obtained by taking an average over 600 frames of OTS data for each

trial. Similarly, the average quaternion rotation of the cart rigid body was approximated for each trial by computing the component-wise mean over 600 OTS frames and then normalizing the resulting quaternion vector. Then, the 6DoF poses of vector ${}^{\{OTS.cart\}}\vec{c}_i$, were projected to 3DoF poses. This was done by discarding the y component (i.e., the height component in the OTS coordinate system) and observing that the axis of rotation in the OTS data varied primarily about the y axis. The latter observation allowed Eq. 19 (see Appendix D) to be solved for the angle of rotation about the y axis. The result was used to form the homogeneous transformation matrix:

$$ {}^{\{OTS\}}H_{i\{cartproj\}} = \begin{pmatrix} cos[2arccos(-1^i(q_{w,i}))] & -sin[2arccos(-1^i(q_{w,i}))] & x_i \\ sin[2arccos(-1^i(q_{w,i}))] & cos[2arccos(-1^i(q_{w,i}))] & z_i \\ 0 & 0 & 1 \end{pmatrix} $$

Note also that the sign of each rotation measurement taken on the "RMMASq2" side of the RMMA was reversed before solving for the needed coordinate transformation to eliminate the reflection between the rotation measurements taken on the "RMMASq3" side of the RMMA. With the data from each coordinate system expressed in this manner, the calibration problem was formulated as:

$$ {}^{\{OTS\}}\boldsymbol{H}_{\{MAP\}}\,{}^{\{MAP\}}H_{i\{transv\}} \approx {}^{\{OTS\}}H_{i\{cartproj\}}\,{}^{\{cartproj\}}\boldsymbol{H}_{\{transv\}} $$

This is a 2D case of the Robot-World/Hand-Eye calibration problem, where again ${}^{\{OTS\}}\boldsymbol{H}_{\{MAP\}}$ is the unknown homogeneous transformation matrix that transforms between the cart transporter vehicle map coordinate system to the OTS coordinate system and ${}^{\{cartproj\}}\boldsymbol{H}_{\{transv\}}$ is the unknown homogeneous transformation matrix that transforms between the cart transporter vehicle and the projected cart base [46, 49, 50].

Two different methods were attempted to solve the calibration problem. The first method, of which the 2D formulation was used, failed to find a unique solution resulting from an under-constrained problem formulation [49]. The second method, which was adapted for 2D coordinate systems, found a unique solution, though the best orthogonal transformation returned a reflection rather than a rotation [50]. This was determined to be due to y being the vertical axis of the OTS coordinate system, which reversed the direction of the x axis between the OTS and cart transporter vehicle map coordinate systems (i.e., when projected into 2D the OTS coordinate system effectively became left-handed instead of right-handed). Therefore, the reflection was adjusted back to a rotation by reversing the sign of the smallest singular value from the Singular Value Decomposition (SVD) used to formulate the solution [51]. Figure 21 plots the results of each calibration. In addition, to provide reference points to verify the calibration, the calibrated points were plotted with example static ground truth RMMA markers [6] (see Fig. 6). Note there was approximately 150 mm difference in the x and z components between each "projected nav vehicle" point

[6] Note that the sample static ground truth markers featured in the plot may differ slightly from the actual static ground-truth RMMA data featured in this report by a few millimeters.

and the corresponding "projected nav cart" point (i.e., the point calibrated using the first method [49]). Additionally, there was approximately 100 mm to 150 mm difference between each "projected nav vehicle partial" point and the corresponding "projected nav cart partial" (i.e., the point calibrated using the second method [50]) point in the x component and approximately 50 mm to 75 mm difference between the same points in the z component. The following factors could contribute to the misalignment between the cart rigid body centroid and the centroid of the cart transporter vehicle base. First, the cart payload structure was not mounted at the direct center of the detachable cart, but at an offset of approximately 76.2 mm towards the front of the cart to allow space to accommodate the cart batteries. Note that this offset can be observed in the center of Fig. 1 and would contribute mostly towards the x component misalignment observed in Fig. 21 depending on the cart rotation about the y axis of the OTS coordinate system. Furthermore, the centroid of the cart rigid body, as defined and measured by the OTS software, was used to determine the docking position of the cart. Due to the additional markers M2 and M4, which were included to avoid symmetric marker placement (see Sec. 2.4 and Fig. 7), the centroid of the OTS rigid body was further offset towards one of the front corners of the cart payload structure. Using the OTS position data from the first trial[7], the offset between the cart rigid body centroid both with and without markers M2 and M4 was computed and revealed an offset of about 29.127 mm in the x component and 33.751 mm in the z component. In total, this result potentially accounts for an approximate misalignment of 105.327 mm in the x component and 33.751 mm in the z component between the cart rigid body centroid and the cart transporter vehicle base centroid. The remainder of this offset could be indicative of further misalignment between the cart transporter vehicle base centroid and the cart rigid body due to unknown sources of uncertainty or could have been influenced by the calibration method used.

Fig. 22 shows boxplots of the Euclidean distances between the position of the cart centroid as measured in the OTS coordinate system and the position of the cart centroid as measured using the vehicle controller pose, which was calibrated and transformed to the cart base centroid in the OTS coordinate system using the second method [50]. The data was divided between the two stops next to the RMMA (i.e., "RMMASq2" and "RMMASq3"). The distances between the OTS cart centroid data and calibrated cart centroid data on the "RMMASq3" side varied between a minimum of approximately 14 mm and a maximum of 62 mm. The corresponding data on the "RMMASq2" side varied between a minimum of approximately 12 mm and a maximum of 41 mm. Since a better fit (between 0.026 mm to 2.6 mm) between the calibrated EOAT positions and the equivalent OTS points was achieved in comparison to the calibrated cart centroid positions, this supported the possibility of higher position error present in the cart transporter vehicle controller's determination of the vehicle pose. Additionally, the "RMMASq3" side displayed a larger range of discrepancy between the cart centroid measured in the OTS coordinate system and the cart centroid calibrated from the cart transporter controller vehicle pose. Also note that no potential outliers or outlier values were observed.

[7]The trial that started at 02:08:04 PM.

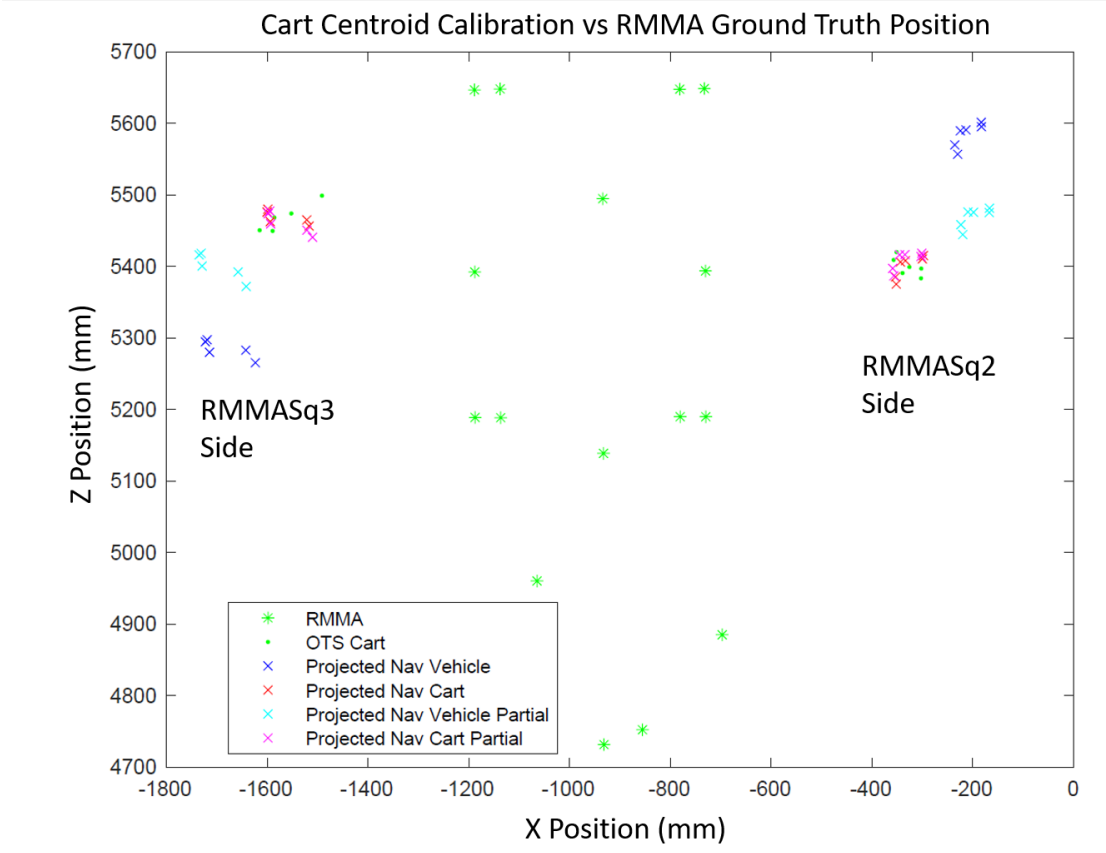

Fig. 21. Plot of the calibrated cart transporter positions (in the OTS coordinate system) next to sample OTS RMMA ground truth markers and cart centroid position as originally measured by the OTS. The "projected nav vehicle" and "projected nav cart" points were calibrated using the first method [49], while the "projected nav vehicle partial" and "projected nav cart partial" points were calibrated using the second method [50]. Also, note that the sample static ground truth markers featured in the plot may differ slightly from the actual static ground-truth RMMA data featured in this report by a few millimeters.

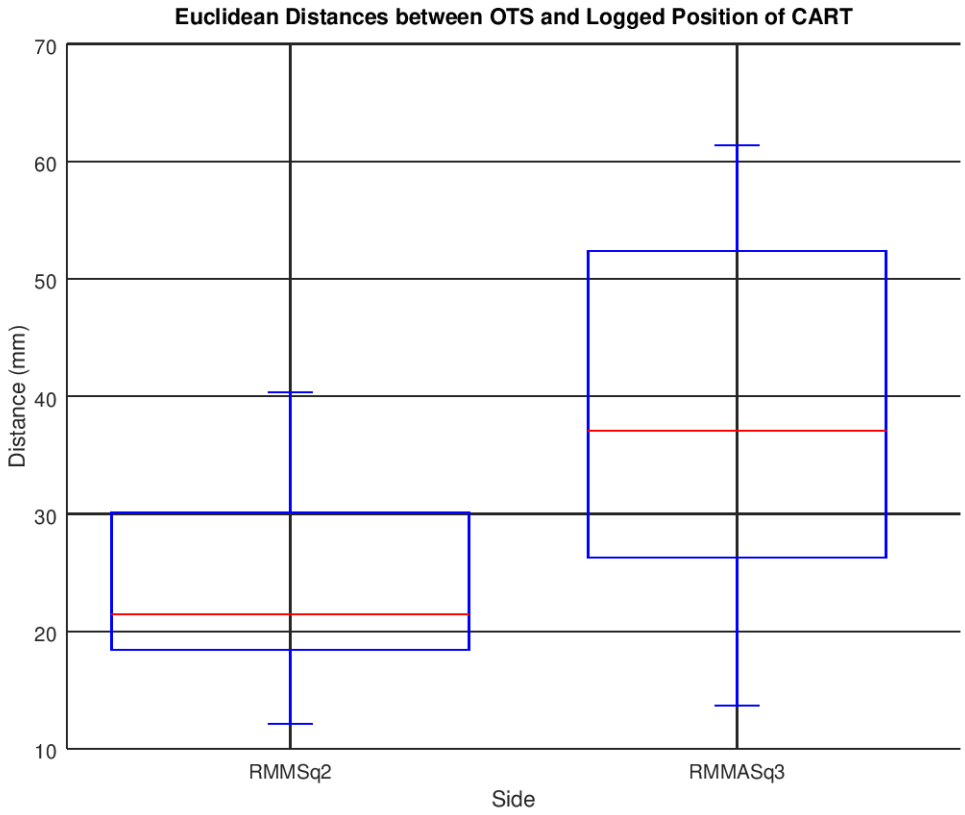

Fig. 22. Boxplots of Least Squares distance between the CART rigid body centroid position data as measured by the OTS and the cart centroid position data calibrated using the second calibration method [50] applied to the data obtained from the cart transporter vehicle controller ('+' - Potential Outlier, 'O' - Outlier).

4.2 Uncertainty Analysis of OTS Measurements

With the background and data extraction techniques detailed, the focus now turns to analyzing the uncertainty of the mobile manipulator-on-a-cart while performing the mock assembly tasks. The analysis primarily focused on position repeatability at different points of the docking and assembly process. In this section, the analysis deals exclusively with the data captured from the OTS.

Figure 23 shows a plot of the cart position after having docked with the RMMA and the EOAT position when the EOAT was paused over the final detection point of each coordinate registration and spiral search localization. Linear regression fits were computed for the colinear points of each coordinate registration method (i.e., a fit for the corner points and $\vec{r}_3$ points on both sides of the RMMA, a fit for the $\vec{lr}_1$ and $\vec{lr}_3$ points, and a fit for the $\vec{lr}_2$ and $\vec{lr}_4$ points) and spiral search localization (i.e., a fit for the $\vec{ap}_1$ and $\vec{ap}_3$ points and a fit for the $\vec{ap}_2$ and $\vec{ap}_4$ points performed after both the edge and bisect coordinate registration methods).

The $\mathcal{R}^2$ values for each of the horizontally-fitted lines were all almost 1. For comparison, straight line segments through the ground truth static measurement of the same points (i.e., a line for the $\vec{lr}_1$ and $\vec{lr}_3$ points, a line for the $\vec{lr}_2$ and $\vec{lr}_4$ points, a line for the $\vec{ap}_1$ and $\vec{ap}_3$ points, and a line for the $\vec{ap}_2$ and $\vec{ap}_4$ points) were also included. It should be noted that the fits for the EOAT detection points exhibited a non-zero slope that was approximately 0.38 for the lines horizontally fitted to the detected $\vec{ap}$ points and about 0.27 for the line fitted to the top of the detected edge registration points that included the corners and $\vec{r}_3$ points. However, the line segments for the ground truth reference of the actual static position of the retro-reflective targets exhibited slopes that were almost zero. Since the static ground truth measurement line segments displayed a zero slope but the corresponding fits for the measured EOAT detection points did not, an external factor could have impacted the mobile manipulator-on-a-cart, but not the RMMA. For example, uneven floor leveling could have affected the detection angle of the RLS, but the RMMA could be considered more or less level. This rotation of the EOAT detection points could also be related to another notable observation, which was the misalignment between the EOAT detection points and the ground truth measurements. This observation will be discussed in further detail later in this section.

Table 3 shows the average and standard deviation of the final EOAT position for each coordinate registration detection point taken over all 11 trials, as measured by the OTS. The average and standard deviations in this table correspond to the EOAT detection points shown in Fig. 23. From the table, the following observations were noted. First, the variability of the EOAT position seemed to be higher overall on the "RMMASq3" side when compared to the "RMMASq2" side of the RMMA for both registration methods. A large standard deviation for the z component of $\vec{r}_1$ and $\vec{r}_2$ was also observed. This could be explained by the following. As noted in Sect. 2.1, the vehicle docked with the table by first traveling to a goal point 1000 mm in front of the RMMA. If the vehicle docked at the goal point with slight uncertainty in its heading, the error could have propagated in the z (y in the cart transporter vehicle map coordinate system) direction. However, if $\vec{r}_1$ and

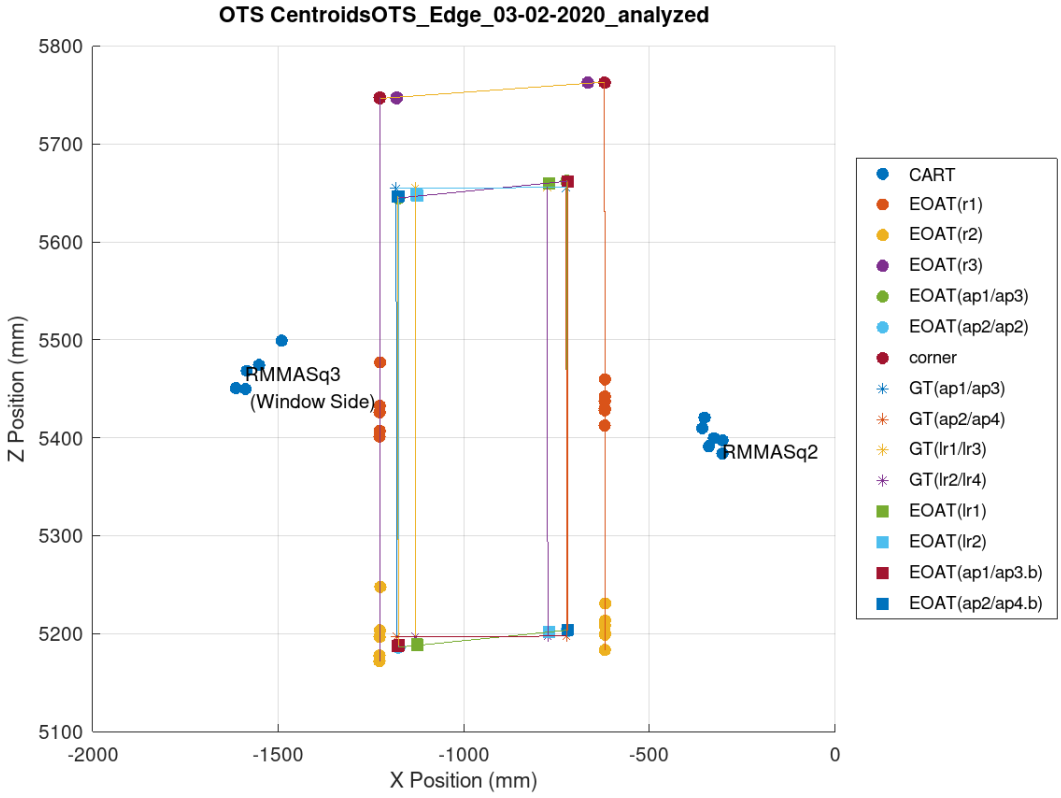

Fig. 23. Plot of the final cart position and EOAT position when paused over the detected registration points as measured by the OTS. The ground truth static measurements of the $\vec{ap}$ reflector positions were included for reference and the plot included a linear regression fit for each set of colinear EOAT detection points for each side of the RMMA.

$\vec{r}_2$ were ignored, the variability of the EOAT positioning was no more than 1 mm on the "RMMASq2" side of the RMMA and no more than 2 mm on the "RMMASq3" side of the RMMA.

Table 4 shows the average and standard deviation of the final cart centroid position and heading, after docking next to the RMMA, taken over all 11 trials, as measured by the OTS. Note that the circular mean and circular standard deviation cart heading are also reported in the table using the respective formulas found in Ref. [52]. From the table, a higher position variability of the final cart docking position in comparison with the EOAT positioning over the retro-reflective targets was observed. The standard deviation of the cart position (and heading) again seemed higher on the "RMMASq2" side of the RMMA when compared with the "RMMASq3" side of the RMMA. Note also that the standard deviation of the heading was between 0.75° and 2°. This further supported the speculation from earlier in this section that the uncertainty in the vehicle heading, combined with the 1000 mm straight move (as described in Sec. 2.1), resulted in the observed variability in the z component of

Table 3. Average and standard deviation final EOAT position for each coordinate registration detection point taken over all 11 trials (as measured by the OTS).

	Mean [Stdev] Position in mm			
	RMMASq2		RMMASq3	
	x	z	x	z
Edge Registration				
EOAT($\vec{r}_1$)	-620.224 [0.315]	5434.919 [15.818]	-1226.551 [0.575]	5428.739 [29.916]
EOAT($\vec{r}_2$)	-619.696 [0.414]	5205.731 [15.959]	-1226.624 [1.103]	5199.347 [30.005]
EOAT($\vec{r}_3$)	-666.139 [0.623]	5762.595 [0.129]	-1180.99 [0.652]	5747.056 [0.383]
EOAT($\vec{ap}_1/\vec{ap}_3$)	-722.611 [0.739]	5661.916 [0.383]	-1175.716 [0.837]	5644.845 [0.485]
EOAT($\vec{ap}_2/\vec{ap}_4$)	-721.328 [0.647]	5203.44 [0.445]	-1176.206 [1.713]	5186.01 [0.237]
$\vec{corner}$	-620.977 [0.507]	5762.699 [0.134]	-1226.393 [0.51]	5747.071 [0.492]
Bisect Registration				
EOAT($\vec{lr}_1/\vec{lr}_3$)	-770.494 [0.425]	5659.999 [0.369]	-1125.84 [1.11]	5188.685 [0.479]
EOAT($\vec{lr}_2/\vec{lr}_4$)	-770.837 [0.533]	5201.668 [0.156]	-1126.692 [1.253]	5647.724 [0.374]
EOAT($\vec{ap}_1/\vec{ap}_3.b$)	-719.956 [0.623]	5661.757 [0.237]	-1176.805 [1.147]	5187.82 [0.343]
EOAT($\vec{ap}_2/\vec{ap}_4.b$)	-721.087 [0.371]	5203.461 [0.427]	-1177.345 [0.928]	5646.548 [0.443]

the EOAT positioning at $\vec{r}_1$ and $\vec{r}_2$.

Fig. 24 shows boxplots of the 2D Euclidean distance between the final EOAT position (as measured by the OTS) when over the $\vec{ap}$ points and the ground truth static measurement of the $\vec{ap}$ points. From the plots, it was observed that the distance between the EOAT position over the $\vec{ap}$ reflectors and the ground truth-measured position of the $\vec{ap}$ reflectors was between 5 mm and 14 mm. A larger discrepancy of about 8 to 14 mm distance between the measured EOAT position and ground truth static measurements of the retro-reflective $\vec{ap}$ targets on the "RMMASq3" side was observed when compared with the "RMMASq2" side of the RMMA, which exhibited a distance between 5 mm and 8 mm between the detected and ground truth-measured points. Only one potential outlier and one outlier were observed in the distance between $\vec{ap}_1.b$ after performing the bisect registration method on the "RMMASq2" side of the RMMA. Additionally, one potential outlier was observed for the distance between $\vec{ap}_3.b$ and one outlier was observed for the distance between $\vec{ap}_4$ on the "RMMASq3" side of the RMMA. The "RMMASq3" side seemed to exhibit slightly

Table 4. Mean and standard deviation final cart centroid position and heading after docking next to the RMMA taken over all 11 trials (as measured by the OTS). Note that the circular mean and circular standard deviation cart heading are also reported (see Ref. [52]).

	Mean [Stdev] Position in mm	
	RMMASq2	RMMASq3
Cart (x)	-330.218 mm [23.56 mm]	-1566.088 mm [47.529 mm]
Cart (z)	5400.375 mm [13.164 mm]	5468.406 mm [20.247 mm]
	Mean [Stdev] Heading	
Cart (θ)	91.611° [0.795°]	88.631° [1.967°]
	Circular Mean [Circular Stdev] Heading	
Cart (θ)	91.611° [0.013]	88.631° [0.605]

more variability when compared to the "RMMASq2" side of the RMMA, and the distance between the detected and ground truth and $\vec{ap}.b$ points was consistently lower than the respective $\vec{ap}$ points on the "RMMASq3" side of the RMMA. No consistent trends were observed, however, when comparing between the $\vec{ap}$ points that were found after edge registration vs. those that were found after performing bisect registration on the "RMMASq2" side of the RMMA.

4.3 Uncertainty Analysis of Controller Log Measurements

Focus now turns to analyzing the uncertainty of the mobile manipulator-on-a-cart using the data collected from the manipulator controller log and the cart transporter vehicle log (after transforming the position and orientation data to the OTS coordinate system). Figure 25 presents the corresponding final cart position and EOAT position when paused over the detected registration points as measured by the robot controller logs. Note that the EOAT points in Fig. 25 were visually indistinguishable from the EOAT points plotted in Fig. 23, though a larger difference existed in the corresponding cart docking positions. These observations were supported by the previously-discussed results of Fig. 20 and Fig. 22. Figure 25, like Fig. 23 also included linear regression fits for the colinear points of each coordinate registration method and spiral search localization. The corresponding $\mathcal{R}^2$ value for each horizontal fitted lines were also almost 1 and the slopes of the horizontal fitted lines also displayed a non-zero slope, as was the case with the fitted lines of Fig. 23.

Table 5 shows the average and standard deviation of the final EOAT centroid position, after docking next to the RMMA, taken over all 11 trials, as measured by the manipulator controller logs. The first observation was the overall similarity of the standard deviation data to that measured by the OTS in Table 3. Once again, the variability of the EOAT position seemed to be higher overall on the "RMMASq3" side when compared to the "RMMASq2" side of the RMMA for both registration methods. A higher standard deviation for the z component of $\vec{r}_1$ and $\vec{r}_2$ was again observed. Excluding these values, the standard deviation of the EOAT position (as measured by the manipulator controller) was again no more than 1 mm on the "RMMASq2" side of the RMMA and no more than 2 mm on the

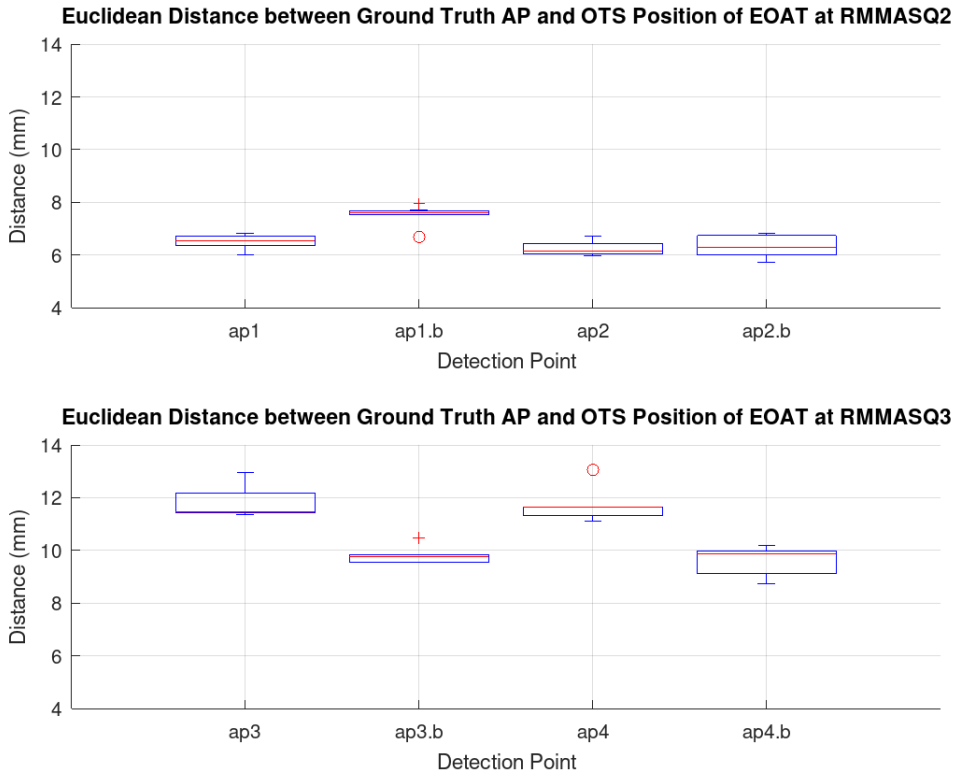

Fig. 24. Boxplots showing the 2D Euclidean distance between the final EOAT position (as measured by the OTS) when over the $\vec{ap}$ points and the ground truth static measurement of the $\vec{ap}$ points ('+' - Potential Outlier, 'O' - Outlier).

"RMMASq3" side of the RMMA, much like the EOAT position measured by the OTS in Table 3.

Table 6 shows the average and standard deviation of the final cart centroid position and heading, after docking next to the RMMA, taken over all 11 trials, and as measured by the cart transporter controller log (in the OTS coordinate system). Overall, the standard deviation cart position data measured by the cart transporter contoller log exhibited similar trends to those observed in Table 4. Once again, the standard deviation of the cart docking position (and heading) showed higher variability when compared to the EOAT positioning over the registration points (Table 5). Additionally, the difference between the mean (and circular mean) cart heading as measured by the OTS and the average cart heading as measured by the cart transporter controller log was only 0.189° on the "RMMASq2" side of the RMMA and 0.351° on the "RMMASq3" side of the RMMA. There was also only a difference of 0.001 and zero between the circular standard deviation cart heading as measured by the OTS and the circular standard deviation cart heading as measured by the cart transporter log on the "RMMASq2" side of the RMMA and the "RMMASq3" side of the

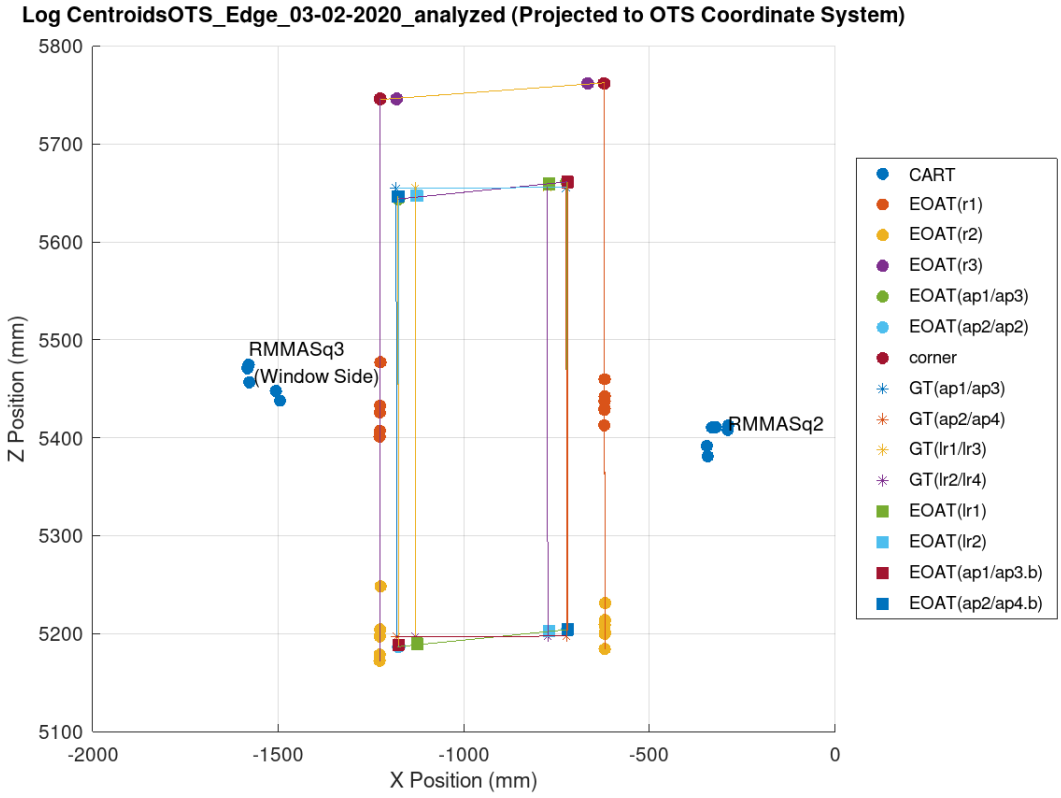

Fig. 25. Plot of the final cart position and EOAT position when paused over the detected registration points as measured by the robot controller logs (and transformed to the OTS coordinate system for more direct comparison). The ground truth static measurements of the $\vec{ap}$ reflector positions were included for reference and the plot included a linear regression fit for each set of colinear detection points for each side of the RMMA.

RMMA, respectively. The corresponding differences in the standard deviation of the cart heading was 0.026° and 0.016°. This indicated that the cart transporter controller perception of the vehicle heading and the vehicle heading variability was similar to that measured by ground truth. As a result, future experiments may attempt to improve the cart transporter docking process with the RMMA by attempting to adjust for heading errors observed by the vehicle controller after reaching the goal, but before executing the 1000 mm straight move command. Note that the cart transporter controller heading was adjusted by adding 90°. Additionally, one trial on the "RMMASq3" side of the RMMA was measured as a positive angle by the cart transporter controller while the other trials measured on that side of the RMMA were measured as negative angles. Therefore, the sign of this observation was also adjusted by subtracting 360°. These adjustments were made so that the cart transporter controller log heading could be compared with the equivalent heading measured and extracted from the OTS data.

Table 5. Average and standard deviation final EOAT position for each coordinate registration detection point taken over all 11 trials (as measured by the manipulator controller log).

	Mean [Stdev] Position in mm			
	RMMASq2		RMMASq3	
	x	z	x	z
Edge Registration				
EOAT($\vec{r}_1$)	-620.955 [0.42]	5435.105 [15.759]	-1225.916 [0.739]	5428.77 [29.959]
EOAT($\vec{r}_2$)	-620.004 [0.426]	5206.491 [15.72]	-1226.067 [1.137]	5200.068 [29.901]
EOAT($\vec{r}_3$)	-666.536 [0.801]	5761.772 [0.135]	-1181.042 [0.673]	5746.001 [0.3]
EOAT($\vec{ap}_1$/$\vec{ap}_3$)	-723.232 [0.71]	5661.265 [0.368]	-1175.768 [0.786]	5643.871 [0.219]
EOAT($\vec{ap}_2$/$\vec{ap}_4$)	-721.29 [0.635]	5204.027 [0.375]	-1176.091 [1.671]	5186.62 [0.224]
$\vec{corner}$	-622.315 [0.777]	5761.956 [0.163]	-1225.66 [0.518]	5746.031 [0.385]
Bisect Registration				
EOAT($\vec{lr}_1$/$\vec{lr}_3$)	-770.477 [0.519]	5659.372 [0.329]	-1126.032 [1.135]	5189.4 [0.513]
EOAT($\vec{lr}_2$/$\vec{lr}_4$)	-770.487 [0.492]	5202.274 [0.17]	-1127.043 [1.183]	5647.195 [0.329]
EOAT($\vec{ap}_1$/$\vec{ap}_3.b$)	-721.038 [0.423]	5661.163 [0.221]	-1176.436 [0.843]	5188.604 [0.332]
EOAT($\vec{ap}_2$/$\vec{ap}_4.b$)	-721.009 [0.381]	5204.015 [0.414]	-1177.284 [1.04]	5646.245 [0.467]

Finally, the boxplots of Fig. 26 are examined, which shows the 2D Euclidean distance between the final EOAT position (as measured by the robot controller log) when over the $\vec{ap}$ points and the ground truth static measurement of the $\vec{ap}$ points. Similar to Fig. 24, it was observed that the distance between the EOAT over the $\vec{ap}$ points and the ground truth static measurements appeared to be higher overall on the "RMMASq3" side when compared with the "RMMASq2" side of the RMMA. Additionally, only one potential outlier was observed on the "RMMASq2" side of the RMMA. However, on the "RMMASq3" side of the RMMA, two potential outliers occurred for the $a\vec{p}_3$ distances and one potential outlier occurred for the $a\vec{p}_3$ distances. Again, the "RMMASq3" side seemed to exhibit slightly more variability when compared to the "RMMASq2" side of the RMMA. Generally, the distance between the EOAT position over the $\vec{ap}$ reflectors and the static ground truth-measured position of the $\vec{ap}$ reflectors was between 5 mm and 14 mm, as was also the case in Fig. 24.

Table 6. Average and standard deviation final cart centroid position after docking next to the RMMA taken over all 11 trials (as measured by the cart transporter controller log and in the OTS coordinate system). Note that the circular mean and circular standard deviation cart heading are also reported (see Ref. [52])

	Mean [Stdev] Position	
	RMMASq2	RMMASq3
Cart (x)	-319.601 mm [25.763 mm]	-1548.589 mm [43.793 mm]
Cart (z)	5402.415 mm [12.974 mm]	5457.58 mm [15.44 mm]
Vehicle (x)	-184.002 mm [25.209 mm]	-1684.05 mm [45.309 mm]
Vehicle (z)	5462.433 mm [14.074 mm]	5397.398 mm [19.077 mm]
	Mean [Stdev] Heading	
Cart (θ)	1.8°[0.769°]	-106.280°[159.029°]
Cart (Adjusted θ)	91.8°[0.769°]	-88.28°[1.983°]
	Circular Mean [Circular Stdev] Heading	
Cart (θ)	1.8°[0.012]	-178.280°[0.605]
Cart (Adjusted θ)	91.8°[0.012]	-88.28°[0.605]

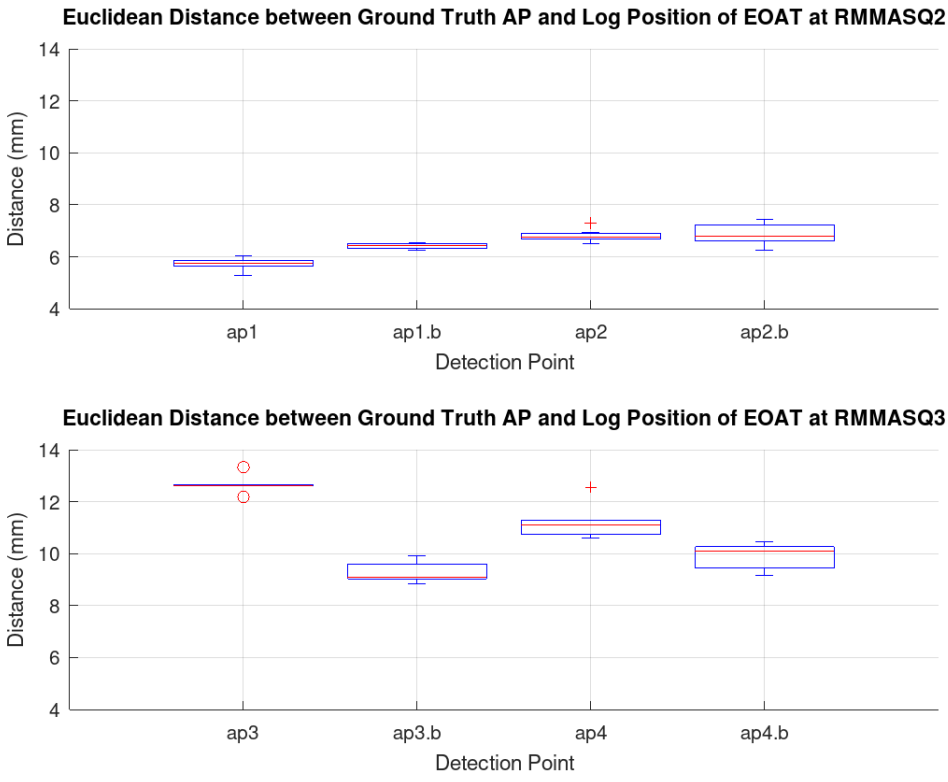

Fig. 26. Boxplots showing the 2D Euclidean distance between the final EOAT position (as measured by the robot controller log) when over the $\vec{ap}$ points and the ground truth static measurement of the $\vec{ap}$ points ('+' - Potential Outlier, 'O' - Outlier).

4.4 Comparison of Registration Methods

4.4.1 Experimental Model

Attention now turns to comparing the speed and accuracy of the two coordinate registration methods. To accomplish this, two response variables were compared as detailed in Sec. 3.1.1 - 3.1.3: the elapsed time taken to complete the coordinate registration in seconds (speed) and the initial-to-final spiral search distance required to localize the $\vec{ap}_1$ or $\vec{ap}_3$ reflectors in millimeters (accuracy). Aside from the registration method used, each response variable might have been influenced by the side of the RMMA at which the coordinate registration was performed, an interaction between the coordinate registration method used and the side of the RMMA at which the coordinate registration method was performed, and random experimental error.

Therefore, the analysis of each response variable was based on an effects model that consisted of a two-factor factorial design (Eq. 4 [53]). Here, y_{abc} was the response recorded (either the elapsed registration time or the initial-to-final spiral search distance); μ was the effect of the constant overall mean; τ_a was the effect due to the ath level of the factor "side", with $a = 1$ indicating the "RMMASq2" side of the RMMA and $a = 2$ indicating the "RMMASq3" side of the RMMA; β_b was the effect due to the bth level of the factor "coordinate registration method", with $b = 1$ indicating the edge method and $b = 2$ indicating the bisect method. Note that the factor "side" and the factor "coordinate registration method" were both considered fixed. The interaction between the factor "side" and the factor "coordinate registration method" was represented by $(\tau\beta)_{ab}$. Finally, ε_{abc} was the effect due to random experimental error, which was assumed to be normally, independently distributed with equal variance. The model adequacy checks for this assumption are presented in Sec. 4.4.4 for each response variable. The subscript c denoted the cth replicate and the variable n_{ab} denoted the total number of observations at the ath level of factor "side" and the bth level of factor "coordinate registration method". Again, note that n_{ab} was either five or six depending on the measured side of the RMMA.

For each response variable, the hypotheses given in Eq. 5 - 7 were tested using an analysis of variance (ANOVA). The decision rule for all hypotheses was to reject the null hypothesis if the corresponding p-value was less than 0.05. Otherwise, the null hypothesis was not rejected. It should also be noted that since two separate, univariate ANOVAs were conducted for each response variable (elapsed registration time and the initial-to-final spiral search distance for $\vec{ap}_1$ and $\vec{ap}_3$), the experiment-wise error may have been slightly inflated. Additionally, the interpretations of the conclusions in Sec. 4.4.2 should consider that there was evidence to suggest the assumption of equal variance might not have held for the samples of coordinate registration times (see Sec. 4.4.4).

$$y_{abc} = \mu + \tau_a + \beta_b + (\tau\beta)_{ab} + \varepsilon_{abc} \begin{cases} a = 1,2 \\ b = 1,2 \\ c = 1,2,...,n_{ab} \end{cases} \tag{4}$$

$$\begin{aligned} \mathcal{H}_0 &: \tau_1 = \tau_2 = 0 \\ \mathcal{H}_a &: \text{At least one } \tau_a \neq 0 \end{aligned} \tag{5}$$

$$\begin{aligned} \mathcal{H}_0 &: \beta_1 = \beta_2 = 0 \\ \mathcal{H}_a &: \text{At least one } \beta_b \neq 0 \end{aligned} \tag{6}$$

$$\begin{aligned} \mathcal{H}_0 &: (\tau\beta)_{ab} = 0 \text{ for all } a, b \\ \mathcal{H}_a &: \text{At least one } (\tau\beta)_{ab} \neq 0 \end{aligned} \tag{7}$$

It is important to note that since only five observations were obtained on the "RMMASq3" side of the RMMA, the experimental design was unbalanced. However, since n_{ab} satisfied Eq. 8, the design was proportional [54]. In Eq. 8, the dot notation denotes the sum or average over the respective subscript [55]. For example, $n_{a.}$ was the sum of the number of observations at the ath level of factor "side" over all levels of factor "coordinate registration method" and the $n_{..}$ was the sum of all observations over all levels of factor "side" and all levels of factor "coordinate registration method". This notation was used similarly with the response variable, y_{abc} when discussing the sum of the recorded responses. Since the number of observations for each response variable were proportional, modified formulas for the sum of squares (SS) were used to manually compute the ANOVA results for each comparison [54]. These formulas are replicated here as Eq. 9-13. However, it should be noted that the use of the adjusted, proportional ANOVA formulas could have resulted in conclusions that mostly, but not completely, align with those derived from an ANOVA conducted on a full, balanced factorial design [54].

$$n_{ab} = \frac{n_{a.} n_{.b}}{n_{..}} \tag{8}$$

$$\mathcal{SS}_{Total} = \sum_{a=1}^{2} \sum_{b=1}^{2} \sum_{a=1}^{n_{ab}} y_{abc}^2 - \frac{y_{...}^2}{n_{..}} \tag{9}$$

$$\mathcal{SS}_{Side} = \sum_{a=1}^{2} \frac{y_{a..}^2}{n_{a.}} - \frac{y_{...}^2}{n_{..}} \tag{10}$$

$$\mathcal{SS}_{Coordn.Reg.Method} = \sum_{a=1}^{2} \frac{y_{.b.}^2}{n_{.b}} - \frac{y_{...}^2}{n_{..}} \tag{11}$$

$$\mathcal{SS}_{Interaction} = \sum_{a=1}^{2} \sum_{b=1}^{2} \frac{y_{ab.}^2}{n_{ab}} - \frac{y_{...}^2}{n_{..}} \tag{12}$$

$$\mathcal{SS}_{Error} = \mathcal{SS}_{Total} - \mathcal{SS}_{Side} - \mathcal{SS}_{Coordn.Reg.Method} - \mathcal{SS}_{Interaction} \tag{13}$$

4.4.2 Comparing the Speed of the Coordinate Registration Methods

The next test proceeded to focus on the hypotheses of Eq. 5 - 7, which compared the speed of the registration methods. The inner four cells of Table 7 show the values of the individual responses (i.e., the initial-to-final spiral search distance in millimeters for either $\vec{ap}_1$ or $\vec{ap}_3$) for each observation and across each factor combination. Note the bisect registration that took 54.525 seconds and the bisect registration that took 49.548 seconds. These coordinate registrations were the only ones that required a coarse spiral search before the bisect registration could proceed. The outer four cells (the column-wise and row-wise sums) show the total number of observations captured and the sum of the responses when a specific factor level was held constant. For example, row three, column one shows that when the factor "coordinate registration method" was held constant to one (i.e., the edge coordinate registration method), a total of 11 observations and 188.135 seconds of elapsed coordinate registration time was observed. These values were used to verify the proportionality of the collected data with Eq. 8 and used as intermediate computations for the ANOVA results using Eq. 9 - 13. The results of the ANOVA are shown in Table 8.

Table 7. Two-factor factorial arrangement for registration time (in seconds). Cells (1, 1), (1, 2), (2, 1), and (2, 2) contain each of the observed responses for the corresponding factor level combination.

		Coordinate Registration Method		
		Edge ($b = 1$)	Bisect ($b = 2$)	Row Sum
Side	RMMASq2 ($a = 1$)	16.506s, 15.112s 13.325s, 14.767s 14.647s, 14.876s	48.243s, 47.458s 48.635s, 49.040s 48.658s, 48.257s	$n_{1.} = 12$ $y_{1..} = 379.524s$
	RMMASq3 ($a = 2$)	19.436s, 17.191s 20.947s, 19.254s 22.074s	49.650s, 48.261s 49.564s, 54.525s 49.548s	$n_{2.} = 10$ $y_{2..} = 350.450s$
	Column Sum	$n_{.1} = 11$ $y_{.1.} = 188.135s$	$n_{.2} = 11$ $y_{.2.} = 541.840s$	$n_{..} = 22$ $y_{...} = 729.974s$

Table 8. Analysis of variance for comparing registration time

Source of Variance	**Sum of Squares**[a]	**Degrees of Freedom**	**Mean Square**[a]	$\mathcal{F}_0$	**P-value**[b]
Side	63.724	1	63.724	26.144	< 0.01
Registration Method	5686.705	1	5686.705	2333.060	< 0.01
Interaction	12.114	1	12.114	4.970	Between 0.025 and 0.05
Error	43.874	18	2.437		
Total	5806.447	21			

[a] Measured in seconds squared [b] A probability

From the computed $\mathcal{F}_0$ values and associated p-values, which were determined from an $\mathcal{F}_0$ probability table, the following conclusions were noted [56]. Since the p-value associated with the hypothesis given in Eq. 5 was less than 0.05, the null hypothesis was rejected and it was concluded that there was sufficient evidence to suggest that the main effect of RMMA side on the registration speed was significant. Additionally, since the p-value associated with the hypothesis given in Eq. 6 was less than 0.05, the null hypothesis was rejected and it was concluded that there was sufficient evidence to suggest that the main effect of the coordinate registration method on the registration speed was significant. Finally, since the p-value associated with the hypothesis given in Eq. 7 was less than 0.05, the null hypothesis was rejected and it was concluded that there was sufficient evidence to suggest that the effect of the interaction between RMMA side and coordinate registration method was also significant. For each of these three conclusions, it was possible that a type I error was made. However, the probability of such an occurrence was given by the respective p-value for each conclusion, though this probability could have been inflated due to evidence that suggested the assumption of equal variance was violated (see Sec. 4.4.4).

Fig. 27 shows the sample average response for each factor level, which was examined as part of the comparison in light of the significant interaction effect indicated by the ANOVA. In summary, Fig. 27 appeared to be consistent with the conclusion derived from the ANOVA that there was sufficient evidence to suggest that the registration time was significantly different between the edge coordinate registration method and the bisect coordinate registration method. More specifically, in Fig. 27, the blue line showing the sample average edge registration time was consistently and notably lower than the orange line showing the sample average bisect registration time. Furthermore, also aligning with the ANOVA conclusion that the effect due to RMMA side was significant, the sample average registration time of the "RMMASq2" side was consistently lower than the "RMMASq3" side in Fig. 27. However, since the two lines of the plot were almost parallel, Fig. 27 may have been inconsistent with the ANOVA conclusion that the interaction effect was significant. Since the p-value was close to the significance level of 0.05, it was possible that the ANOVA conclusion on interaction significance was impacted by the use of the proportional design or the evidence found that suggested the assumption of equal variance may not have held. Additionally, since the slope of the blue line between the sample average times of the edge method was slightly steeper than the orange line between the sample average times of the bisect method, Fig. 27 suggested that the registration time of the edge method was possibly more sensitive to the side of the RMMA than the registration time of the bisect method.

4.4.3 Comparing the Accuracy of the Registration Methods

Now, the test to evaluate the hypotheses in Eq. 5 - 7 to compare the accuracy of the two coordinate registration methods is described. The accuracy was indicated by the initial-to-final spiral search distance (mm) for either $\vec{ap}_1$ or $\vec{ap}_3$ (i.e., the first spiral search for an ap target that occurred immediately after coordinate registration). Table 9 was formatted

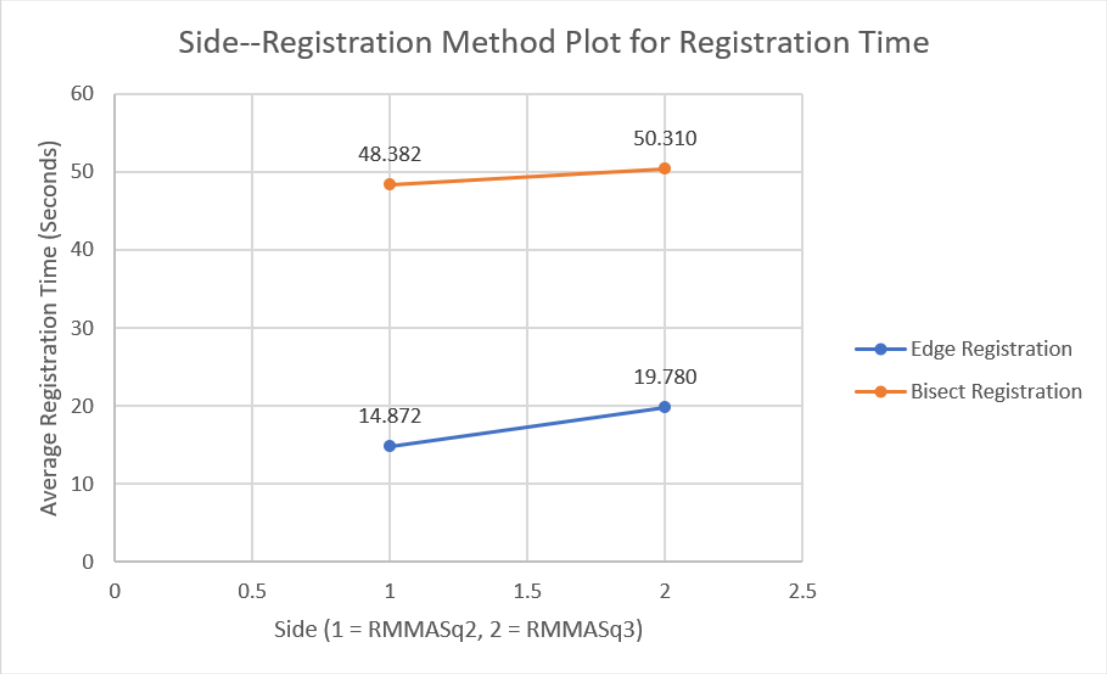

Fig. 27. Plot of the average registration time against each factor (side and coordinate registration method).

similarly to Table 7. Table 10 shows the corresponding ANOVA results for the initial-to-final spiral search distance.

Table 9. Two-factor factorial arrangement for initial-to-final spiral search distance for $\vec{ap}_1$ and $\vec{ap}_3$. Cells (1, 1), (1, 2), (2, 1), and (2, 2) contain each of the observed responses for the corresponding factor level combination.

		Coordinate Registration Method	
	Edge ($b = 1$)	Bisect ($b = 2$)	Row Sum
Side RMMASq2 ($a = 1$)	1.411 mm, 1.075 mm, 1.424 mm, 1.435 mm, 1.941 mm, 1.064 mm	2.495 mm, 2.462 mm, 1.801 mm, 2.510 mm, 1.865 mm, 2.498 mm	$n_{1.} = 12$ $y_{1..} = 21.980$ mm
RMMASq3 ($a = 2$)	1.824 mm, 0.035 mm, 1.068 mm, 1.303 mm, 1.208 mm	1.127 mm, 0.076 mm, 1.776 mm, 0.032 mm, 1.068 mm	$n_{2.} = 10$ $y_{2..} = 9.516$ mm
Column Sum	$n_{.1} = 11$ $y_{.1.} = 13.786$ mm	$n_{.2} = 11$ $y_{.2.} = 17.709$ mm	$n.. = 22$ $y_{...} = 31.496$ mm

Table 10. Analysis of variance for comparing the initial-to-final spiral search distance for $\vec{ap}_1$ and $\vec{ap}_3$

Source of Variance	**Sum of Squares**[c]	**Degrees of Freedom**	**Mean Square**[c]	$\mathcal{F}_0$	**P-value**[d]
Side	4.225	1	4.225	16.436	Between 0.025 and 0.05
Registration Method	0.670	1	0.670	0.261	> 0.25
Interaction	1.840	1	1.840	7.158	Between 0.01 and 0.025
Error	4.627	18	0.257		
Total	11.362	21			

[c] Measured in millimeters squared [d] A probability

From Table 10, the following conclusions were noted. Since the p-value associated with the hypothesis given in Eq. 5 was less than 0.05, the null hypothesis was rejected and it was concluded that there was sufficient evidence to suggest that the main effect of RMMA side on the coordinate registration accuracy was significant. In this conclusion, it was possible that a type I error was made, however the probability of such an occurrence is given by the respective p-value. Since the p-value associated with the hypothesis given in Eq. 6 was greater than 0.05, the null hypothesis was not rejected and it was concluded that there was not sufficient evidence to suggest that the main effect of the coordinate registration method on the coordinate registration accuracy was significant. In this conclusion, it was possible that a type II error was made and the probability of such an occurrence was unknown. Finally, since the p-value associated with the hypothesis given in Eq. 7 was less than 0.05, the null hypothesis was rejected and it was concluded that there was sufficient evidence to suggest that the effect of the interaction between RMMA side and coordinate registration method on the coordinate registration accuracy was significant. In this conclusion, it was

also possible that a type I error was made, and the probability of such an occurrence is given by the respective p-value.

Fig. 28 shows the sample average response for each factor level, which, similarly to Fig. 27, was examined as part of the comparison in light of the significant interaction suggested by the ANOVA. In summary, Fig. 28 appeared to support the conclusion from the ANOVA that the interaction effect between coordinate registration method and side was significant since the two lines did not exhibit parallelism and intersected. Fig. 28 also appeared to be consistent with the ANOVA conclusion that there was sufficient evidence to suggest that the accuracy of the coordinate registration was significantly different when performed between the "RMMASq2" side of the RMMA and the "RMMASq3" side of the RMMA because a larger sample average spiral search distance was observed on the "RMMASq2" side of the RMMA when compared with the "RMMASq3" side, though the magnitude of the difference indicated by Fig. 28 may not be considered practically meaningful. Considering the interaction displayed, Fig. 28 did not appear to necessarily contradict the ANOVA conclusion that there was not sufficient evidence to suggest that the accuracy of the coordinate registration was significantly different between the edge coordinate registration method and the bisect coordinate registration method.

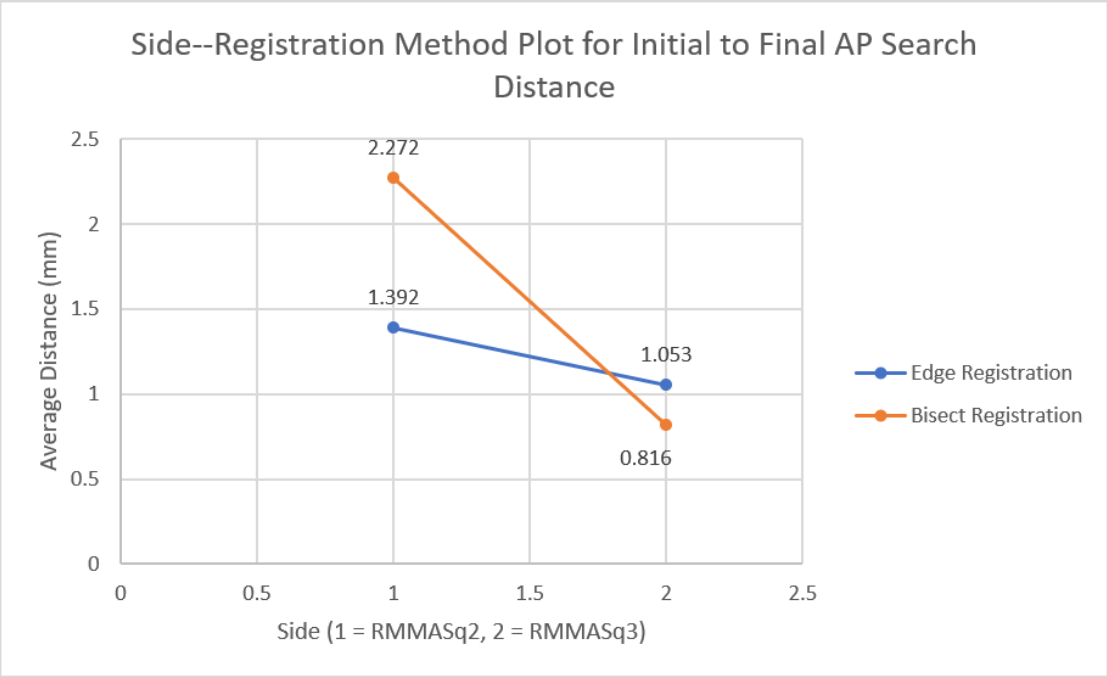

Fig. 28. Plot of the average initial-to-final spiral search distance for $\vec{ap}_1$ and $\vec{ap}_3$ against factors (side and coordinate registration method).

4.4.4 Residual Analysis for Checking Model Assumptions

To provide further validation for the reliability of the conclusions, the assumptions of normally, independently distributed errors with equal variance were checked for the samples by conducting a residual analysis of each response variable. The residuals were computed in a spreadsheet using the formula, $e_{abc} = y_{abc} - \bar{y}_{ab.}$. For any specific outlier values observed on the plot, the standardized residual was examined, which is given by the formula, $\mathscr{d}_{abc} = \frac{e_{abc}}{\sqrt{\mathcal{MS}_{Error}}}$, where $\mathcal{MS}_{Error}$ was the mean square (MS) error. Note that an observation was considered to be an outlier value if the standardized residual had an absolute value that was greater than three [55].

To investigate the assumption of normality, normal probability plots of the residuals were analyzed for each response variable, which are given in Fig. 29. Although some statistical software may also report the result of a statistical test, such as an Anderson-Darling test on the residuals, such tests often assume independence of the data being examined and residuals have been noted to not necessarily conform to this assumption [57]. It was for this reason that the normal probability plot of the residuals was the preferred method to detect severe departures from the normality assumption. The plots were generated using a Python-based statistics package [58, 59]. Figure 29 (Top) showed a generally linear relationship between the ordered residuals for registration time and the theoretical quantiles of the normal distribution. Only one positive residual, which had a value of 4.216 (measuring the Bisect method from the "RMMASq2" side of the RMMA), seemingly deviated more from this relationship when compared to the other residuals. A coarse spiral search was needed prior to this bisect coordinate registration and the time for the coarse spiral search was added to the total coordinate registration time. Since the registration times were logged automatically via the manipulator control code, this measurement was accepted as legitimate (not a recording error). Additionally, the standardized value for this residual was about 2.700, which was the only residual that had an absolute value greater than 2 (but still less than 3), and was therefore not considered a notable outlier. Figure 29 (Bottom) similarly showed a linear relationship when the ordered residuals for the initial-to-final spiral search distances for $\vec{ap}_1$ and $\vec{ap}_3$ were compared against the theoretical quantiles of the normal distribution. Here, the most notable residual that deviated from this relationship had a value of -1.017. The standardized value of this residual was about -2.007, which was again the only residual that had an absolute value greater than 2 (but still less than 3), and was therefore also not deemed a notable outlier. Since there was no reason to suspect possible violations of the normality assumption based on the normal probability plot, it was assumed that the error distributions were approximately normal.

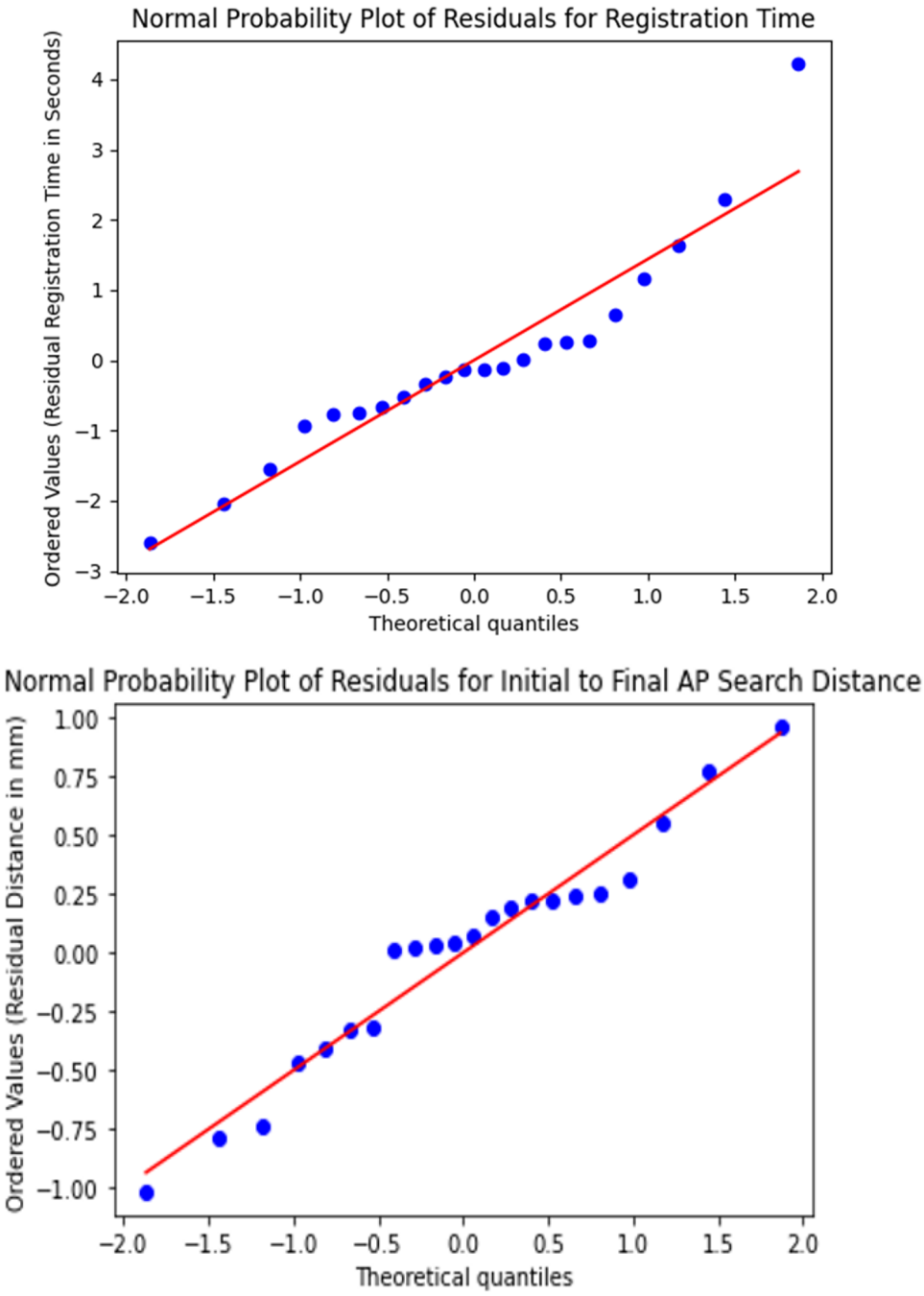

Fig. 29. Normal probability plot of the residuals for registration time in seconds (Top) and of the residuals for the initial-to-final spiral search distances for $\vec{ap}_1$ and $\vec{ap}_3$ in mm (Bottom).

To investigate the assumption of independently distributed errors, the primary interest was in verifying no strong correlation was present in the residuals [57]. Since the presence of autocorrelation, where adjacent observations might display correlation, is a strong indication of non-randomness in data, the residuals versus run order plots in Fig. 30 were analyzed first [55, 60, 61]. In such plots positive autocorrelation could graphically manifest as a sequence of either positive or negative residuals, while negative autocorrelation might manifest in a rapid oscillation in the signs of the residuals [57, 62]. In Fig. 30 (Top), a general downward trend was observed from runs 1 - 7. Additionally, runs 7-10 showed a group of three residuals that were negative, but generally increasing. The behavior from runs 1-10, therefore, resembled a concave up curvature. The residuals then tended to be higher around runs 16 and 17. Runs 10-22 appeared to display a more random distribution of residuals. Upon first glance, Fig. 30 (Bottom), appeared to show a more random distribution of the residuals overall. However, close inspection revealed possible slight periodic behavior since the residuals for runs 1-4 were mostly positive, the residuals for runs 5-10 were mostly negative, and the residuals for runs 10-15 were mostly positive again. This behavior suggested the possibility of slight serial autocorrelation. Interpretation of these plots was assisted using information from several resources [57, 63, 64].

Given the observations noted from the residuals versus run order plots in Fig. 30, the Durbin-Watson statistical test was used to investigate the possibility of positive and/or negative autocorrelation [60]. In using the Durbin-Watson test, two hypotheses were tested: one that tested for the presence of positive autocorrelation and one that tested for the presence of negative autocorrelation. The null hypothesis stated that there was no positive (or negative) autocorrelation, while the alternative hypothesis stated that there was positive (or negative) autocorrelation [60]. The null hypothesis was rejected or not rejected at the 0.05 significance level. The Durbin-Watson statistic was computed using a Python-based statistics package [65]. For each response variable, the corresponding residuals were entered into an array and sorted by run order before input into the Durbin-Watson function. The Durbin-Watson statistic was found to be 1.716 ($\mathscr{D}_1$) for the residuals of registration times and 2.006 ($\mathscr{D}_2$) for the residuals of the initial-to-final spiral search distances for AP1 and AP3.

A table of upper and lower bounds on the critical values for the Durbin-Watson statistic was used to determine the significance of the $\mathscr{D}_1$ and $\mathscr{D}_2$ values [60]. If the Durbin-Watson statistic was less than $\mathscr{D}_L$, the null hypothesis was rejected. If the Durbin-Watson statistic was greater than $\mathscr{D}_U$, the null hypothesis was not rejected. Otherwise, if the Durbin-Watson statistic was between $\mathscr{D}_L$ and $\mathscr{D}_U$, then the test was inconclusive [60]. The bounds on the Durbin-Watson statistic at the 0.05 significance level and when $n = 22$ are provided in Table 11. To look up the appropriate bounds in the critical value table, which was needed to test the related hypotheses, the number of regressors associated with Eq. 4, when expressed as a linear regression model for the residuals of each response variable, needed to be determined. The regressors were determined to have at least included one term for each significant factor (i.e., RMMA side, coordinate registration method, and/or interaction) and a constant intercept term. Since some terms were possibly considered insignificant

depending on the response variable, and would therefore be omitted from the model, the critical value bounds for all cases are provided (one regressor, two regressors, and three regressors).

Table 11. Bounds on the Durbin-Watson statistic at the 0.05 significance level for $n = 22$ [60]. Note that the number of terms included the intercept.

	$n_{...} = 22$ $\alpha = 0.05$	$\mathcal{D}_L$	$\mathcal{D}_U$
Terms	2	1.239	1.429
	3	1.147	1.541
	4	1.053	1.664

First, a test for positive autocorrelation on the residuals of each response was implemented. When $n_{...} = 22$ and three regressors were present, $\mathcal{D}_1$ was greater than $\mathcal{D}_U$. Therefore, the null hypothesis was not rejected and it was concluded that there was not sufficient evidence to suggest that a positive autocorrelation existed for the residuals of registration times. In this conclusion it was possible that a type II error was made, and the probability of this having occurred was unknown. Furthermore, When $n_{...} = 22$ and three regressors were present, $\mathcal{D}_2$ was greater than $\mathcal{D}_U$. Therefore, the null hypothesis was not rejected and it was concluded that there was not sufficient evidence to suggest that a positive autocorrelation existed for the residuals of the initial-to-final spiral search distance for $\vec{ap}_1$ and $\vec{ap}_3$. In this conclusion it was possible that a type II error was made, and the probability of this having occurred was unknown.

For testing the hypotheses related to possible negative autocorrelation, $4 - \mathcal{D}_1 = 2.284$ and $4 - \mathcal{D}_2 = 1.994$ and was instead compared to the $\mathcal{D}_L$ and $\mathcal{D}_U$ values. When $n_{...} = 22$ and three regressors were present, $4 - \mathcal{D}_1$ was greater than $\mathcal{D}_U$. Therefore, the null hypothesis was not rejected and it was concluded there was not sufficient evidence to suggest that negative autocorrelation existed for the residuals of registration times. In this conclusion, it was possible that a type II error was made, and the probability of this having occurred was unknown. Furthermore, When $n_{...} = 22$ and three regressors were present, $4 - \mathcal{D}_2$ was greater than $\mathcal{D}_U$. Therefore, the null hypothesis was not rejected and it was concluded that there was not sufficient evidence to suggest that a negative autocorrelation existed for the residuals of the initial-to-final spiral search distances for $\vec{ap}_1$ and $\vec{ap}_3$. In this conclusion it was possible that a type II error was made, and the probability of this having occurred was unknown. Given these conclusions, there was no reason to suspect that the independence assumption on the errors was significantly violated for each response variable.

Finally, the assumption of equal variance for the error distribution was investigated using both graphical methods on the residuals and statistical tests on the sample data. Figure 31 plots the residuals versus fitted values for the elapsed coordinate registration time. From the plot, some possible mild inequality of variance was observed. Additionally, from Fig. 32 and 33, which plotted the residuals against each factor level, it was observed that

the variance of the residuals may have increased between the "RMMASq2" side (which had the larger sample size) and "RMMASq3" side (which had the smaller sample size). The funnel shape of the residuals in Fig. 32 was concerning because such an occurrence suggested possible additional inflation of the type I error in the conducted ANOVA. Additionally, when the largest residual for the bisect registration was ignored in Fig. 33, the plot also resembled a funnel shape that indicated possible inequality of variance. This further emphasized the importance of a balanced design for future experiments, since ANOVAs applied to unbalanced data are less robust to mild departures from the normality and equal variance assumptions. Additionally, this observation suggested that the analysis techniques used in this work may not be as reliable when applied to similar experiments that might be extended to include random effects [57]. Figure 34 shows the corresponding residuals versus fits plots for the initial-to-final spiral search distances for $\vec{ap}_1$ and $\vec{ap}_3$. From Fig. 35, which plotted the residuals against each measured side of the RMMA, similarities were again observed with Fig. 32, with a funnel shape that indicated a possible increase in variance between the "RMMASq2" side and the "RMMASq2" side. The plot shown in Fig. 35, however did not exhibit any other concerning structure to the residuals.

Given the structure observed in Fig. 32 and Fig. 35, statistical tests were applied to the sample data to further investigate the assumption of equal variance for the error of each response variable. For the first test, the null hypothesis stated that the samples of registration times all came from a population with equal variance, while the alternative hypothesis stated that at least one sample of registration times did not come from a population with equal variance. Since the error of the registration time data was assumed to conform to the normality assumption, the decision rule was based on the p-value computed from Bartlett's test and compared to the 0.05 significance level [66]. Specifically, if the p-value was less than 0.05, the null hypothesis was rejected. Otherwise, the null hypothesis was not rejected. Since the p-value was 0.027, which was less than 0.05, the null hypothesis was rejected and it was concluded that there was sufficient evidence to suggest that at least one sample of registration times did not come from a population with equal variance. In this conclusion, it was possible that a type I error was made, however the probability of such an occurrence was 0.027.

Furthermore, a statistical test was applied to the initial-to-final spiral search distance data. Again, the null hypothesis stated that the samples of initial-to-final spiral search distances all came from a population with equal variance, and the alternative hypothesis stated that at least one sample of initial-to-final spiral search distances did not come from a population with equal variance. Since the error of the initial-to-final spiral search distance data was assumed to conform to the normality assumption, the decision rule was again based on the p-value computed from Bartlett's test and compared to the 0.05 significance level [66]. Specifically, if the p-value was less than 0.05, the null hypothesis was rejected. Otherwise, the null hypothesis was not rejected. Since the p-value was 0.213, which was greater than 0.05,the null hypothesis was not rejected and it was concluded that there was not sufficient evidence to suggest that at least one sample of initial-to-final spiral search distances did not come from a population with equal variance. In this conclusion, it was

possible that a type II error was made, however the probability of such an occurrence was unknown. In summary, the residual versus fits plot and statistical tests suggested there was reason to suspect that the assumption of equal variance was violated for the error of the registration time samples. Hence, interpretation of the conclusions drawn from the corresponding ANOVA on the registration times should consider the impact of the equal variance assumption. However, given the result of Bartlett's test, it was also determined there was not sufficient evidence to suggest that the assumption of equal variance was violated on the samples of initial-to-final spiral search distances, which further supported the conclusions drawn from the corresponding ANOVA.

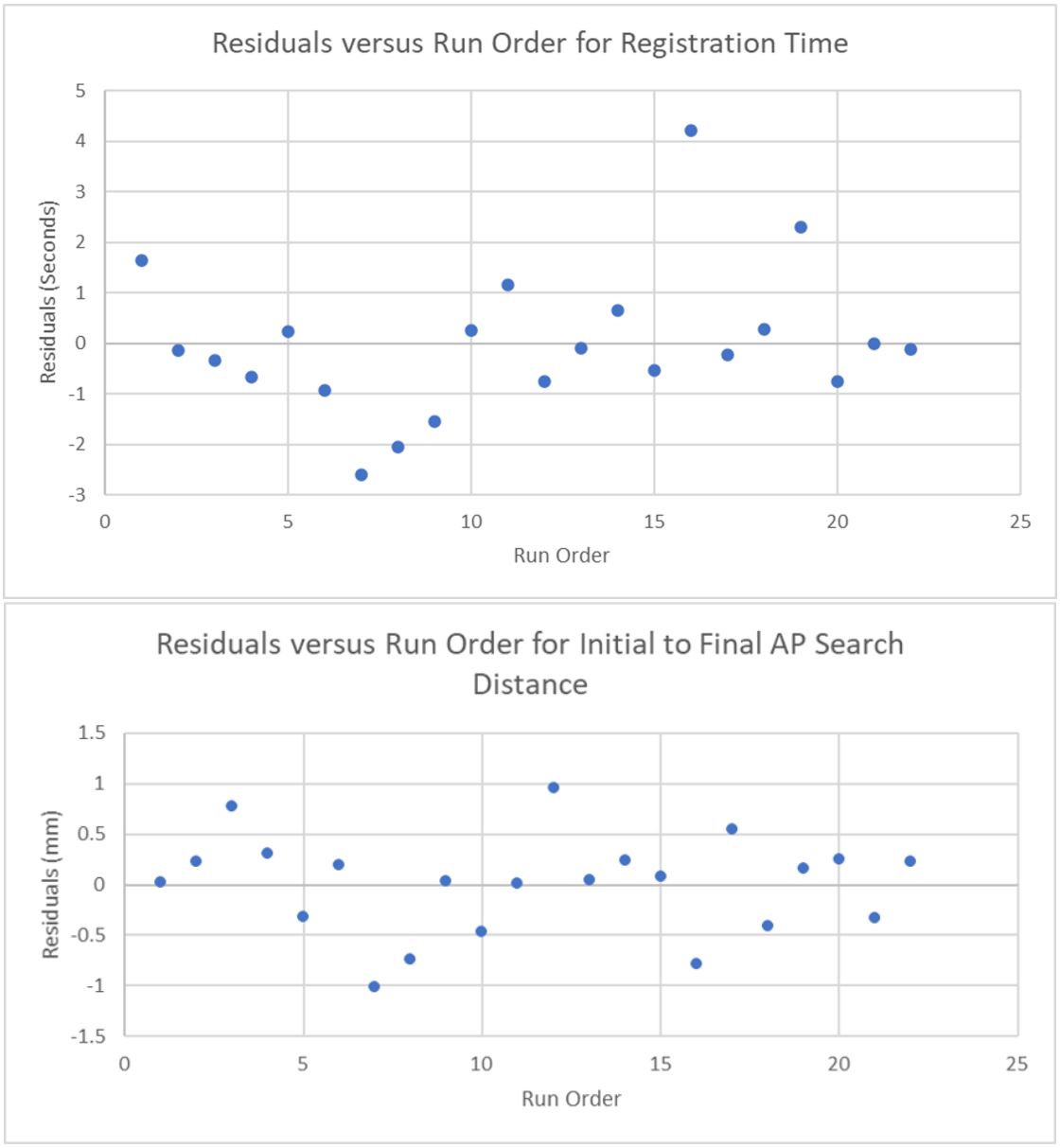

Fig. 30. Residuals vs. run order plot for registration time in seconds (Top) and the initial-to-final spiral search distances for $\vec{a}p_1$ and $\vec{a}p_3$ in mm (Bottom).

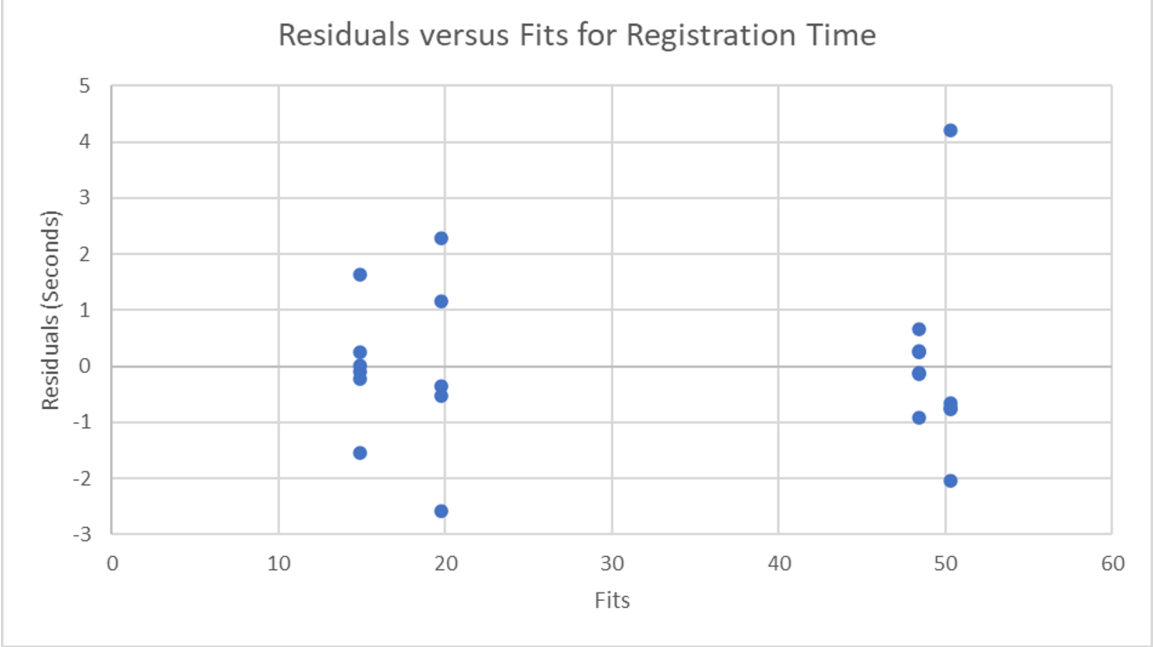

Fig. 31. Residuals vs. fits plot for registration time in seconds.

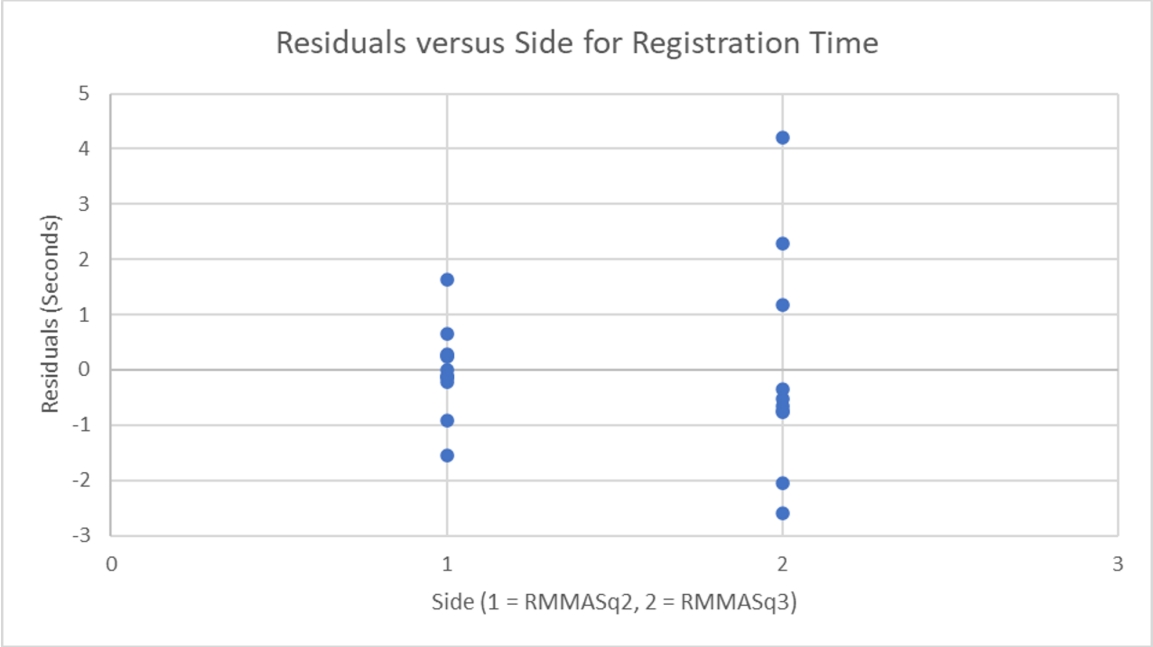

Fig. 32. Residuals vs. side plot for registration time in seconds.

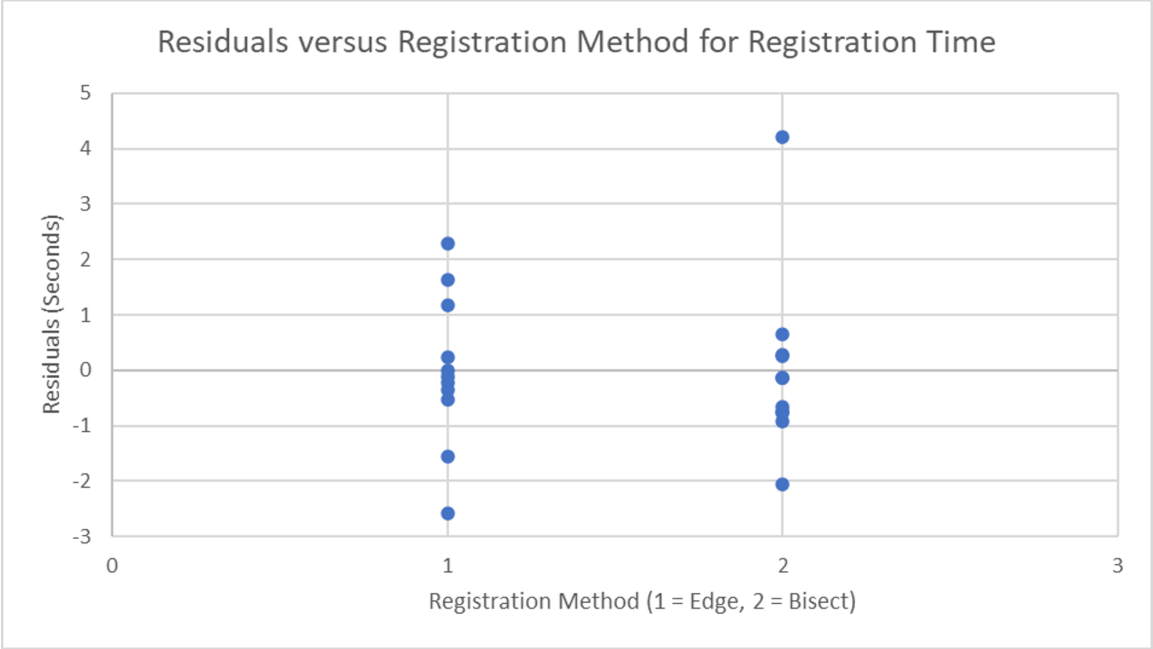

Fig. 33. Residuals vs. coordinate registration method plot for registration time in seconds.

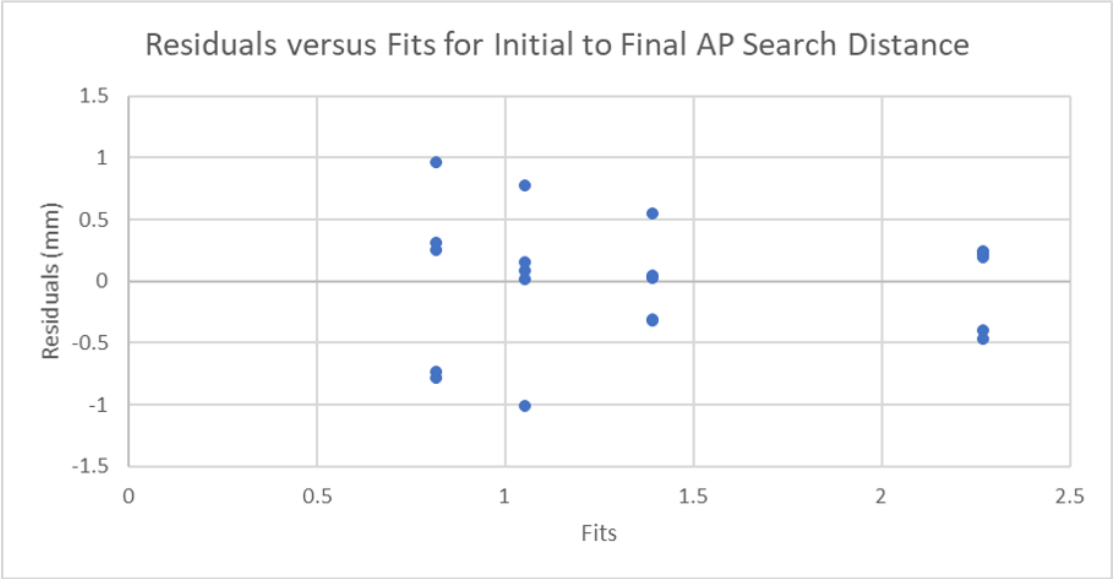

Fig. 34. Residuals vs. fits plot for the initial-to-final spiral search distances for $\vec{ap}_1$ and $\vec{ap}_3$.

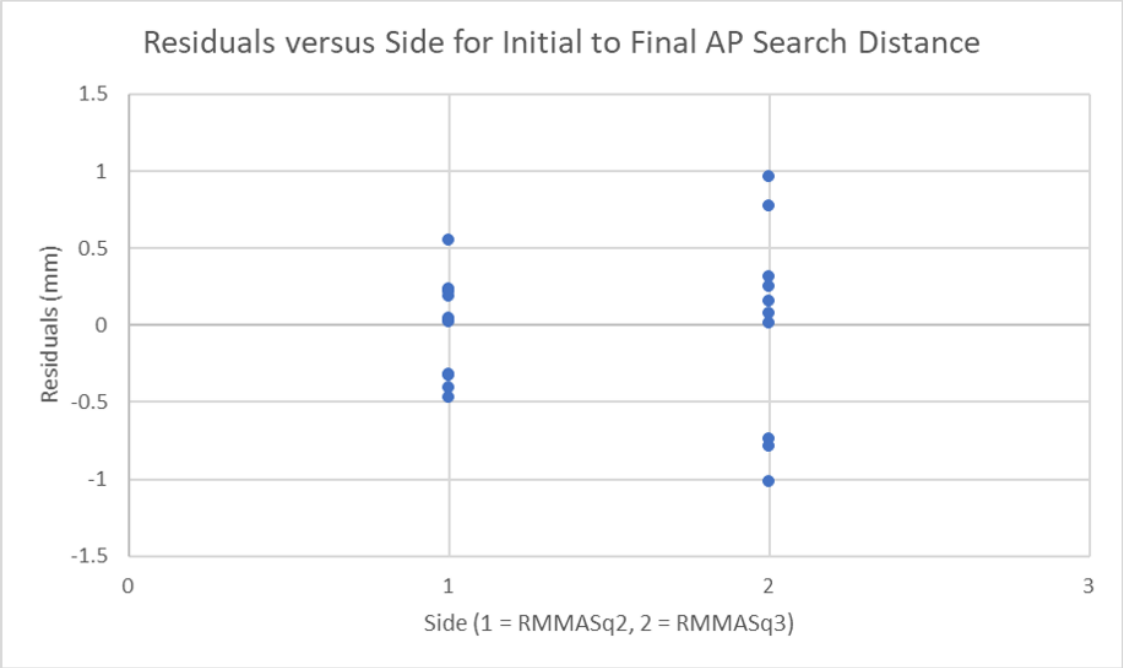

Fig. 35. Residuals vs. side plot for the initial-to-final spiral search distance for $\vec{a}p_1$ and $\vec{a}p_3$.

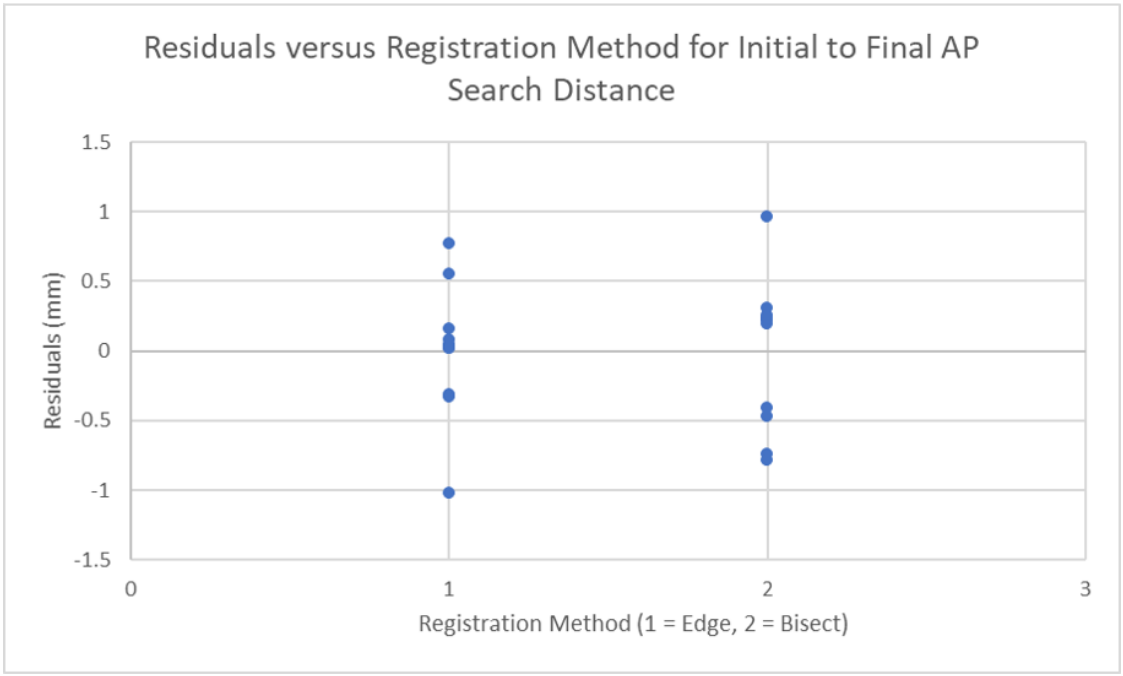

Fig. 36. Residuals vs. coordinate registration method plot for the initial-to-final spiral search distances for $\vec{a}p_1$ and $\vec{a}p_3$.

4.5 Assessment of Cart Leveling

4.5.1 Experimental Model

Attention now turns to analyzing the angle readings obtained by the digital levels during the experiment. Table 12 displays the average of ten angle readings for each of the 11 trials (rounded to the nearest thousandth of a degree). Note that the data for each level (front or side) was separated into two samples: The readings taken when the cart was docked at "RMMASq2" vs. the readings taken when the cart was docked at "RMMASq3". Since the "RMMASq3" goal point was rotated 180 degrees from the "RMMASq2" goal, the sign of the digital level readings was reversed for the readings taken at "RMMASq3". From this, the reported difference between the sample averages of the digital level readings taken from the two sides of the RMMA by the front level was 0.67°. Additionally, the equivalent difference for the side level was 0.222°. In an attempt to determine if the difference between the samples was statistically significant, inferential statistical tests were applied on the two samples for each digital level. Textbooks were used as references to develop the hypothesis tests, which were also applied using a Python-based statistics library [55, 58, 67]. For each level, the goal was to determine if there was a significant difference in angle reading between the two docking locations.

Two hypotheses (i.e., one hypothesis for testing the front level and one hypothesis for testing the side level) were tested on the population means of angle readings based on two independent samples (i.e., the sample of angle readings taken from "RMMASq2" vs. the sample of level readings taken from "RMMASq3"). Equations 14-15 summarize the main hypotheses tested. Before addressing the main hypotheses, however, it should be noted that the appropriate statistical test was selected based on the conducted model adequacy checks (see Sec. 4.5.3) to test the assumptions of normality and equal variance for each sample. These assumptions needed to be specifically validated because the sample size of the level readings for each side $(5-6)$ was small enough to prevent satisfaction by appealing to the Central Limit Theorem [68]. It should be noted that for all tested hypotheses in Sec. 4.5.2, the decision rule was to reject or not reject the null hypothesis based on the 0.05 significance level.

$$\begin{aligned} \mathcal{H}_0 &: \mu_{front,rmmsq2} = \mu_{front,rmmsq3} \\ \mathcal{H}_a &: \mu_{front,rmmsq2} \neq \mu_{front,rmmsq3} \end{aligned} \tag{14}$$

$$\begin{aligned} \mathcal{H}_0 &: \mu_{side,rmmsq2} = \mu_{side,rmmsq3} \\ \mathcal{H}_a &: \mu_{side,rmmsq2} \neq \mu_{side,rmmsq3} \end{aligned} \tag{15}$$

4.5.2 Comparing the Front and Side Level Readings

Focus now shifts to the hypothesis given in Eq. 14. Since, based on the tests in Sec. 4.5.3, it was assumed that both samples, that is the sample of front level readings taken

Table 12. Digital level angle readings per trial with the mean and standard deviation across trials. Note that the circular mean and circular standard deviation angle readings across trials are also reported (see Ref. [52]).

Trial	Goal	Front Level	Side Level
1	RMMASq2	0.028°	−0.010°
2	RMMASq3	0.086°	0.202°
3	RMMASq2	0.020°	0.037°
4	RMMASq3	0.116°	0.528°
5	RMMASq2	0.037°	0.016°
6	RMMASq3	0.094°	0.175°
7	RMMASq2	0.047°	0.091°
8	RMMASq3	0.094°	0.295°
9	RMMASq2	0.016°	0.018°
10	RMMASq3	0.095°	0.116°
11	RMMASq2	0.030°	0.096°
Mean [Stdev]	RMMASQ2	0.030° [0.011°]	0.041° [0.043°]
Mean [Stdev]	RMMASQ3	0.097° [0.011°]	0.263° [0.161°]
Circular Mean [Circular Stdev]	RMMASQ2	0.030° [0.000]	0.041° [0.001]
Circular Mean [Circular Stdev]	RMMASQ3	0.097° [0.604]	0.263° [0.604]

when the cart was docked at "RMMASq2" and the sample of front level readings taken when the cart was docked at "RMMASq3", came from normally distributed populations with equal variance, the two-sample independent t-test was used to evaluate the hypothesis [69]. From this test, it was found that the p-value was almost zero and less than 0.05. Therefore, the null hypothesis was rejected and it was concluded that there was sufficient evidence to suggest the population mean of the mean front digital level readings recorded at "RMMASq2" and the population mean of the mean front digital level readings recorded at "RMMASq3" were different. In this decision, it was possible that a type I error was made, and the probability of such an occurrence was almost zero.

Next, the hypothesis given in Eq. 15 was tested. Again, it was assumed that both samples, that is the sample of side level readings taken when the cart was docked at "RMMASq2" and the sample of side level readings taken when the cart was docked at "RMMASq3", came from normally distributed populations. However, due to the results presented in Sec. 4.5.3, it was not assumed that the sample of side level readings came from populations with equal variance. Therefore, the hypothesis was instead evaluated using the Welch's t-test [69]. From this test, it was found that the p-value was 0.035, which was less than 0.05. Therefore, the null hypothesis was rejected and it was concluded that there was sufficient evidence to suggest the population mean of the mean side digital level readings recorded at "RMMASq2" and the population mean of the mean side digital level readings recorded at "RMMASq3" were different. In this decision, it was possible that a type I error was made, and the probability of such an occurrence was 0.035. In summary, from the analysis presented in this section, it was concluded that there was reason to suspect that the

leveling of the cart varied between the "RMMASq2" and "RMMASq3" stops along both axes that were measured by the two levels. It was speculated that an inconsistent floor leveling combined with the use of the linear actuators could have contributed to this difference in leveling. Therefore, future data calibrations applied to the mobile manipulator-on-a-cart system, like that presented in Sec. 4.1.3, should take the inconsistent floor leveling into account.

4.5.3 Checking Model Assumptions for the Digital Level Readings

For testing the normality assumption, the Anderson-Darling test was applied to each of the two angle reading samples for the front and side digital levels [70]. For testing the assumption of equal variance between the two samples for each level, Bartlett's test was used [66]. Then, to check for the presence of autocorrelation, residual vs. run-order plots and the Durbin-Watson test were utilized.

First, the normality assumption on the samples of level readings was tested. For the front digital level, the following hypothesis was tested on the sample of level readings that were taken while the cart was docked at "RMMASq2". The null hypothesis stated that the sample of mean front digital level readings recorded at "RMMASq2" came from a normally distributed population. The alternative hypothesis stated that the sample of mean front digital level readings recorded at "RMMASq2" did not come from a normally distributed population. For this test, the decision rule was based on the value of the critical value and the Anderson-Darling statistic at the 0.05 significance level. Therefore, if the statistic was greater than 0.809, the null hypothesis was rejected. Otherwise, the null hypothesis was not rejected. The statistic for this test was found to be 0.171, which was less than the critical value specified in the decision rule. Therefore, the null hypothesis was not rejected and it was concluded that there was not sufficient evidence to suggest that the sample of mean front digital level readings recorded at "RMMASq2" did not come from a normally distributed population. In this conclusion it was possible that a type II error was made, and the probability of this having occurred was unknown.

The following hypothesis was tested regarding the sample of front level readings that were taken while the cart was docked at "RMMASq3". The null hypothesis stated that the sample of mean front digital level readings recorded at "RMMASq3" came from a normally distributed population. The alternative hypothesis stated that the sample of mean front digital level readings recorded at "RMMASq3" did not come from a normally distributed population. For this test, the decision rule was again based on the value of the Anderson-Darling statistic at the 0.05 significance level. Therefore, if the statistic was greater than 0.984, the null hypothesis was rejected. Otherwise, the null hypothesis was not rejected. The statistic for this test was found to be 0.599, which was less than the critical value specified in the decision rule. Therefore, the null hypothesis was not rejected and it was concluded that there was not sufficient evidence to suggest that the sample of mean front digital level readings recorded at "RMMASq3" did not come from a normally distributed population. In this conclusion it was possible that a type II error was made, and

the probability of this having occurred was unknown.

For the side digital level, the following hypothesis were tested on the sample of level readings that were taken while the cart was docked at "RMMASq2". The null hypothesis stated that the sample of mean side digital level readings recorded at "RMMASq2" came from a normally distributed population. The alternative hypothesis stated that the sample of mean side digital level readings recorded at "RMMASq2" did not come from a normally distributed population. For this test, the decision rule was based on the value of the Anderson-Darling statistic at the 0.05 significance level. Therefore, if the statistic was greater than 0.809, the null hypothesis was rejected. Otherwise, the null hypothesis was not rejected. The statistic for this test was found to be 0.379, which was less than the critical value specified in the decision rule. Therefore, the null hypothesis was not rejected and it was concluded that there was not sufficient evidence to suggest that the sample of mean side digital level readings recorded at "RMMASq2" did not come from a normally distributed population. In this conclusion it was possible that a type II error was made, and the probability of this having occurred was unknown.

The focus now shifts to the test conducted on the following hypothesis concerning the sample of side level readings that were taken while the cart was docked at "RMMASq3". The null hypothesis stated that the sample of mean side digital level readings recorded at "RMMASq3" came from a normally distributed population. The alternative hypothesis stated that the sample of mean side digital level readings recorded at "RMMASq3" did not come from a normally distributed population. For this test, the decision rule was again based on the critical value and the Anderson-Darling statistic at the 0.05 significance level. Therefore, if the statistic was greater than 0.984, the null hypothesis was rejected. Otherwise, the null hypothesis was not rejected. The statistic for this test was found to be 0.376, which was less than the critical value specified in the decision rule. Therefore, the null hypothesis was not rejected and it was concluded that there was not sufficient evidence to suggest that the sample of mean front digital level readings recorded at "RMMASq3" did not come from a normally distributed population. In this conclusion it was possible that a type II error was made, and the probability of this having occurred was unknown.

To investigate the assumption of independently distributed errors, it was again important to check for the presence of autocorrelation in the residuals. The following observations were noted from the front-level residuals vs. run-order plot in Fig. 37 (Top). In runs 2-3, the residuals tended to be negative. However, in runs 4-7, the residuals were generally positive, with only one negative residual. In runs 4-6, a general downward trend was displayed. Finally, in runs 9-11, the residuals were generally negative, but increasing. For the side-level residuals in Fig. 37 (Bottom), the residuals were negative for runs 1-3 and slightly increasing. In run 4, a large positive residual occurred, before the sequence of negative residuals in runs 5-6. In runs 7-10 a sequence of residuals occurred that started positive and then decreased to below zero. Finally, a positive residual occurred for run 11.

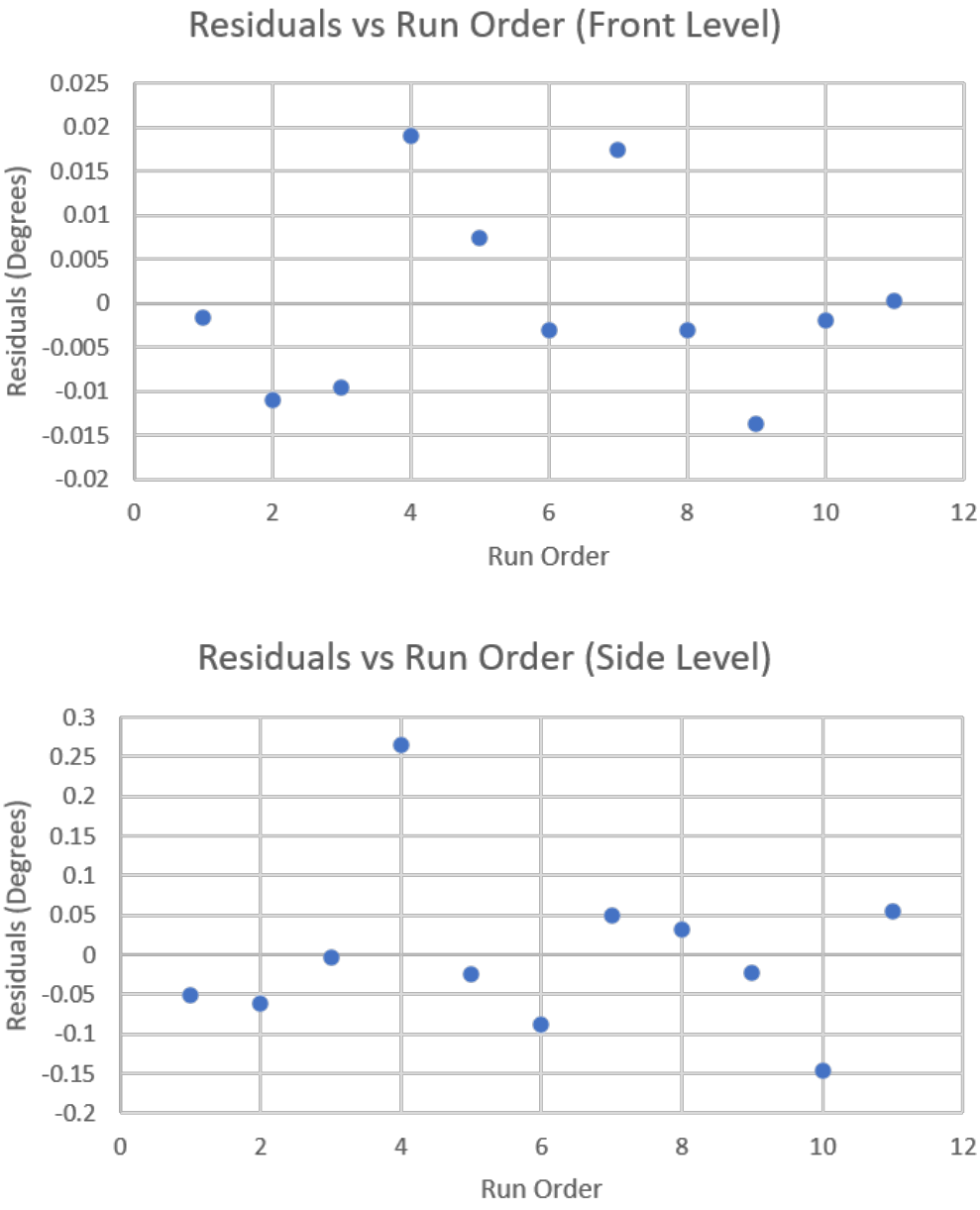

Fig. 37. Residuals vs. run order plot for average front digital level readings (Top) and average side digital level readings (Bottom) in degrees.

Based on the observations from the residuals vs. run-order plot, the Durbin-Watson test was again applied to statistically test two hypotheses on the residuals obtained from each digital level: one for the presence of positive autocorrelation and one for the presence of negative autocorrelation in the average readings from the front digital level [60]. The null hypothesis stated that there was no positive (or negative) autocorrelation, while the alternative hypothesis stated that there was positive (or negative) autocorrelation [60]. The null hypothesis was again rejected or not rejected at the 0.05 significance level, and the Durbin-Watson statistic was computed using a Python-based statistics package [65]. For the readings taken from each digital level, the corresponding residuals were again computed and stored in an array sorted by run-order. The Durbin-Watson statistic was found to be 1.959 ($\mathcal{D}_3$) for the front digital level residuals and 2.133 ($\mathcal{D}_4$) for the side digital level residuals.

When the effects model corresponding to the hypothesis in Eq. 14 was expressed as a linear regression model, the linear regression model had two terms: one for the effect of measured RMMA side and a constant intercept. Therefore, since the sample size was 11 for the sample of average front digital level readings, $\mathcal{D}_L = 0.927$ and $\mathcal{D}_U = 1.324$.

First, a test for positive autocorrelation was applied. Since $\mathcal{D}_3 = 1.959$ was greater than $\mathcal{D}_U = 1.324$, the null hypothesis was not rejected and it was concluded that there was not sufficient evidence to suggest that a positive autocorrelation existed for the residuals of the average digital level readings recorded by the front digital level. In this conclusion it was possible that a type II error was made, and the probability of this having occurred was unknown. Since $\mathcal{D}_4 = 2.133$ was greater than $\mathcal{D}_U = 1.324$, the null hypothesis was not rejected and it was concluded that there was not sufficient evidence to suggest that a positive autocorrelation existed for the residuals of the average digital level readings recorded by the side digital level. In this conclusion it was possible that a type II error was made, and the probability of this having occurred was unknown.

For the test of negative autocorrelation, $4 - \mathcal{D}_3 = 2.041$ and $4 - \mathcal{D}_4 = 1.867$ were compared to $\mathcal{D}_L$ and $\mathcal{D}_U$ values. Since $4 - \mathcal{D}_3$ was greater than $\mathcal{D}_U = 1.324$, the null hypothesis was not rejected and it was concluded that there was not sufficient evidence to suggest that a negative autocorrelation existed for the residuals of the average digital level readings recorded by the front digital level. In this conclusion it was possible that a type II error was made, and the probability of this having occurred was unknown. Given these conclusions, it was unlikely that the independence assumption on the error was significantly violated for each response. Since $4 - \mathcal{D}_4$ was greater than $\mathcal{D}_U = 1.324$, the null hypothesis was not rejected and it was concluded that there was not sufficient evidence to suggest that a negative autocorrelation existed for the residuals of the average digital level readings recorded by the side digital level. In this conclusion it was possible that a type II error was made, and the probability of this having occurred was unknown. Given these conclusions, there was no reason to suspect that the independence assumption on the error was significantly violated for each response.

The assumption of equal variance was then tested between the two samples of level readings from the front digital level. For this test, the null hypothesis stated that the sam-

ple of mean front digital level readings recorded at "RMMASq2" and the sample of mean front digital level readings recorded at "RMMASq3" came from populations with equal variance. The alternative hypothesis stated that the sample of mean front digital level readings recorded at "RMMASq2" and the sample of mean front digital level readings recorded at "RMMASq3" did not come from populations with equal variance. The decision rule was based on the p-value computed from Bartlett's test and compared to the 0.05 significance level [66]. Therefore, if the p-value was less than 0.05, the null hypothesis was rejected. Otherwise, the null hypothesis was not rejected. The p-value computed from Bartlett's test was found to be 0.991, which was greater than 0.05. Therefore, the null hypothesis was not rejected and it was concluded that there was not sufficient evidence to suggest that the sample of mean front digital level readings recorded at "RMMASq2" and the sample of mean front digital level readings recorded at "RMMASq3" did not come from populations with equal variance. In this conclusion it was possible that a type II error was made, and the probability of this having occurred was unknown.

Finally, the assumption of equal variance was tested between the two samples of level readings from the side digital level. For this test, the null hypothesis stated that the sample of mean side digital level readings recorded at "RMMASq2" and the sample of mean side digital level readings recorded at "RMMASq3" come from populations with equal variance. The alternative hypothesis stated that the sample of mean side digital level readings recorded at "RMMASq2" and the sample of mean side digital level readings recorded at "RMMASq3" did not come from populations with equal variance. The decision rule was based on the p-value computed from Bartlett's test in comparison to the 0.05 significance level [66]. Therefore, if the p-value was less than 0.05, the null hypothesis was rejected. Otherwise, the null hypothesis was not rejected. The p-value computed from Bartlett's test was found to be 0.014, which was less than 0.05. Therefore, the null hypothesis was rejected and it was concluded that there was sufficient evidence to suggest that the sample of mean side digital level readings recorded at "RMMASq2" and the sample of mean side digital level readings recorded at "RMMASq3" did not come from populations with equal variance. In this conclusion it was possible that a type II error was made, and the probability of this having occurred was unknown.

5. Conclusion

In this work, an artifact-based performance measurement test method was adapted for use with a mobile manipulator-on-a-cart. A complete overview of the system hardware, software, system configurations, and experimental design was provided, and the collected data across the robot controller logs, digital levels, and the OTS ground truth system was also outlined. The process used to select and aggregate the OTS data was described and the resulting marker standard deviation was validated against the previously established measurement uncertainty of the OTS. The calibration of coordinate transformations to allow for the robot data to be compared to the OTS marker data using the same OTS coordinate system as a reference was also described. The average and standard deviation position of

the EOAT and cart transporter using both the OTS marker data and the data acquired from the robot controller logs was plotted. Finally, the final position of the EOAT over the $\vec{ap}$ verification points was compared to the ground truth static measurements of the same target locations using the OTS. This data was used to identify and discuss possible sources of repeatability uncertainty in the mobile manipulator-on-a-cart system.

The uncertainty of the cart transporter docking performance and manipulator positioning was analyzed using the OTS and compared to measurements taken from the robot controller logs. After implementing the calibration, the plot shown in Fig. 23 was generated and the mean and standard deviation position of the cart transporter and EOAT were compared, with the accompanied data presented in Sec. 4.2. From the plot, a higher position variability in the cart transporter was observed on the "RMMASq3" side when compared to the "RMMASq2" side of the RMMA. The large variation in the z component of the $\vec{r}_1$ and $\vec{r}_2$ references points was also indicative of heading uncertainty that could have propagated as the vehicle approached the RMMA. The difference between the non-zero slope of the horizontally fitted linear regression lines (which was between 0.25 and 0.4) fitted to the EOAT detection points and the almost zero slope of the ground truth reference of the $\vec{ap}$ reflectors suggested an external factor (such as non-constant cart leveling with the floor) could have affected the detection angle of the RLS. The standard deviation of the manipulator position after detecting the 3 mm $\vec{ap}$ reflectors was less than 2 mm as measured by the OTS. The distance between the $\vec{ap}$ reflectors as detected by the EOAT and the ground truth reference of the reflectors was between 5 mm to 14 mm, with a larger discrepancy observed on the "RMMASq2" side of the RMMA. Finally, the standard deviation of the cart heading was found to be between 0.75°and 2°and the circular standard deviation cart heading was found to be 0.013 and 0.605 on the "RMMASq2" side of the RMMA and the "RMMASQ3" side of the RMMA, respectively.

The equivalent, calibrated data measured from the robot logs were plotted in Fig. 25. The plot and the accompanied data also included in Sec. 4.3 displayed overall similarity to Fig. 23 and the corresponding OTS data overall. For example, the detected EOAT points in Fig. 25 were visually indistinguishable to those of Fig. 23. The same non-zero regression line slope was observed between the two plots, as was the higher variability in the cart transporter positioning on the "RMMASq3" side of the RMMA when compared to the "RMMASq2" side of the RMMA. As with Fig. 23, the distance between the EOAT reflectors as detected by the EOAT and the ground truth reference of the $\vec{ap}$ reflectors was between 5 mm to 14 mm. The difference in the average cart heading as measured by the OTS and the average cart heading as measured by the cart transporter controller was 0.189°and 0.351°on the "RMMASq2" and "RMMASq3" sides of the RMMA, respectively. Since the difference in the standard deviation as measured by the OTS and by the cart transporter controller was 0.025°and 0.016°and the difference in the circular standard deviation cart heading as measured by the OTS and by the cart transporter controller was 0.001 and zero on the "RMMASQ2" and "RMMASQ3" side of the RMMA, respectively, it was determined that the cart transporter perception of its heading and heading variability matched the corresponding measurements observed from ground truth. Similar to the same data as

determined by the OTS, the standard deviation of the manipulator position after detecting the 3 mm $\vec{ap}$ reflectors was less than 2 mm as measured by the robot controller logs.

Furthermore, the speed and accuracy of two coordinate registration methods were compared using statistical models and inference techniques. The model, which used an unbalanced two-factor factorial design to account for any interaction between the coordinate registration method used and the side of the RMMA measured, was checked against the assumptions that the model errors were from normally, independently distributed populations with equal variance. Although inadequate randomization was a concern due to the limitations of the cart batteries, the Durbin-Watson test was applied and it was found that there was not sufficient evidence to suggest the presence of autocorrelation. There was also not sufficient evidence to suspect serious violations on the normality assumption for both response variables and not sufficient evidence to suggest that the assumption of equal variance was violated on the samples of initial-to-final spiral search distances. However, there was sufficient evidence that suggested the assumption of equal variance may not have held for the samples of coordinate registration time data, which could have influenced the conclusions drawn from the corresponding ANOVA. Along with the presented ANOVA results, plots displaying the sample averages for the registration times (Fig. 27) and sample averages for the initial-to-final search distances (Fig. 28) among each factor combination were examined since there was sufficient evidence to suggest significant interactions were present for both response variables. From the ANOVA, it was concluded that there was not sufficient evidence to suggest that the effect of coordinate registration method on accuracy of the coordinate registration was significant and there was sufficient evidence to suggest that the effect of measured RMMA side on the accuracy of the coordinate registration method was significant. It was also concluded that there was sufficient evidence to suggest that both the registration method used and the side of the RMMA measured were significant effects on the registration time. Additionally, Fig. 27 showed the edge registration method had faster sample average registration times than the bisect method. Again, the related ANOVA conclusions should be interpreted considering the results of the model adequacy checks for the registration times and interactions present.

Finally, the digital level readings at both measured sides of the RMMA were compared to identify if the difference in the cart leveling was significant. Statistical model assumptions were again checked and no sufficient evidence was found to suggest that the normality and equal variance assumptions on the errors for the measurements taken by the front digital level were violated. For the side digital level readings, there was not sufficient evidence to suggest the normality assumption was violated, nor was there sufficient evidence to suggest the presence of autocorrelation. However, there was sufficient evidence to suggest the equal variance assumption may not have been adequately met for the sample of level readings on the "RMMASq2" side of the RMMA taken by the side level. This was accounted for in the comparison by using a Welch's t-test instead of a two-sample t-test. It was found that there was sufficient evidence to suggest a significant difference in the cart leveling for both the front digital level and the side digital level.

Based on the findings of this report, the following potential improvements are noted

for future work. Given that the heading of the cart transporter measured by its controller closely matched the heading measured through the OTS, future experiments may attempt to improve the cart transporter docking process to adjust for any heading error observed between reaching the goal and executing the straight move to approach the RMMA. Although no sufficient evidence was found to suggest the independence assumption had been violated via the Durbin-Watson test, future experiments could improve the procedure by randomly assigning each run to randomly selected treatments (i.e., the side of the RMMA and the registration method used). Improvements to the battery life of the cart can also help to alleviate the limitations of this work in that regard. Additionally, further effort could be made to achieve balance in the experiment design to ensure the robustness of utilized ANOVAs in the event evidence exists to suggest any violations of the assumption of normality and equal variance. Furthermore, the time synchronization could be improved by further minimizing the number of hops and by aggregating the sensors and data capture to use fewer computers, potentially utilizing a wireless access point with support for SNTP, and potentially synchronizing the OTS computer using PTP. Such improvements could allow future experiments to include analysis of dynamic rigid bodies. Given that the cart leveling was deemed significant, the calibration methods, which assumed that no significant leveling difference was present may be further improved to account for this factor. Future development on the coordinate registration methods and implementation may account for the difference in leveling that could impact position uncertainty. For future comparisons in the cart leveling, the Watson-Williams test based in circular statistics may be considered for application over the statistical tests featured in Sec. 4.5.2. Finally, future experiments might also attempt to establish and quantify if any correlation exists between the leveling and the performance of the mobile manipulator-on-a-cart. Such improvements will be incorporated as future work seeks to integrate the OTS itself with the mobile manipulator-on-a-cart. Rather than passively using the OTS to measure performance as in this work, the OTS would instead be used as another coordinate registration method for further comparison.

Acknowledgments

The authors thank the following individuals for their contributions to this project. Dr. Jeremy Marvel, Megan Zimmerman, Shelly Bagchi, Dr. Vinh Nguyen, and Dr. Jennifer Case of the Intelligent Systems Division at NIST, for their technical assistance with CRPI, feedback on the applied statistical methods, sharing of reference materials on quaternion conversions, and general consultation. Dr. Barbara Wainwright, Department of Mathematics and Computer Science at Salisbury University, for her consultation on factorial design experiments and the Durbin-Watson test. Samuel Reed-Weidner, Omron Robotics and Safety Technologies, for his technical consultation on the cart transporter hardware and software, which also included recommendations for configuring the cart transporter to dock with the RMMA. Dr. Soocheol Yoon, Intelligent Systems Division at NIST, for his technical consultation on the cart transporter robot and assistance with the data collection. Elena Messina, Prospicience LLC and Dr. George Dimitoglou, Hood College for their su-

pervision. Dr. Sarala Padi, Information Technology Laboratory at NIST, for her assistance with the data collection.

References

[1] Tavakoli M, Carrier J, Torabi A (2020) Robotics, smart wearable technologies, and autonomous intelligent systems for healthcare during the covid-19 pandemic: An analysis of the state of the art and future vision. *Advanced Intelligent Systems* 2(7). https://doi.org/10.1002/aisy.202000071

[2] Yamaoto T, Terada K, Ochiai A, Saito F, Asahara Y, Murase K (2019) Development of human support robot as the research platform of a domestic mobile manipulator. *ROBOMECH* 6(4). https://doi.org/10.1186/s40648-019-0132-3

[3] Bostelman RV, Hong T, Marvel J (2016) Survey of research for performance measurement of mobile manipulators. *Journal of Research (NIST JRES)* 121:342–366.

[4] Li G, Huang Y, Zhang X, Liu C, Shao W, Jiang L, Meng J (2020) Hybrid maps enhanced localization system for mobile manipulator in harsh manufacturing workshop. *IEEE Access* 8:10782–10795. https://doi.org/10.1109/ACCESS.2020.2965300

[5] Bhatt PM, Malhan RK, Shembekar AV, Yoon YJ, Gupta SK (2020) Expanding capabilities of additive manufacturing through use of robotics technologies: A survey. *Additive Manufacturing* 31:100933. https://doi.org/10.1016/j.addma.2019.100933. Available at http://www.sciencedirect.com/science/article/pii/S2214860419312266

[6] Bostelman RV, Li-Baboud Y, Yoon S, Shah M, Aboul-Enein O (2020) Towards measurement of advanced mobile manipulator performance for assembly applications. https://doi.org/10.6028/NIST.TN.2108.

[7] Khatib O, Yokoi K, Chang K, Holmberg R, Casal A (1996) Coordination and decentralized cooperation of multiple mobile manipulators. *Journal of Robotic Systems* 13(11):755–764. https://doi.org/10.1002/(SICI)1097-4563(199611)13:11⟨755::AID-ROB6⟩3.0.CO;2-U. Available at https://onlinelibrary.wiley.com/doi/abs/10.1002/%28SICI%291097-4563%28199611%2913%3A11%3C755%3A%3AAID-ROB6%3E3.0.CO%3B2-U

[8] Papdopolous E, Rey D (1996) A new measure of tipover stability margin for mobile manipulators. *Proceedings of IEEE International Conference on Robotics and Automation* (IEEE), Vol. 4, pp 3111–3116. https://doi.org/10.1109/ROBOT.1996.509185

[9] Bostelman RV (2018) *Performance measurement of mobile manipulators*. Ph.D. thesis. Université Bourgogne Franche-Comté, 32, Avenue de l'Observatoire 25000 Besancon, France. Available at https://tel.archives-ouvertes.fr/tel-01803721.

[10] Seelinger M, Yoder J, Baumgartner E, Skaar S (2002) High-precision visual control of mobile manipulators. *IEEE Transactions on Robotics and Automation* 18(6):957–965. https://doi.org/10.1109/TRA.2002.805647

[11] Shneier M, Bostelman R (2014) Literature review of mobile robots for manu-

facturing (National Institute of Standards and Technology (NIST)), https://doi.org/10.6028/NIST.IR.8022

[12] (2018) National Institute of Standards and Technology (NIST) robotic systems for smart manufacturing. Available at www.nist.gov/programs-projects/robotic-systems-smart-manufacturing-program.

[13] (2018) National Institute of Standards and Technology (NIST) measurement science for manufacturing robotics. Available at https://www.nist.gov/programs-projects/measurement-science-manufacturing-robotics.

[14] (2018) National Institute of Standards and Technology (NIST) mobility performance of robotic systems. Available at https://www.nist.gov/programs-projects/mobility-performance-robotic-systems.

[15] Bostelman RV, Hong T, Marvel JA (2015) Performance measurement of mobile manipulators. *Multisensor, Multisource Information Fusion: Architectures, Algorithms, and Applications 2015*, ed Braun JJ International Society for Optics and Photonics (SPIE), Vol. 9498, pp 97 – 106. https://doi.org/10.1117/12.2177344. Available at https://tsapps.nist.gov/publication/get_pdf.cfm?pub_id=918268

[16] Bostelman RV, Falco JA, Shah M, Hong TH (2016) *Autonomous Industrial Vehicles: From the Laboratory to the Factory Floor* (ASTM International), Chapter Dynamic Metrology Performance Measurement of a Six Degree-Of-Freedom Tracking System used in Smart Manufacturing, pp 91–105. https://doi.org/10.1520/STP1594-EB

[17] Bostelman RV, Foufou S, Legowik SA, Hong TH (2016) Mobile manipulator performance measurement towards manufacturing assembly tasks. *Proceedings of the 13th IFIP International Conference on Product Lifecycle Management (PLM16)*, eds Harik R, Rivest L, Bernard A, Eynard B, Bouras A (Springer International Publishing), Vol. 492, pp 411–420. https://doi.org/10.1007/978-3-319-54660-5_37. Available at https://tsapps.nist.gov/publication/get_pdf.cfm?pub_id=920470

[18] Bostelman RV, Hong T, Legowik S (2016) Mobile robot and mobile manipulator research towards ASTM standards development. *Multisensor, Multisource Information Fusion: Architectures, Algorithms, and Applications 2016*, ed Braun JJ International Society for Optics and Photonics (SPIE), Vol. 9872, pp 111 – 120. https://doi.org/10.1117/12.2228464

[19] Bostelman RV, Li-Baboud YS, Legowik SA, Foufou S (2017) Mobile manipulator performance measurement data (National Institute of Standards and Technology (NIST)), https://doi.org/10.6028/NIST.TN.1965

[20] Bostelman RV, Eastman R, Hong TH, Aboul-Enein O, Legowik SA, Foufou S (2016) Comparison of registration methods for mobile manipulators. *Advances in Cooperative Robots*, eds Tokhi MO, Virk GS (World Scientific), pp 205–213. https://doi.org/10.1142/9789813149137_0026. Available at https://tsapps.nist.gov/publication/get_pdf.cfm?pub_id=921002

[21] (2020) Ld series mobile robot datasheet. Available at https://assets.omron.com/m/1bf71ca06f961b4b/original/LD-Series-Mobile-Robot-Datasheet.pdf.

[22] (2016) Mobile robot software suite. Available at https://assets.omron.com/m/

0c55a28223f13734/original/Mobile-Robot-Software-Suite-User-s-Guide.pdf.
[23] (2016) Advanced robotics command language reference guide. Available at https://assets.omron.com/m/6f13d7c70932964d/original/Advanced-Robotics-Command-Language-Reference-Guide.pdf.
[24] (2016) Universal robots ur5 technical specifications. Available at https://www.universal-robots.com/media/50588/ur5_en.pdf.
[25] World-beam® qs18llp series datasheet. Available at http://info.bannerengineering.com/cs/groups/public/documents/literature/118900.pdf.
[26] Marvel J, Zimmerman M, Bagchi S, Wyk KV, Kumbla N, Antonishek B, Aboul-Enein O (2019) Collaborative robot programming interface download. Available at https://github.com/usnistgov/CRPI.
[27] (2009) Real-time control system library download. Available at https://www.nist.gov/el/intelligent-systems-division-73500/networked-control-systems-group/real-time-control-systems.
[28] Proctor F (2019) Ulapi download. Available at https://github.com/frederickproctor/ulapi.
[29] Aboul-Enein O, Jing Y, Bostelman R (2020) Formalizing performance evaluation of mobile manipulator robots using ctml. *Proceedings of the ASME 2020 International Mechanical Engineering Congress and Exposition (IMECE 2020)* (ASME), Vol. Volume 2B: Advanced Manufacturing. https://doi.org/10.1115/IMECE2020-23234. V02BT02A004 Available at https://tsapps.nist.gov/publication/get_pdf.cfm?pub_id=928432
[30] (2016) Pro 3600 owner's manual. Available at https://www.leveldevelopments.com/wp/wp-content/uploads/documents/PRO3600_Instructions.pdf.
[31] Tatham S, Lanes A, Harris B, Nevins J (2019) Putty download. Available at https://www.chiark.greenend.org.uk/~sgtatham/putty/.
[32] (2020) How to use remote desktop. Available at https://support.microsoft.com/en-us/help/4028379/windows-10-how-to-use-remote-desktop.
[33] Ml900-24 specification sheet. Available at http://powerbright.com/manuals/specs/ML900_spec_sheet.pdf.
[34] XE and EP batteries range summary. Available at https://www.enersys.com.cn/uploadfiles/main/files/2013/4/20130412104918.pdf.
[35] (2020) Motive download. Available at https://www.optitrack.com/downloads/motive.html.
[36] (2020) Motive documentation calibration. Available at https://v22.wiki.optitrack.com/index.php?title=Calibration.
[37] (2015) Motive documentation rigid body tracking. Available at https://v22.wiki.optitrack.com/index.php?title=Template:Coordinate_System.
[38] (2018) Motive documentation markers. Available at https://v22.wiki.optitrack.com/index.php?title=Markers.
[39] (2020) Motive documentation rigid body tracking. Available at https://v22.wiki.optitrack.com/index.php?title=Rigid_Body_Tracking#Rigid_Body_

Marker_Placement.

[40] Legowik S, Bostelman RV, Hong T (2016) Sensor Calibration and Registration for Mobile Manipulators. *The Fifth International Conference on Advances in Vehicular Systems, Technologies and Applications (VEHICULAR 2016)*, eds Ullmann M, El-Khatib K (IARIA XPS Press), pp 9 – 15. Available at https://tsapps.nist.gov/publication/get_pdf.cfm?pub_id=921474.

[41] Odom W, Knott T (2006) *Networking Basics: CCNA 1 Companion Guide*. Cisco Networking Academy Program series (Cisco Press).

[42] Mainwaring G, Griffiths M Nettime download. Available at https://www.timesynctool.com/.

[43] Anand DM, Sharma D, Li-Baboud Y, Moyne J (2009) Eda performance and clock synchronization over a wireless network: Analysis, experimentation and application to semiconductor manufacturing. *2009 International Symposium on Precision Clock Synchronization for Measurement, Control and Communication* (IEEE), pp 1–6. https://doi.org/10.1109/ISPCS.2009.5340200

[44] Eaton JW (2020) Gnu octave download. Available at https://www.gnu.org/software/octave/download.html.

[45] (2018) Octave statistics package download. Available at https://octave.sourceforge.io/statistics/.

[46] Shah M (2014) Calibration and registration techniques for robotics. Available at http://faculty.cooper.edu/mili/Calibration/index.html.

[47] Arun K, Huang T, Blostein S (1987) Least-squares fitting of two 3-d point sets. *IEEE Transactions on Pattern Analysis and Machine Intelligence* 9(5):698–700. https://doi.org/10.1109/TPAMI.1987.4767965

[48] Shah M (2014) Arun.m source code. Available at http://faculty.cooper.edu/mili/Calibration/RT/arun.m.

[49] Shah M (2013) Solving the robot-world/hand-eye calibration problem using the kronecker product. *Journal of Mechanisms and Robotics* 5(3). https://doi.org/10.1115/1.4024473. Available at https://asmedigitalcollection.asme.org/mechanismsrobotics/article-pdf/5/3/031007/6375575/jmr_005_03_031007.pdf

[50] Shah M, Bostelman R, Legowik S, Hong T (2018) Calibration of mobile manipulators using 2d positional features. *Measurement* 124:322–328. https://doi.org/10.1016/j.measurement.2018.04.024. Available at https://www.sciencedirect.com/science/article/pii/S026322411830294X

[51] Umeyama S (1991) Least-squares estimate of transformation parameters between two point patterns. *IEEE Transactions on Pattern Analysis and Machine Intelligence* 13(4]):376–380. https://doi.org/10.1109/34.88573

[52] Berens P (2009) Circstat: A matlab toolbox for circular statistics. *Journal of Statistical Software, Articles* 31(10):1–21. https://doi.org/10.18637/jss.v031.i10. Available at https://www.jstatsoft.org/v031/i10

[53] Montgomery DC (2013) *Design and Analysis of Experiments* (John Wiley and Sons), Chapter 5, eighth Ed., p 188.

[54] Montgomery DC (2013) *Design and Analysis of Experiments* (John Wiley and Sons), Chapter 15, eighth Ed., pp 652–653.
[55] Montgomery DC (2013) *Design and Analysis of Experiments* (John Wiley and Sons), eighth Ed.
[56] Montgomery DC (2013) *Design and Analysis of Experiments* (John Wiley and Sons), Chapter Appendix, eighth Ed., pp 688–692.
[57] Montgomery DC (2013) *Design and Analysis of Experiments* (John Wiley and Sons), Chapter 3, eighth Ed., pp 80–82.
[58] (2020) Scipy download. Available at https://www.scipy.org/install.html.
[59] (2020) scipy.stats.probplot. Available at https://docs.scipy.org/doc/scipy/reference/generated/scipy.stats.probplot.html.
[60] (2019) Test for autocorrelation by using the durbin-watson statistic. Available at https://support.minitab.com/en-us/minitab/18/help-and-how-to/modeling-statistics/regression/supporting-topics/model-assumptions/test-for-autocorrelation-by-using-the-durbin-watson-statistic/.
[61] (2013) Autocorrelation. Available at https://www.itl.nist.gov/div898/handbook/eda/section3/eda35c.htm.
[62] (2019) Detect autocorrelation in residuals. Available at https://support.minitab.com/en-us/minitab/18/help-and-how-to/modeling-statistics/regression/supporting-topics/residuals-and-residual-plots/detect-autocorrelation-in-residuals/.
[63] Pardoe I, Simon L, Young D (2018) Residuals vs. order plots. Available at https://online.stat.psu.edu/stat462/node/121/.
[64] (2019) Residual plots for fit regression model. Available at https://support.minitab.com/en-us/minitab/18/help-and-how-to/modeling-statistics/regression/how-to/fit-regression-model/interpret-the-results/all-statistics-and-graphs/residual-plots/.
[65] Perktold J, Seabold S, Taylor J (2020) statsmodels.stats.stattools.durbin_watson. Available at https://www.statsmodels.org/stable/generated/statsmodels.stats.stattools.durbin_watson.html.
[66] (2020) scipy.stats.bartlett. Available at https://docs.scipy.org/doc/scipy/reference/generated/scipy.stats.bartlett.html#scipy.stats.bartlett.
[67] McClave J, Sincich T (2017) *Statistics* (Pearson Education), thirteenth Ed.
[68] Montgomery DC (2013) *Design and Analysis of Experiments* (John Wiley and Sons), Chapter 2, eighth Ed., p 33.
[69] (2020) scipy.stats.ttest_ind. Available at https://docs.scipy.org/doc/scipy/reference/generated/scipy.stats.ttest_ind.html.
[70] (2020) scipy.stats.anderson. Available at https://docs.scipy.org/doc/scipy/reference/generated/scipy.stats.anderson.html.
[71] (2011) Sparkfun ftdi basic breakout schematic. Available at https://cdn.sparkfun.com/datasheets/BreakoutBoards/FTDI%20Basic-v22-3.3V.pdf.
[72] Classic rod linear actuators. Available at https://www.firgelliauto.com/products/linear-actuators?_pos=1&_sid=4b1c46503&_ss=r.
[73] Ultra slim pcb relays. Available at https://gfinder.findernet.com/public/attachments/

34/EN/S34EN.pdf.
[74] Relay interface modules. Available at https://gfinder.findernet.com/public/attachments/38/EN/S38EN.pdf.
[75] Corke P (2017) *Robotics, Vision and Control: Fundamental Algorithms in MATLAB* (Springer International Publishing AG), Chapter 2, 2nd Ed., pp 44–46. https://doi.org/10.1007/978-3-319-54413-7
[76] Fu K, Gonzales R, Lee C (1987) *Robotics: Control, Sensing, Vision, and Intelligence* (Tata McGraw Hill Education), Chapter 4, pp 184–186.

Appendix A: Network and Software Diagram

In Fig. 38, a complete network and software diagram is included as a supplementary reference to the information presented in Sec. 2.2.

Appendix B: Connecting the Digital Levels for Data Acquisition

An adapter was used to connect the RS232 serial output of one digital level to the Universal Serial Bus (USB) port of the on-board computer for the manipulator-on-a-cart. The connection to this adapter is shown at the top of Fig. 39. Since a second adapter cable was not available, a breakout board that adapted to Micro-USB was used to connect a second level to the USB port of the on-board computer [71]. The connection to the breakout board is shown at the bottom of Fig. 39. Note that, at the bottom of Fig. 39, the connection to the ground and receive pins on the breakout board had to be swapped to allow for correct data acquisition from the digital level.

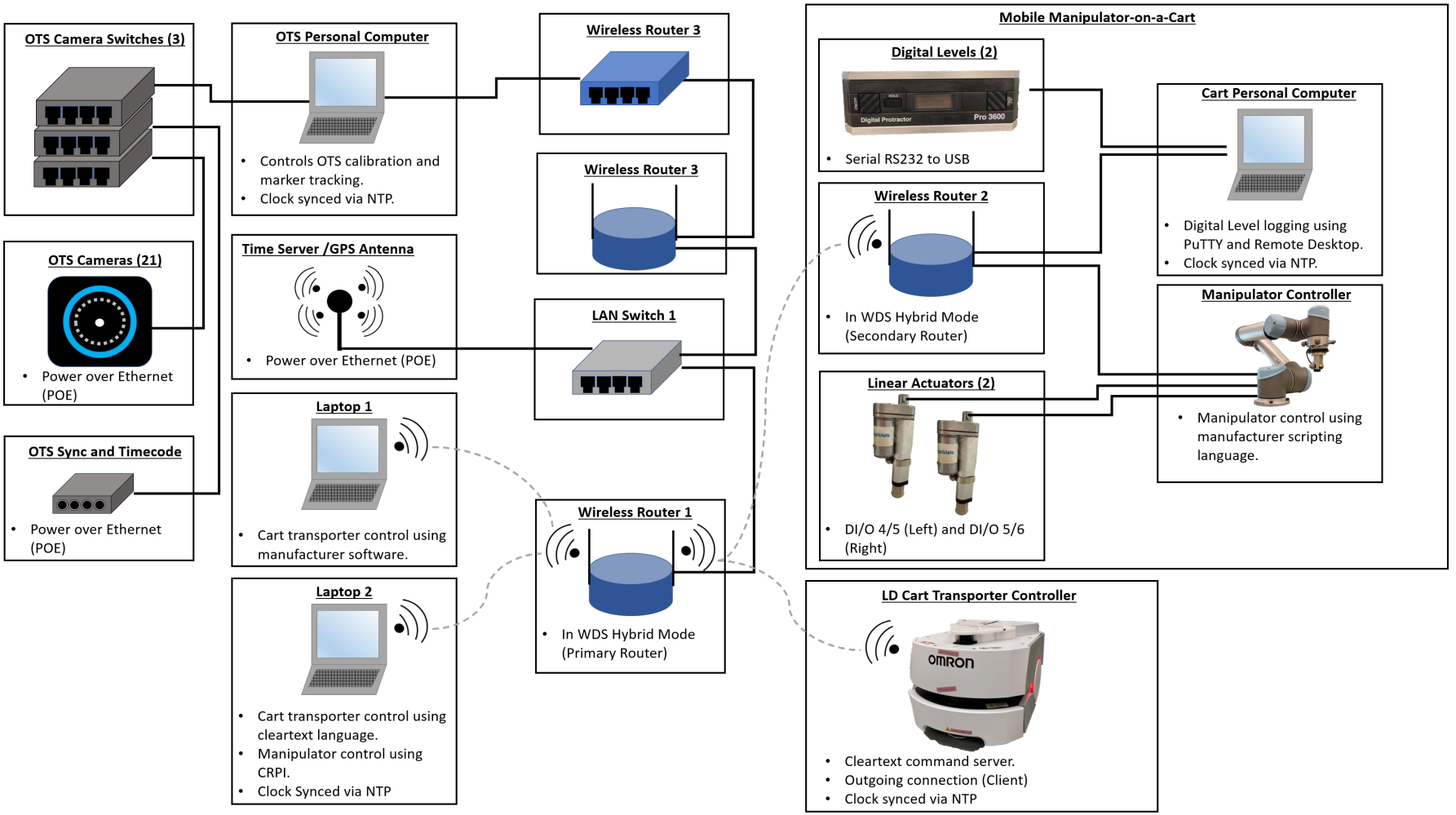

Fig. 38. Network and software diagram for the mobile manipulator-on-a-cart operating environment.

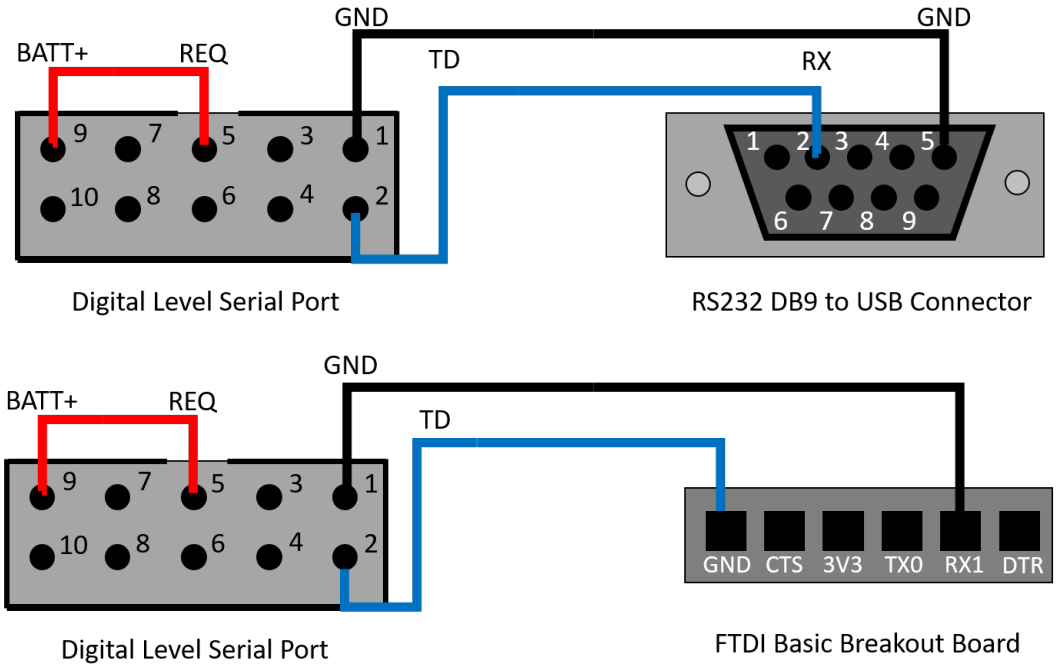

Fig. 39. Connection diagram from digital level to RS232 DB9 connector (top). Connection diagram from digital level to breakout board (bottom).

Appendix C: Hardware Specifications for Linear Actuators

The hardware specifications for the linear actuators of the mobile manipulator-on-a-cart were as follows. One linear actuator had an input voltage of 12 VDC, a maximum load of 1067.57 N, 25% type of duty, and a 7.62 cm stroke [72]. A second linear actuator had an input voltage of 12 VDC, a maximum load of 750 N, a 25% type of duty, and a 7.62 cm stroke. The actuators were connected using relays to digital output ports 4-6 of the manipulator arm as shown in Fig. 38. The circuit diagram for connecting the actuators to the controller is shown in Fig. 40. Four, electromechanical DC relays with 6 A contacts and 24 V coils (relay type 34.51.7.024.0010) were used with a 93.01.0.024 type socket [73, 74]. As stated in Sec. 2.2, this functionality was implemented to prevent the cart from rolling from its docking position while the manipulator was in motion.

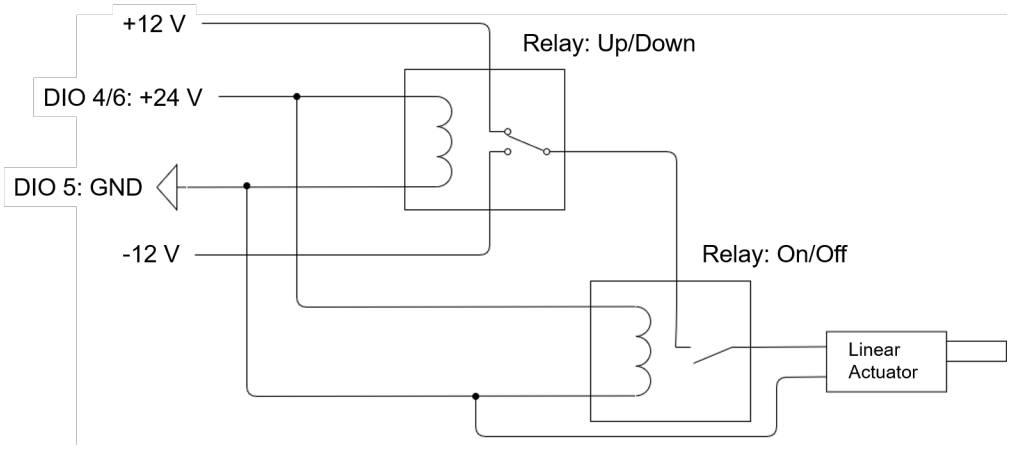

Fig. 40. Circuit diagram for connecting a linear actuator to the manipulator controller I/O.

Appendix D: Conversion from Axis-Angle and XYZ Euler Angles to Quaternion

Let the quaternion representation of a rotation, $\vec{q}$, be a hypercomplex number that follows the definition in Eq. 16 - 18. If angle $\theta_{\vec{n}}$ is a rotation about an axis, $\vec{n}$, then the respective quaternion representation is related through Eq. 19 when $\vec{n}$ is taken to be one of the imaginary axes. Since composition of rotations can be achieved through the non-commutative quaternion product, the XYZ Euler angle representation of a rotation can be converted to the quaternion representation using Eq. 20 [75, 76].

$$\vec{q} = \begin{pmatrix} q_x & q_y & q_z & q_w \end{pmatrix} = q_x\vec{i} + q_y\vec{j} + q_z\vec{k} + q_w \tag{16}$$

$$\vec{i}^2 = \vec{j}^2 = \vec{k}^2 = \vec{i}\vec{j}\vec{k} = -1 \tag{17}$$

$$q_x^2 + q_y^2 + q_z^2 + q_w^2 = 1 \tag{18}$$

$$Rot(\vec{n}, \theta_{\vec{n}}) = cos(\frac{\theta_{\vec{n}}}{2}) + sin(\frac{\theta_{\vec{n}}}{2})\vec{n} \tag{19}$$

$$Rot(\theta_x, \theta_y, \theta_z) = Rot(\vec{i}, \theta_x)Rot(\vec{j}, \theta_y)Rot(\vec{k}, \theta_z) \tag{20}$$

Appendix E: Data Capture Anomalies

During the data capture process, the following data capture anomalies occurred. First, upon completion of the eleventh trial using the bisect registration method[8], which was captured on the "RMMASq2" side of the RMMA, the cart transporter experienced a cart detection

[8]The OTS data capture that started at 03:17:40 PM.

fault. Due to the fault, the cart transporter was unable to re-dock with the cart. The data from this trial was considered to be valid and was not discarded, but the control program had to be reset and the fault manually cleared on the cart transporter by the operator. Following the cart detection fault, an additional, incomplete OTS data capture[9] was discarded since it was deemed an operator error and contained no data of the mobile manipulator-on-a-cart engaged in mock assembly. A twelfth complete trial of data[10] was also captured on the "RMMASq2" side of the RMMA. However, due to the work from home restrictions imposed by the ongoing COVID-19 pandemic, the second part of the trial containing the OTS data for the bisect registration method was not available when data analysis was being conducted. Therefore, this twelfth trial was also omitted. One more additional trial[11] was attempted on the "RMMASq3" side of the RMMA, however, the cart batteries died before the manipulator could complete the bisect coordinate registration, which resulted in incomplete data. Therefore, this last trial was also discarded.

[9]The OTS data capture that started at 03:20:32 PM.
[10]The OTS data captures that started at 03:23:52 PM and 03:26:41 PM.
[11]The OTS data captures that started at 03:30:30 PM and 03:33:21 PM